Jül-4261

Institute of Bio- und Nanosystems
Bioelectronics (IBN-2)

Electrical Characterization of the Cell-Sensor Adhesion with Transistor Transfer Function Measurements

Susanne Schäfer

Mitglied der Helmholtz-Gemeinschaft

JÜLICH
FORSCHUNGSZENTRUM

Electrical Characterization of the Cell-Sensor Adhesion with Transistor Transfer Function Measurements

Susanne Schäfer

Berichte des Forschungszentrums Jülich ; 4261
ISSN 0944-2952
Institute for Bio- and Nanosystems
Bioelectronics (IBN-2) Jül-4261

The complete volume is freely available on the Internet on the Jülicher Open Access Server (JUWEL) at http://www.fz-juelich.de/zb/juwel

Zu beziehen durch: Forschungszentrum Jülich GmbH · Zentralbibliothek, Verlag
D-52425 Jülich · Bundesrepublik Deutschland
☎ 02461 61-5220 · Telefax: 02461 61-6103 · e-mail: zb-publikation@fz-juelich.de

Contents

Chapter 1

Introduction

In the wide field of cell biological research, cell adhesion has been found to form a linkage between various cellular properties like cell growth, cell proliferation and migration. Cell adhesion is understood as the binding of cells to each other or to a substrate. It is determined by multiple intra- and extracellular factors of biochemical or topographical kind. On the one hand, fundamental research adresses the intertwined functions of the cell, which are related to adhesion and migration. On the other hand a variety of bioassays has been developed, which uses cell adhesion as indicator for biochemical effectors like anti-cancer agents. In the context of neuronal networks, cell adhesion is examined to achieve a deeper understanding of network formation and the specialization towards highly complex compounds like the central nervous system or brain tissue. Cell adhesion is observed with various methods, including optical, mechanical and electrical measurements. Certainly the most common approach is optical microscopy. Therefore a variety of highly specialized microscopical methods has been used to analyze the contact area of cells in the vicinity of a substrate. As an example *Transmission Electron Microscopy* (TEM) can be used to image slices of fixated HEK293 cells to determine the cleft-height between cell and substrate (Hoeller [2005], Wrobel et al. [2008]). Unfortunately, this method is restricted to single points of the fixated cell and information on the dynamics of adhesion cannot be obtained. Optical microscopy on the other hand is used to conduct measurements on living cells. The three main approaches are *Total-Internal-Reflection-Fluorescence Microscopy* (TIRF) (Axelrod [1981], Engelhardt [2007]), *Reflection-Interference-Contrast Microscopy* (RICM) (Rädler and Sackmann [1993]), and *Fluorescence-Interference-Contrast Microscopy* (FLIC) (Weis et al. [1996], Iwanaga et al. [2001]). All those methods exhibit a high lateral resolution of typically 200 to 400 nm and are adequate to image lipid bilayers, cell membranes or fluorescent proteins. The height of the

cleft between cell and substrate was determined for various cellular systems and different protein coated substrates (Fromherz et al. [1999], Zeck and Fromherz [2003], Wrobel et al. [2008]). To analyse the adhesive strength of cells on different substrates, a mechanical approach can be combined with RIC microscopy. RICM images are processed to reveal changes of the topography of flexible polymer substrates upon cell adhesion. By calculating the Young modulus and Possion's ratio, the adhesive strength is obtained (Merkel et al. [2007]).

Besides those optical and mechanical techniques, two electrical methods of cell adhesion measurements have evolved: *Electrical cell impedance sensing* (ECIS) on gold electrodes (Giaever and Keese [1984]) and impedance spectroscopy with field-effect transistors (Fromherz et al. [1993], Weis et al. [1996]). With the ECIS system the impedance of cell-covered and cell-free gold electrodes is recorded and the cell impedance is determined by comparison. Changes in the cell impedance are correlated with alterations in cell adhesion. On this basis a variety of bioassays has been developed to investigate cell attachment and cell spreading (Keese and Giaever [1991]) on various protein coatings (Keese and Branner [1993]). Also, cell migration (Wegener et al. [2000], Keese and Branner [1993]) and wound healing (Keese et al. [2004]) can be monitored. These bioassays are adequate to sense the cells' response to biological and chemical compounds, as the cells change their electrical sealing properties upon treatment (Keese and Giaever [1994], Keese et al. [1998]). However, to achieve a deeper understanding of adhesion processes, adhesive strength and the dynamics of cell adhesion must be monitored on a single cell level , which is so far the limitation of the ECIS system. This problem is overvome by impedance measurements with field-effect transistors. These devices are suitable to explore a wide range of biomaterials like cells (Fromherz et al. [1993], Weis et al. [1996]) or protein layers of various compositions (Schasfoort et al. [1989]). Theoretical descriptions of those systems are found for attached cells and biomimetic systems like erythrocyte-ghosts (Kiessling et al. [2000]), membrane vesicles (Fromherz et al. [1999]) or modified membranes (Antonisse et al. [2000], Kharitonov et al. [2001a]). Those theoretical approaches are based on the so called *point-contact model* or the *sheet-conductor model*, assuming the contact area as core-coat capacitor. By the application of Kirchoff's laws, equation systems are found, which are then used to extract adhesion related parameters like the seal resistance. However, these approaches do not illuminate dynamical activity like cell detachment or changes upon chemical treatment.

Both approaches of impedimetric measurements offer great advantages. The respective cellular systems are monitored in real-time with several samples in parallel. Also, the data volumes to be processed are much smaller compared to optical methods. Therefore, automated and non-

invasive setups can be developed, which are independent of expensive and space-consuming lab equipment.

The objective of this thesis is the characterization of single cell adhesion on transistor surfaces with transistor transfer-function measurements. Planar field-effect transistors with 16 recording channels will be presented for adhesion measurements of biomimetic systems like membrane vesicles as well as for cell migration measurements.

The thesis consists of six chapters. Following this introduction, chapter two gives the theoretical background with respect to cellular biology, field-effect devices and impedance spectroscopy. Chapter three covers the device processing, the measurement setup and gives an overview of the various experiments. The experimental results will be presented in chapter four and discussed in chapter five. In the final chapter of this thesis, a conclusion is drawn and improvements as well as possible future experiments are suggested.

Chapter 2

Theoretical Background

2.1 The cell

The cell is the smallest metabolically functional unit of all known living organisms. As structural and functional units cells build tissue and organs. The human body consists of approximately 10^{14} cells with a diameter varying from 10 to 100 μm. The majority of the genetic information is stored inside the nucleus in the chromatin, surrounded by the nuclear membrane. Outside the nucleus, cell organells are embedded in the cytoplasm. The elaborated membrane system, including several organells, metabolizes, produces, stores and redistributes carbonhydrates, proteins (e.g enzymes) or phospholipids (Figure 2.1). Mitochondria function as the energy factory of the cell, providing the most necessary energy carrier ATP. The cytoskeleton, consisting of a filament network, provides mechanical strength and anchorage for the cell organells. It is constantly digested and rebuild. This makes cell proliferation and migration possible. The plasma membrane divides the cell into compartments and encloses the cell body as a whole. It has great influence on structural and signaling funtionality.

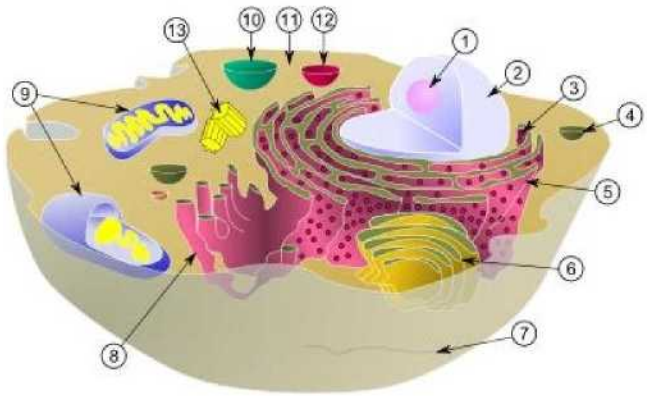

Figure 2.1: The eucaryotic cell with subcellular components (Organelles): (1) nucleolus (2) nucleus (3) ribosome (4) vesicle (5) rough endoplasmic reticulum (ER) (6) Golgi apparatus (7) Cytoskeleton (8) smooth ER (9) mitochondria (10) vacuole (11) cytoplasm (12) lysosome (13) centrioles (Szczepan [2006]).

The membrane

The cell membrane consists of amphiphilic phospholipids. They have a hydrophilic (polar) head group and a hydrophobic fatty acid tail (nonpolar). In aqueous environment the phospholipids assemble to a 5-10 nm thick bilayer. Proteins are embedded in the bilayer (integral proteins) or attached to it (peripheral proteins). They determine the membrane properties (Figure 2.2) and are e.g. responsible for active transport, signal transduction, enzyme activity, and cell adhesion. This compound is understood as a two-dimensional, non-static fluid that allows lateral diffusion

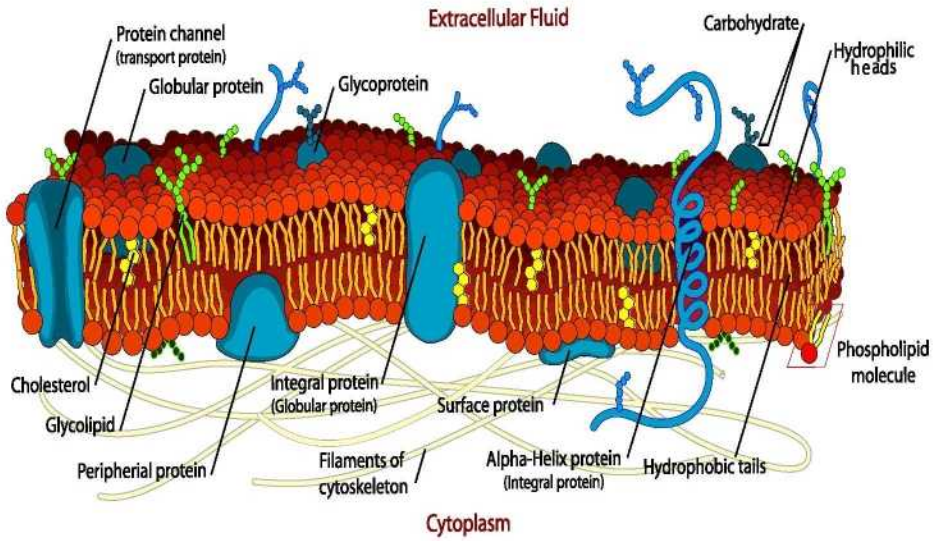

Figure 2.2: Composition of the cell membrane.Ruiz [2007]

and the rare flipflop movements. It is often compared to a fluid mosaic (Singer and Nicolson [1972]). In an equivalent circuit the electrical properties of the lipid bilayer are given by an ohmic resistor and a capacitor in parallel as shown in Figure 2.3. A typical value for the specific membrane capacitance is $C_{mem,spec} = 1\mu F cm^{-2}$ (Adam et al. [1988]). The cell membrane separates cell or subcellular organelles from their surrounding. As a semipermeable barrier it ensures a high degree of specific cellular metabolism. While lipophilic and gas molecules (O_2, CO_2) can diffuse freely through the membrane along a concentration gradient, the membrane is impassable for polar or big molecules. However, those molecules can either pass the membrane through ion channels (passive transport) or by binding to specific transport proteins (active transport). The latter is an energy consuming process as the molecules are transported against their concentration gradient.

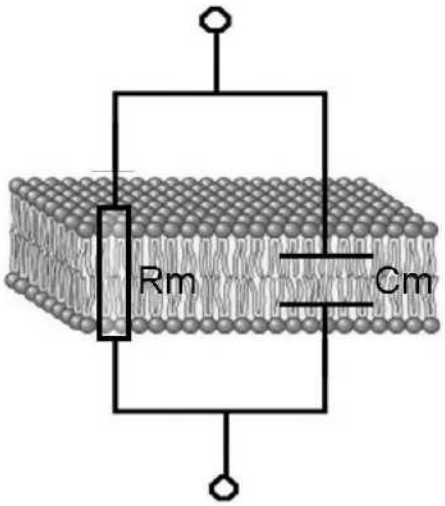

$$C_m = C_{m,spez} \cdot A_m = \left(\frac{\epsilon_0 \cdot \epsilon}{d_m}\right) \cdot A_m \tag{2.1}$$

$$R_m = \frac{R_{m,spez}}{A_m} \tag{2.2}$$

Figure 2.3: Equivalent circuit of a lipid bilayer.

C_m: Membrane capacitance [F]
A_m: Membrane area $[m^2]$
R_m: Membrane resistance $[\Omega]$
ϵ_0: Dielectric constant $(8.854 \cdot 10^{-12} F m^{-1})$
$C_{m,spez}$: Specific membrane capacitance $[F \cdot m^{-2}]$
R_m: Specific membrane resistance $[\Omega \cdot m^2]$
d_m: Membrane thickness $[m]$
ϵ: Dielectric constant of membrane

Ion channels and membrane potential

Ion channels are highly selective passages through the lipid bilayer. They consist of one or more integral membrane protein domains around a waterfilled pore. The archetypical channel is just one or two atoms wide at its narrowest point and specific to a certain species of ions. In some ion channels, the passage through the pore is governed by a gate, which may be influenced and switched by chemical or electrical signals, temperature or mechanical force.

Selective permeability for the different species of ions through the membrane allows the cell to establish an inhomogenous distribution of ions between the cell interior and the surrounding environment. Electrogenic pumps stabilize this concentration gradient in an energy (ATP) consuming pumping process. In case of the sodium-potassium pumps, two potassium ions are pumped into the cell for every three sodium ions pumped out (Figure 2.4). The interplay of diffusion forces, electrostatic interactions and a certain leakage results in an equilibrium state called the equilibrium potential or resting potential of the cell. For one ion species X the equilibrium potential E_X can be calculated with the Nernst-equation (Equation 2.3):

The membrane potential in real cells is predominantly caused by different intra- and extracellular concentrations of sodium, potassium and chloride ions. With given permeabilities P^X for each

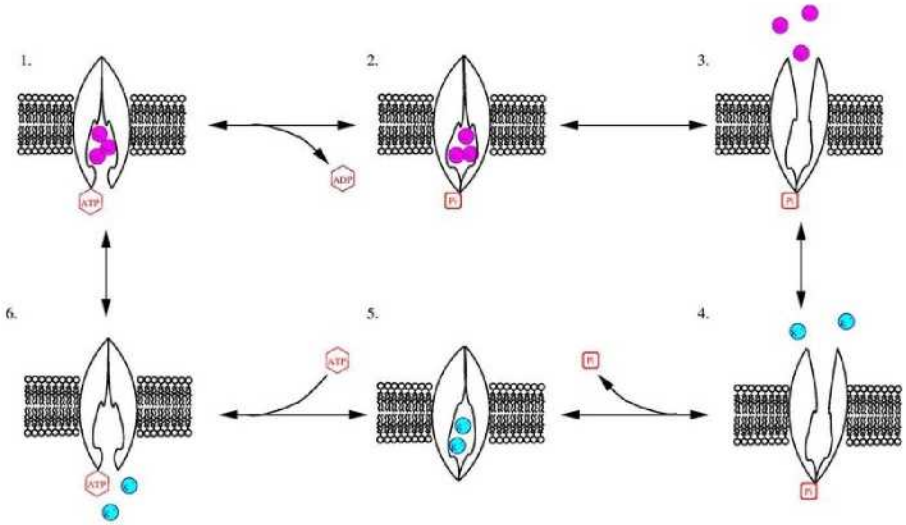

Figure 2.4: The sodium-potassium pump maintains the concentration gradient across the cell membrane. For every three sodium ions pumped out, two potassium ions are pumped into the cell. (Gastrein [2005])

$$E_X = \frac{RT}{zF} \cdot ln\left(\frac{[X]_{out}}{[X]_{in}}\right) \tag{2.3}$$

R: Gas constant ($8.31 J/molK$)
T: Temperature [K]
F: Faraday constant ($96.5 \cdot 10^3 C/mol$)
z: Valence of the ion
$[X]_{out}$: Extracellular concentration of ion species X
$[X]_{in}$: Intracellular concentration of ion species X

ion species the membrane potential can be calculated by the Goldman-Hodgkin-Katz equation (equation 2.4). For electrogenic cells, this membrane potential normally is in the range of -60mV to -90mV.

$$E_m = \frac{RT}{Fz} \cdot ln\left(\frac{P^K[K^+]_{out} + P^{Na}[Na^+]_{out} + P^{Cl}[Cl^-]_{in}}{P^K[K^+]_{in} + P^{Na}[Na^+]_{in} + P^{Cl}[Cl^-]_{out}}\right) \tag{2.4}$$

Electrically active cells

Some cell types like neurons or cardiac myocytes are electrically active. As such, they can rapidly change their membrane potential, causing a so called action potential. Travelling waves of this potential changes are the fundamental mechanism of electrical signal propagation in cellular networks. This was first observed by Cole [1949]. It can be measured with the invasive Patch-Clamp Technique (Neher and Sakmann [1976]) or non-invasively, e.g. with field-effect devices (see section 2.2). For a deeper understanding of the electronic cell-device coupling it is necessary to gain information about the adherence properties of the cell to its substrate.

2.1.1 Cell adhesion

Cell adhesion is an intrinsic characteristic of cells. There are two adhesion types: Cells either adhere to each other (with tight junctions, gap junctions, desmosomes, or adherens junctions) or to a substrate (focal adhesions, integrins, hemidesmosomes). Cell-cell adhesion is mainly mediated by a protein family called cadherins, whereas transmembrane proteins, called integrins, bind the cell to a substrate, often building complexes called focal adhesions. Integrins are heterodimeric proteins, consisting of two domains. Many α- and β-domains are known, appearing in varied compositions and fulfill multiple structural and signaling functions. Integrins form a structural link between the intracellular cytoskeleton and the *extracellular matrix* (ECM). On the intracellular side, they bind to structural proteins (talin, α-actinin) associated with the actinfibres of the cytoskeleton forming an adhesion complex. On the extracellular side they act as receptors with a selective affinity for certain ECM-components. The cognized sequences often consist of the three amino acids arginine, glycine and aspatate (RGD-sequence). Integrins bind to the ECM in high number, but with low affinity, creating a so called "velcro"-effect. Therefore cells can attach without loosing their mobility, retaining the ability to explore their environment.

Integrins possess intra- and extracellular receptor sites. Upon ligand binding they can trigger

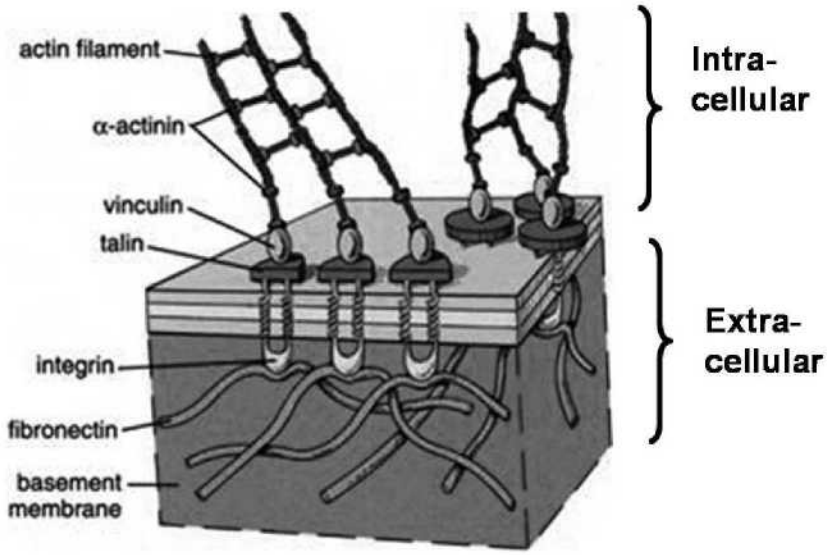

Figure 2.5: Integrins are the mechanical link between extracellular matrix and cytoskeleton and are involved in signaling pathways. The picture was adapted from Swartz [2007].

signal cascades or interact with other signal receptors. Hence integrins contribute to the signal exchange between ECM and cell interior (Alberts et al. [2004]). Furthermore, most cells cannot

survive without integrin activity. Loss of contact then induces apoptosis. For those reasons cell adhesion is explored and used to gain information on cell growth, movement and proliferation (Jung et al. [2001]). Cell-substrate adhesion can be governed topographically (Curtis and Wilkinson [1997], Berry et al. [2004]), biochemically (Arnold et al. [2004]) or a with a combination of both (Chen et al. [1997]).

2.1.2 Cell migration

Cell migration holds a central role in processes like wound healing or the immune response. During tissue development many different cell types travel over long distances through changing environments until they reach their final destination.

The migrating movement of cells is a cycle of three different phases. It is initiated by the directional protrusion of the leading edge by actin polymerization. Lamellipodia are formed and stabilized by new adhesion complexes. During migration the cell front is bound to the substrate more tightly than the cell rear, thus generating the traction and force needed for a net forward movement. In a third step the cell removes the rear by detachment and subsequent retraction, either by a regulated release of focal adhesions or by ripping them off (schematically shown in Figure 2.6). Naturally, parameters influencing cell adhesion also have an impact on cell migration, causing a strong link between adhesion and migration research (Huttenlocher et al. [1995]).

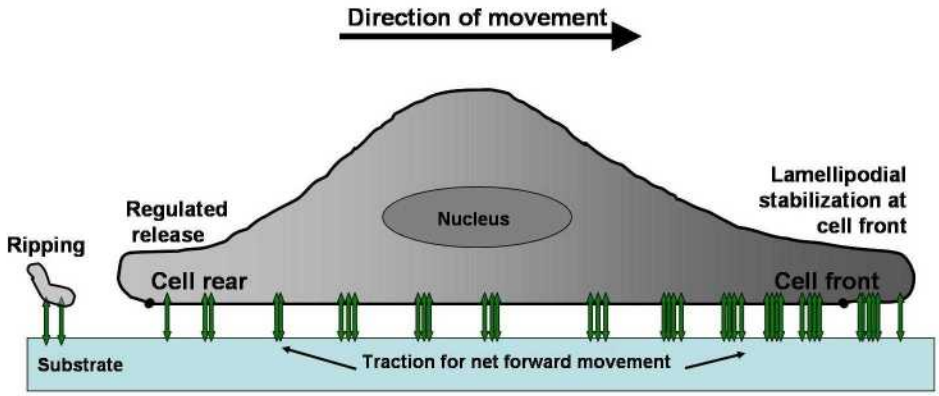

Figure 2.6: Schematic of migrating cell. The figure was adapted from Huttenlocher et al. [1995].

2.1.3 Apoptosis

Apoptosis is a common kind of programmed cell death. Initiated by internal or external cues, the cell starts a precise cycle of decomposition of all cell components. This leads to morphological changes, the loss of the membrane asymmetry, shrinkage and finally nuclear defragmentation. This controlled process is needed in every organism to ensure homeostasis, which is the equilibrium of cell proliferation and cell death. An imbalance of cell proliferation and apoptosis leads to misdevelopment or severe diseases (Thompson [1995]). Excessive apoptosis e.g. causes hypotrophy, whereas insufficient apoptosis results in uncontrolled cell proliferation like tumor growth. For these reasons, apoptosis is an increasing research topic since the early 1990s. Several involved signalling pathways have been identified, most of them acting via the tumor-suppressing gene p53. Also, mitochondria have a great influence on apoptosis regulation (Green and Reed [1998]). They can release effectors that activate so called caspases, which carry out the degradation of the cell (Fesik and Shi [2001]). Although the pathways are complex and not fully revealed, some reagents like NO were found to interfere in the pathways and therefore stimulate or suppress apoptosis (Brüne [2003]). Furthermore, an acidification of up to 1 pH is observed for apoptotic cells (Barry et al. [1993]) and precedes DNA defragmentation (Gottlieb et al. [1996]). The cytosolic acidification increases the caspase activity dramatically (Matsuyama et al. [2000]), implying the pH homeostasis as regulator for early apoptosis in the mitochondrial pathway. The most common method to visualize apoptosis is fluorescence staining. Peptides like annexin-V, which are labeled with dies like FITC, bind to negatively charged phospholipids (phosphatidylserine) on the membrane (Aubry et al. [1999]). Usually, those phospholipids are only expressed on the inner side of the membrane, but are transported to the outer membrane surface in an early apoptotic state of the cell (Kenis et al. [2004]). On the other hand, late apoptosis can be seen with dies like propidium iodide, which diffuses through the apoptotic membrane and intercalates with the DNA in the nucleus in a concentration of one dye per 4-5 base pairs. Neither annexin-V nor propidium iodide can bind to viable cells.

2.2 The field-effect transistor

The *field-effect transistor* (FET) is a semiconductor device, which basically consists of two pn-junctions and which uses an electrical field to control the conductivity of a channel region. Even small changes in the potential applied to the device can be detected and subsequently be amplified. This ability to detect small potential changes can be used to perform non-invasive cell measurements.

Most FETs are addressed by four terminals. Two of them, called *source* S and *drain* D, consist of highly n- or p-doped semiconducting material (n-FET or p-FET). The controlling contact (*gate* G) is separated from the channel by a highly resistive barrier (insulated-gate FET (IGFET)). This layer usually consists of silicon-dioxide (SiO_2) and its thickness determines the gate capacitance. Typically metal is used as gate material, giving the device the name *metal-oxide-semiconductor FET* (MOSFET) (schematically shown in Figure 2.7). The MOSFET was first introduced by Kahng and Atalla [1960]. The fourth contact (*body or bulk* B) simply refers to the substrate body, in which drain and source are embedded. Usually the bulk terminal is connected to the highest (p-FET) or lowest (n-FET) voltage within the circuit, therefore being set to the source potential. It can also be operated as a second gate and is then referred to as the *back gate*. In this case, the bulk can be used to set the threshold voltage of the device. To adjust the channel resistivity, a gate voltage V_{GS} is applied, modifying the mobility and concentration of charge carriers in the channel.

In order to measure electrical cell signals in an aqueous environment, the gate area can be left without a final metalization (*open-gate FET*). Instead, an electrolyte solution, which is contacted by a bath electrode, is used (Bergveld et al. [1976]). This transistor type is also called ISFET (*ion-sensitive FET*) or EOSFET (*electrolyte-oxide semiconductor FET*). When a gate-source voltage higher than the intrinsic threshold voltage V_{th} is applied to the insulating SiO_2-layer, a channel area with strong inversion of charge carriers is created. Once a drain-source voltage V_{DS} is applied, this inversion layer provides a conductive path through which the drain-source current I_{DS} can pass.

The operation modes of p-channel FETs and n-channel FETs are similar, with holes being the electrical majority carriers for p-FETs and electrons being the majority carriers for n-FETs. In both cases only one type of carriers contributes to the current, contrary to bipolar transistors.

Two types of FETs are distinguished: For enhancement type FETs the current flow I_{DS} increases with increasing V_{GS}. For the depletion type FET, I_{DS} decreases for increasing V_{GS}. Enhancement

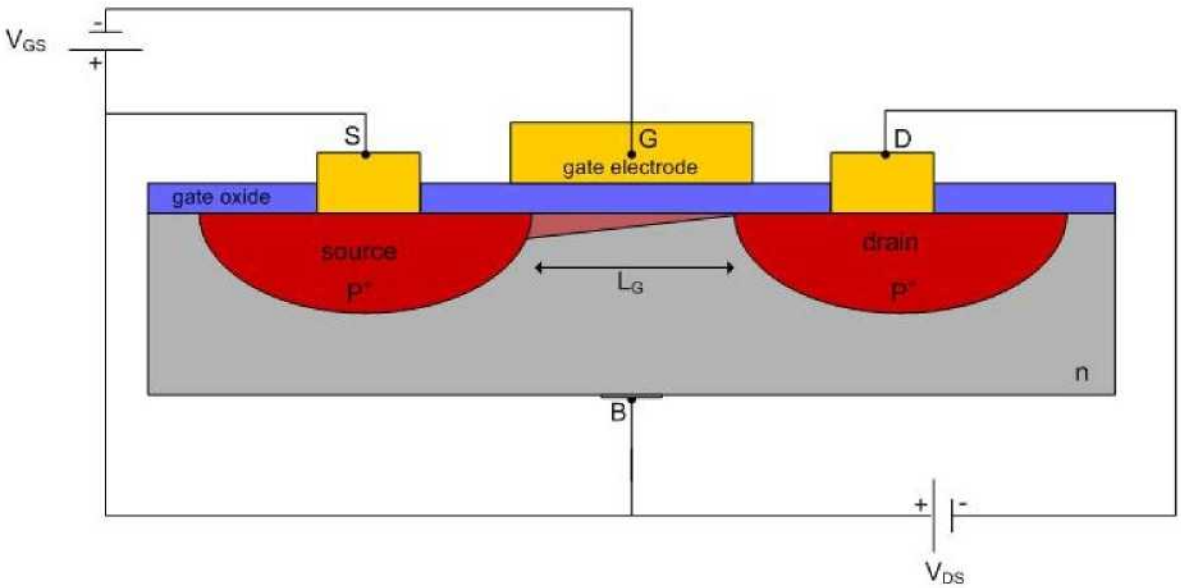

Figure 2.7: Schematic of a p-channel MOSFET. Gate-, source-, drain- and bulkelectrodes are labeled with G,S,D and B, respectively. V_{GS} refers to the gate-source voltage, V_{DS} to the drain-source voltage. Between the p-doped conducting lines, the channel with length L_G can be seen.

FETs are therefore *normally off*, whereas depletion FETs are *normally on*.

2.2.1 Characteristics

A FET is characterized by the following parameters:

- Output characteristics: $I_{DS}(V_{DS})$ with constant V_{GS}
- Transfer characteristics: $I_{DS}(V_{GS})$ with constant V_{DS}
- Transcondustance $g_m(V_{GS})$ with constant V_{DS}
- Gate capacitance C_G

The transconductance g_m is defined as the change of the drain current I_{DS} with the applied gate voltage V_{GS} while keeping the drain-source voltage V_{DS} constant (equation 2.6). Typical output, transfer characteristics and transconductance of a planar enhancement-type p-FET are shown in Figure 2.8.

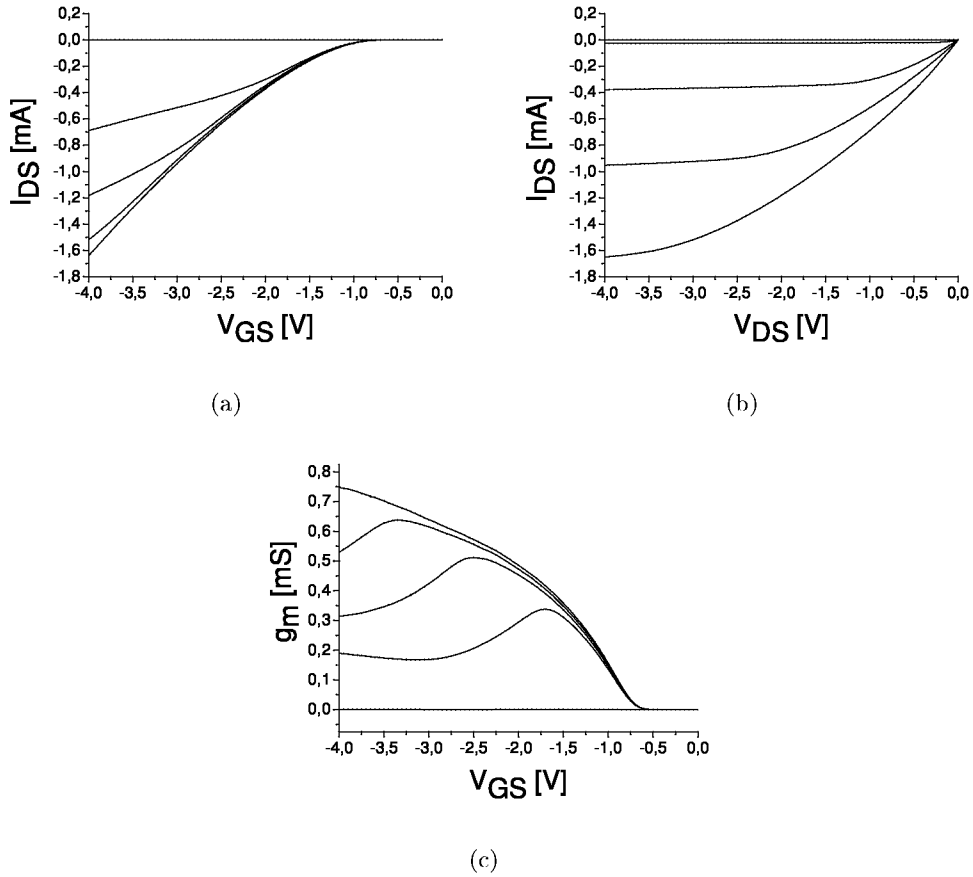

Figure 2.8: Transfer (a), output characteristics (b), and transconductance (c) of a planar p-FET with gatewidth $25\mu m$ and gatelength $4\mu m$. Gate-source voltage was swept from 0 to −4V, drain-source voltage decreased in steps of −1V from $0V$ to $-4V$.

Depending on the applied voltages, three different states of operation of the transistor occur:

- Sub-threshold

  While the gate-source voltage V_{GS} is smaller than the intrinsic threshold-voltage V_{th}, there should be no gate-source current. Nevertheless leakage currents can occur in real FETs, caused by defects in the gate oxide.

- Linear Region

  For small voltages $V_{GS} > V_{th}$ and $V_{DS} < (V_{GS} - V_{th})$, the inversion layer thickness is independent of V_{DS} and I_{DS} is nearly proportional to the drain-source voltage. The transistor operates like a variable resistor:

$$I_{DS} = \mu_n \cdot c_{ox} \cdot \frac{W_G}{L_G} \cdot \left((V_{GS} - V_{th}) V_{DS} - \frac{V_{DS}^2}{2} \right) \tag{2.5}$$

μ_n: Carrier mobility
$c_{ox} = \frac{\epsilon_{ox}}{d_{ox}}$: Specific oxide capacitance
ϵ_{ox}: Dielectric constant of the oxide
d_{ox}: Oxide thickness
W_G: Gate width
L_G: Gate length

The transconductance is then given by a partial derivation:

$$g_m = \frac{\delta I_{DS}}{\delta V_{GS}}|_{V_{DS}} = \mu_n \cdot c_{ox} \cdot \frac{W_G}{L_G} \cdot V_{DS} \tag{2.6}$$

- Saturation

  If the drain-source voltage is increased, the potential gradient from source to drain gives the channel an asymmetrical form. The inversion region becomes "pinched-off" near the drain end of the channel. If the drain-source voltage is increased further, the pinch-off point of the channel moves away from the drain towards the source. Even though the conductive channel no longer connects source to drain, carriers are not blocked completely from flowing. The charge carriers are free to move out of the channel through the depletion region if attracted to the drain by the drain-source voltage. The depletion region acts as a resistor with a resistance similar to silicon. Increase of the drain-source voltage will increase the distance from drain to the pinch-off point, increasing the resistance due to the depletion region proportionally to the applied drain-source voltage. Therefore the drain-source current will remain relatively fixed, independent of changes to the drain-source voltage. The FET behaves as a constant-current source rather than as a resistor and can be used as a voltage amplifier. Here, the gate-source voltage controls the level of constant current through the channel. This operation mode is called saturation mode.

  The dependency of the saturation-current from the gate-potential V_G varies for different gate-lengths L_G. In very short channels, the source-drain field is quite high and moving carriers reach a saturation velocity v_s quickly. Therefore the current I_{DS} increases proportional with the influenced charge proportional to the gate potential V_G.

  For longer channels the carrier velocity is also proportional to their mobility and therefore to V_{DS}. The dependency of the source-drain current from the gate-voltage is no longer linear but squared. For the saturation region ($V_{GS} > V_{th}$, $V_{DS} > (V_{GS} - V_{th})$) the following approximation can be made:

$$I_{DS} = \mu_n \cdot c_{ox} \cdot \frac{W_G}{2 \cdot L_G} \cdot (V_{GS} - V_{th})^2 \tag{2.7}$$

The transconductance g_m is then given by:

$$g_m = \frac{\delta I_{DS}}{\delta V_{GS}}|_{V_{DS}} = \mu_n \cdot c_{ox} \cdot \frac{W_G}{L_G} \cdot (V_{GS} - V_{th}) \tag{2.8}$$

2.2.2 Noise

If very small cellular signals are to be detected, the noise in the signal pathway becomes important, as it might conceal the signal to be measured. Geometry of the gate area and process parameters can be adjusted to build FETs with a low noise level (Völker [2005]), e.g. by burying the channel further into the substrate (see subsection 2.2.3). The devices built within this work were not optimized regarding noise. Nevertheless, a full device characterization includes noise measurements. Hence, noise shall be discussed briefly below.
Noise is the fluctuation of a variable (e.g. the measured cellular signal) caused by nonpredictable and random processes, which cannot be reproduced. There are many sources of noise along the signal path, from noise at the electrolyte-SiO_2 interface to noise produced in the amplification stage. Attention will be set to the transistor noise as an intrinsic characterisic.
Let $\overline{A}$ be the time average of the total signal A(t), corresponding to the direct current (DC) component of A(t) with:

$$\overline{A} = \lim_{T \to \infty} \frac{1}{2\pi} \int_{-T}^{+T} A(t)dt \tag{2.9}$$

Then the noise a(t) is the deviation of $\overline{A}$ from A(t): $a(t) = A(t) - \overline{A}$. The time average of the noise is zero by definition: $\overline{a(t)} = 0$. With this the power of the signal fluctuations can be defined:

$$\overline{a(t)^2} = \sigma^2 = \lim_{T \to \infty} \frac{1}{2T} \int_{-T}^{+T} [a(t)]^2 dt \tag{2.10}$$

Often the effective value is used for calculations, also called the root-mean square value:

$$\sqrt{\overline{a}^2} = \sigma = a_{rms} \tag{2.11}$$

For transistors two kinds of noise dominate: thermal noise and generation-recombination noise. Thermal noise arises from resistors like feed lines, drain and source contacts or the channel itself. It is evenly distributed causing a so-called *white noise*. This type of noise was firstly observed by John B. Johnson (Johnson [1928]) and described by Harry Nyquist (Nyquist [1928]), also giving

it the name *Nyquist-* or *Johnson-noise*. The thermal noise voltage is proportional to temperature and resistance: $dV^2 \propto R \cdot kT$ (k : Boltzmann constant). As the temperature is kept around 37°C for cell experiments, the resistance must be reduced in order to decrease the white noise. This can be done by using highly doped or metalized feed lines. While thermal noise is not frequency dependent, generation-recombination noise is highly dependent on frequency. It results from capture- and emission-processes at the defects of the semiconductor-oxide interface. Majority charge carriers tunnel into traps of the SiO_2 and back, modulating the channel conductance and therefore the current I_{DS} (Jordan and Jordan [1965]). This random change between two distinct states is also called *random telegraph signal* (RTS). The resting times τ_0, τ_1 in those states depend on the tunneling distance. Therefore the propability of tunneling processes can be significantly reduced by burying the channel further into the silicon substrate leading to a noise reduction.

Although noise is a random process, for known $a(t_0)$ it is possible to estimate the noise at $t_1 = t_0 + \tau$. The necessary quantity is the autocorrelation function $\rho(\tau)$. It determines the strength of correlation at $t_0 = 0$ and at a time $t_1 > t_0$.

$$\rho(\tau) := \lim_{t\to\infty} \frac{1}{2T} \int_{-T}^{+T} a(t)a(t+\tau)dt \tag{2.12}$$

The correlation becomes maximal for $\tau = 0$ with $\rho(0) = \sigma^2$. The Fourier transform of the autocorrelation function is the spectral noise density S(f).

$$S(f) := 2 \int_{-\infty}^{\infty} \rho(\tau) exp^{(-2\pi i f \tau)} d\tau \tag{2.13}$$

The factor 2 is added due to the fact that $\rho(\tau)$ is a symmetrical function ($\rho(\tau) = \rho(-\tau)$).

For white noise the spectral noise density is constant and the respective autocorrelation function a δ-distribution.

To calculate the spectral noise density from a measured signal, it is more useful to give S(f) in the form:

$$S_a(f) := \lim_{t\to\infty} \frac{1}{2T} \int_{-T}^{+T} a(t) exp^{(i2\pi f t)} dt \tag{2.14}$$

When noise is plotted as frequency spectrum (see Figure 2.9) generation-recombination noise dominates for frequencies 0.1 Hz to 10 kHz, whereas white noise governs the medium range fre-

quencies. As it can be seen in Figure 2.9, two more characteristic regions can be defined. The δ-peak equals the DC-value of the signal at $f = 0$ and does not contribute to the spectral noise density. The noise drop at the end of the spectrum originates in the total noise power being a finite value. The spectral noise density must drop for higher frequencies (Müller [1990]).

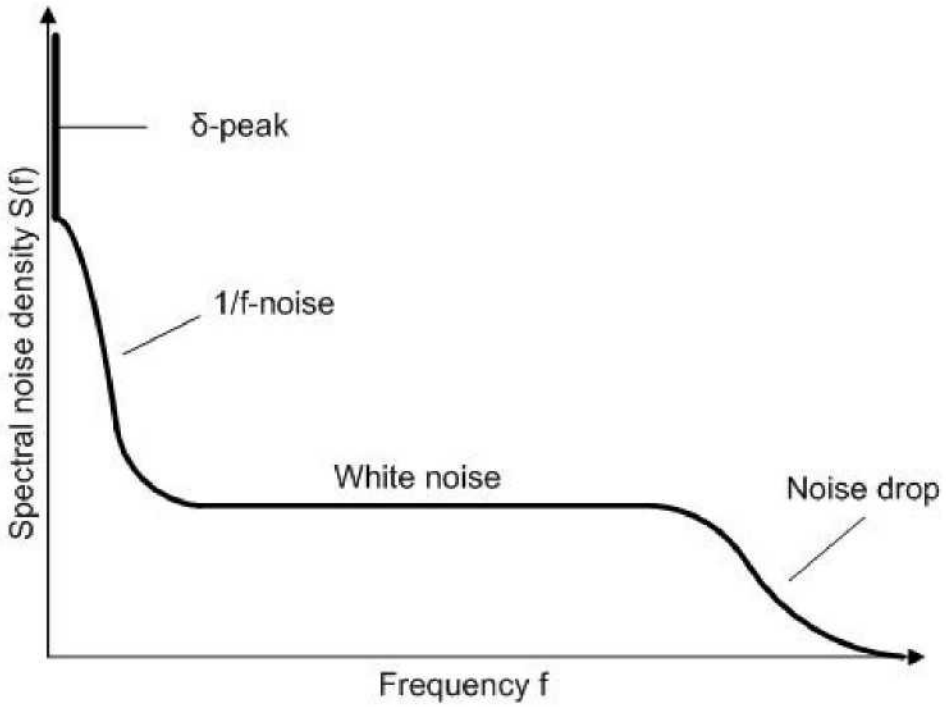

Figure 2.9: Frequency schematic of the spectral noise density. The figure was adapted from Müller [1990].

2.2.3 Buried-channel FETs

To minimize transistor noise the conducting channel can be buried in the substrate. This increases the tunneling distance and hence decreases the tunneling propability. By this, generation-recombination noise is lowered. The channel is buried with an appropriate implantation energy, shifting the typical Gaussian ion distribution into the substrate, away from the silicon-oxide interface. If boron ions are implanted into the gate area, the characteristics of the transistor change significantly. Without an applied voltage the transistor is conducting. This leads to the name *normally-on transistor* or *depletion-mode FET*.

2.2.4 Cellular signals measured with field-effect devices

The electrical coupling between cell and field-effect transistor strongly depends on the cell adherence to the transistor gate. The coupling of an electrically active cell to a transistor was first described by Regehr et al. [1989] in an idealised equivalent circuit (Figure 2.10). The cell encloses the gate forming a cleft filled with electrolyte. This cleft acts as a resistor with the resistance R_J (conductance G_J) depending on factors like the cleft height and geometry, as well as the electrolyte composition. The cleft height strongly varies with cell type and surface modification. So far, various values have been determined: 10 nm for erythrocytes on poly(L)lysine (Kiessling et al. [2000]), 28 to 39 nm for HEK293 on poly(L)lysine (Wrobel et al. [2005]), 50 nm to 75 nm for HEK293 on fibronectin (Braun and Fromherz [2004], Gleixner and Fromherz [2006]), 60 nm for neurons on fibronectin and 110 nm for neurons on laminin (Braun and Fromherz [1998]). The ion current leaving the cleft causes a voltage drop across the resistance R_J. In the *Point-Contact Model* the electric coupling takes place in a single point, represented by the junction voltage V_J. A patch pipette with capacitance C_{fast} and resistance R_S is used to control the intracellular voltage. The pipette parameters are usually extracted from the patch-clamp experiment. Free and attached (junction-) membrane are distinguished, each with a certain membrane capacitance (C_{FM} and C_{JM}). Ion channels and leakage through the membrane are represented as Hodgkin-Huxley Elements, consisting of resistor and a capacitor elements in series. With this model it was possible to explain extracellular recordings quite accurately (Ingebrandt et al. [2005]). Nevertheless the system is based on invasive patch-clamp measurements. In the next section impedance measurements will be introduced, offering a non-invasive technique to gain information about cellular properties.

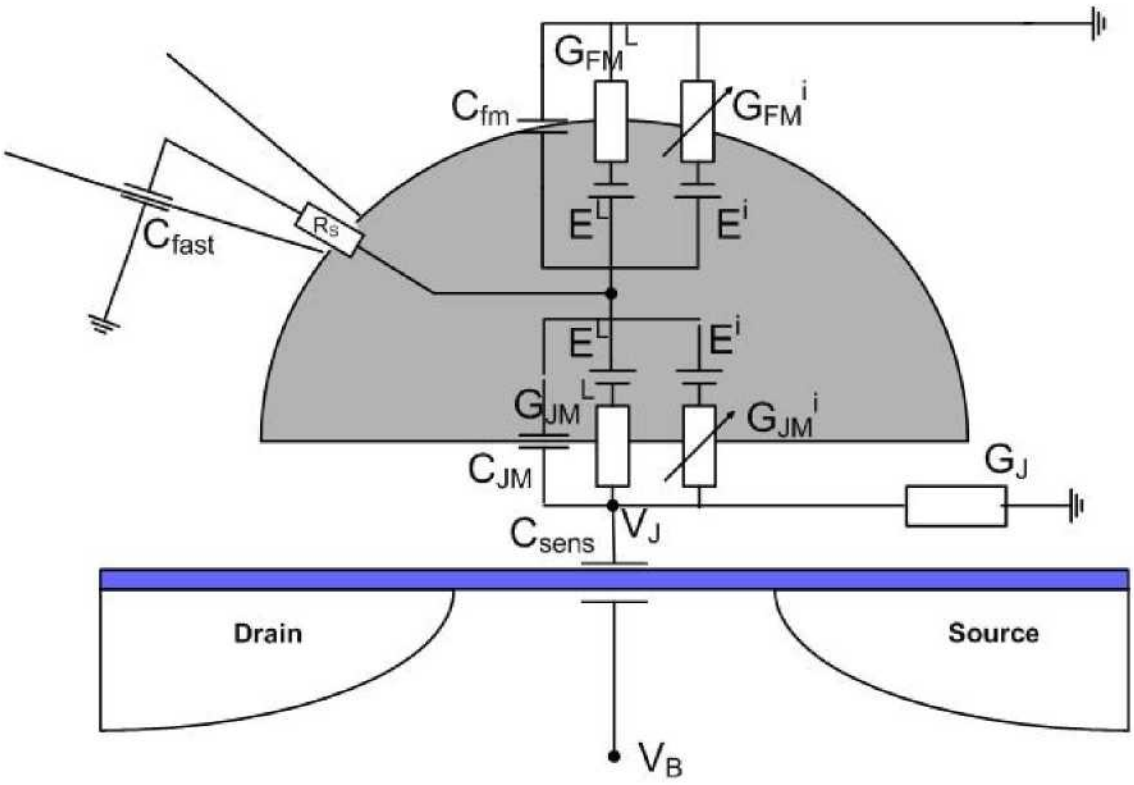

Figure 2.10: Point-contact model of a cell and an open-gate FET. The picture was adapted from Meyburg [2005].

2.3 Impedance measurements

The most common approach to examine biological processes like cell adhesion or motility phenomena is optical microscopy. Although the lateral resolution is high and staining methods have become very elaborate, there are several disadvantages to this approach. Firstly, only one sample can be observed at a time and secondly, expensive as well as space-consuming equipment is needed. Furthermore staining is an invasive method of monitoring as it affects the observed cells permanently. For these reasons, electrical monitoring using impedance spectroscopy has been developed since the early 1990s. The spectroscopy methods are usually accomplished with electrodes (*electrical cell impedance sensing*: ECIS) or with field-effect devices (*ion-sensitive FET*: ISFET, *enzyme-sensing FET*: ENFET). These systems offer the monitoring of cellular systems in real-time with several samples in parallel. Also, the data volumes to be processed are much smaller. Therefore, automated and non-invasive setups can be developed, which are independent of space-consuming lab equipment.

2.3.1 Impedance measurements with electrodes

An established method to examine cellular phenomena on electrodes is the *electrical cell impedance sensing* (ECIS) system. Gold electrodes are evaporated into cell culture wells and cells are grown on top in tissue culture medium. The initial system consisted of a large counter electrode with a diameter of $2cm^2$ and small electrodes with a diameter in the range of $10^{-4}cm^2$ (Giaever and Keese [1984])(Figure 2.11). In the meantime a variety of assays has been developed based on this system. The electrodes vary in size from $25\,\mu m$ to $250\,\mu m$ depending on the application and are evaporated in up to 96 well plates. Cells are then cultured on the electrodes and subjected to a small alternating electric field of defined frequency. Application of the electric field (4000Hz, 1V) results in a voltage drop at the boundary between solution and electrode of a few mV and a current density of a few mA/cm^2. The attached cells act as insulating particles and constrain the current flow, forcing it to flow beneath and between the cells. This can lead to an up to 8-fold increase of the measured impedance, which is then followed over time.

A simple model is used to calculate the specific resistance (for a unit area) of a cell-covered electrode (Figure 2.12) as a function of the frequency ν. It is based on the measured specific impedance $Z_n(\nu)$ of a cell-free electrode, the specific impedance through the cell layer $Z_m(\nu)$ and the resistivity ρ of the cell culture medium. The cells are approximated as disks with the radius r_c. The current is assumed to flow radial in the space between the ventral surface of the cells and

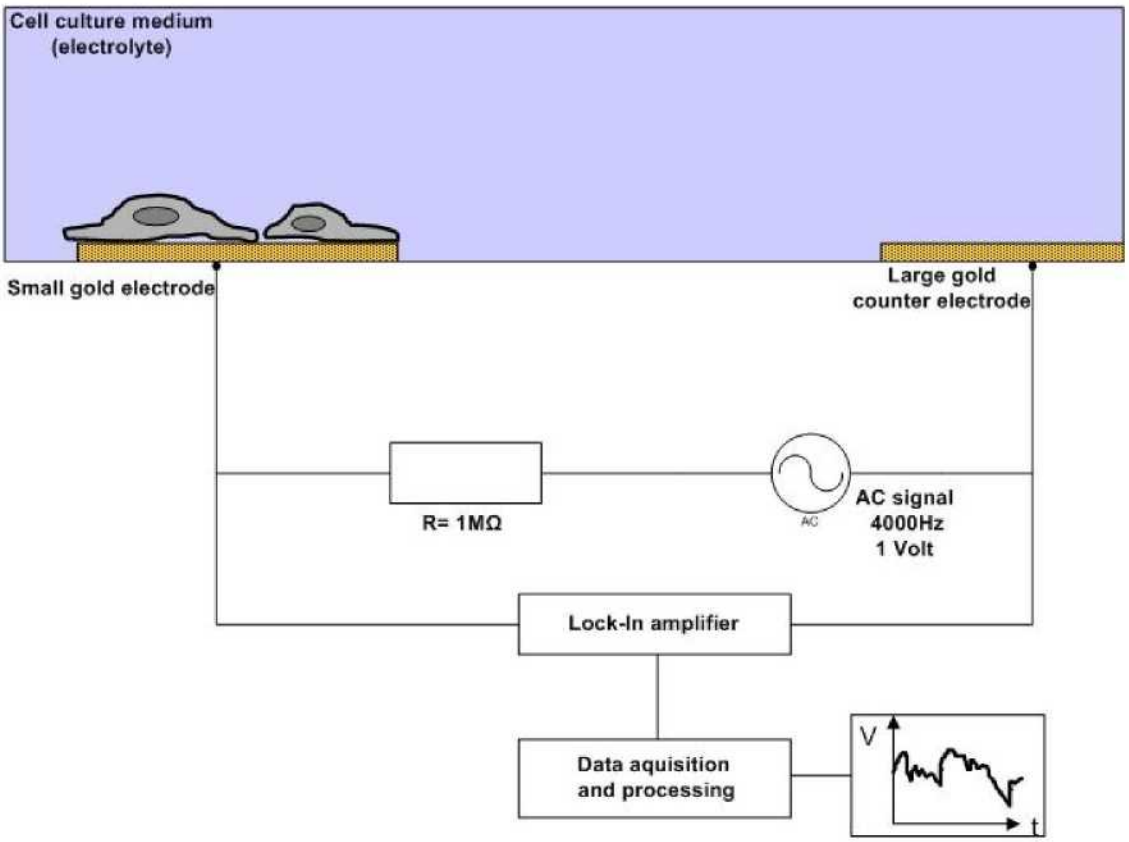

Figure 2.11: The electrical cell-substrate impedance sensing (ECIS) setup (Lo et al. [1995]). Cell layers are cultured on small gold electrodes. The impedance is then altered by the cells, acting as insulating particles. By comparison to the cell free large counter electrode, adhesion and motility are observed. Data is acquired and processed by a personal computer.

the substrate with a constant current density. Another conductive path is given by outflowing current between the cells. $Z_n(\nu)$ is the specific impedance of the electrode-electrolyte interface, whereas $Z_m(\nu)$ is given by $Z_m(\nu) = \frac{-i}{2\pi\nu(C_m/2)}$ with the single cell membrane capacitance C_m. C_m is set to a typical value of $1\,\mu F/cm^2$.

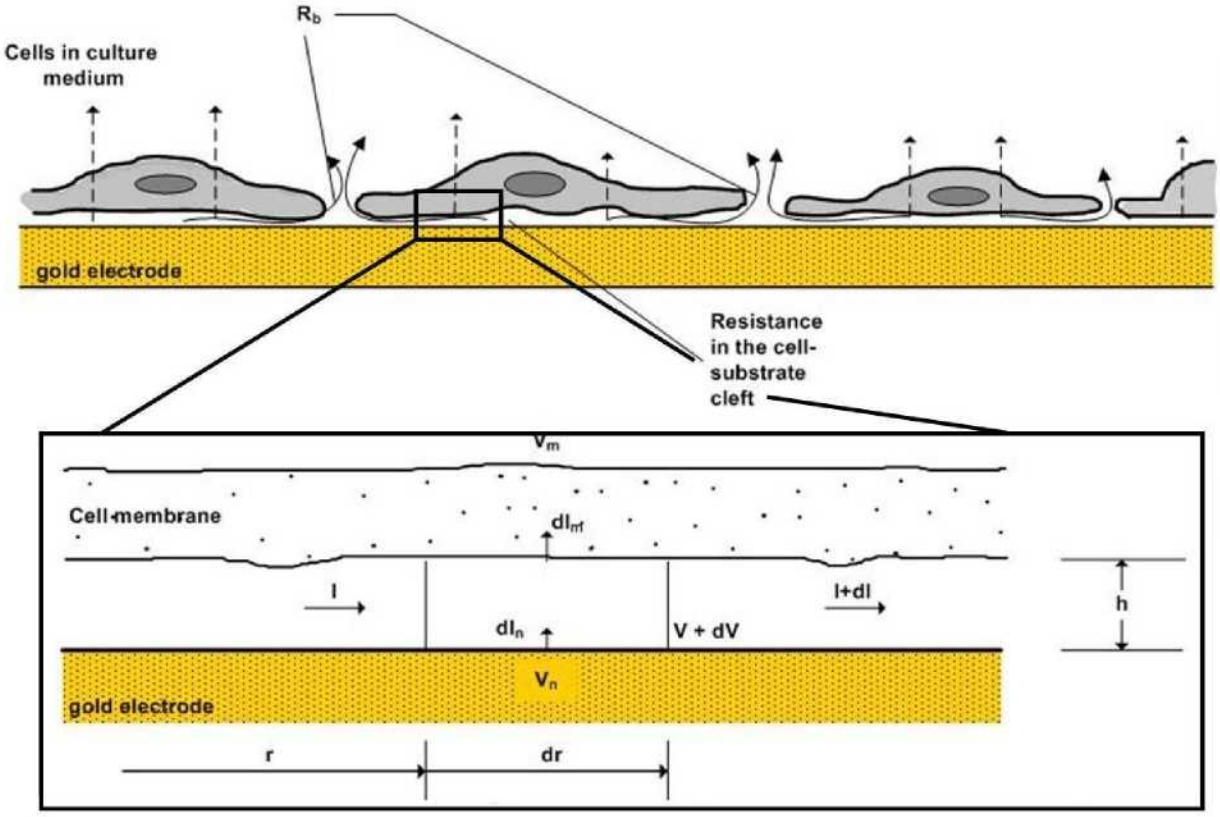

Figure 2.12: Schematic of current flow on ventral side of the cell layer and in between the cell gaps (Giaever and Keese [1991]). Two electrical pathways contribute: through the cells (dotted arrows) or through the cleft and between the cell gaps (solid arrows). h is the cleft height. dI, dV and dr refer to infinitesimal changes of current I, voltage V and distance r, respectively. The subscript m denotes the membrane, whereas n denotes the electrode side.

$$-dV = \frac{\rho dr}{h 2\pi r} I \tag{2.15}$$

$$V_n - V = \frac{Z_n(\nu)}{2\pi r dr} dI_n \tag{2.16}$$

$$V - V_m = \frac{Z_m(\nu)}{2\pi r dr} dI_m \tag{2.17}$$

$$dI = dI_n - dI_m \tag{2.18}$$

These assumptions lead to the differential equation 2.19:

$$\frac{dV^2}{dr^2} + \frac{1}{r}\frac{dV}{dr} - \gamma^2 V + \beta = 0 \tag{2.19}$$

where

$$\gamma^2 = \frac{\rho}{h}\left(\frac{1}{Z_n(\nu)} + \frac{1}{Z_m(\nu)}\right) \tag{2.20}$$

and

$$\beta = \frac{\rho}{h}\left(\frac{V_n}{Z_n(\nu)} + \frac{V_m}{Z_m(\nu)}\right) \tag{2.21}$$

V_n is the potential of the electrode and V_m the potential measured just outside the cell layer in solution. h is the distance of the cell membrane from the substratum.
The equation 2.19 is solved by a sum of modified Bessel functions of first ($I_0(\gamma r_c)$) and second kind ($I_1(\gamma r_c)$). The specific impedance for a cell-covered electrode is then given by 2.22:

$$\frac{1}{Z_c} = \frac{1}{Z_n}\left(\frac{Z_n}{Z_n + Z_m} + \frac{\frac{Z_m}{Z_n+Z_m}}{\frac{i\gamma r_c}{2}\frac{I_0(\gamma r_c)}{I_1(\gamma r_c)} + 2R_b\left(\frac{1}{Z_n} + \frac{1}{Z_m}\right)}\right) \tag{2.22}$$

The solution depends on two factors: the resistance between the cells for a unit area R_b and a factor α, which is given by 2.23.

$$\gamma r_c = r_c\sqrt{\frac{\rho}{h}\left(\frac{1}{Z_n} + \frac{1}{Z_m}\right)} = \alpha\sqrt{\frac{1}{Z_n} + \frac{1}{Z_m}}. \tag{2.23}$$

With this method, cell attachment and cell spreading (Keese and Giaever [1991]) can be monitored. When the electrodes are precoated with pure protein (extracellular matrix components, e.g. fibronectin or laminin), cells show an attachment behaviour correlated to the protein coating (Keese and Branner [1993]). Cell locomotion and micromotion (Wegener et al. [2000]) can be measured, giving a lateral resolution in the nm-range (Keese and Branner [1993]). Furthermore cell responses to biological and chemical compounds (e.g. Triton X100, Cytochalasin B) can be aquired, as cells change their morphology (Keese and Giaever [1994], Keese et al. [1998]). This information is especially useful for toxicology studies. In wound-healing experiments, confluent cell layers of various kidney cell types were mechanically disrupted. Once cell motion was not inhibited by cell-cell adhesion any longer, cells started to repopulate the ruptured area. This was followed over time (Keese et al. [2004]).

2.3.2 Impedance measurements with field-effect devices

For a theoretical description of the impedance signals from single cells presented in this thesis, a theoretical model needs to be developed. This is done in the chapter Results. In this section the different models used in literature are reviewed. With *ion-sensitive field-effect devices* (ISFETs) impedance spectroscopy is used to examine a variety of biomaterials like cells or protein layers of various compositions (Schasfoort et al. [1989]). First attempts to characterize cell adhesion with field-effect devices emerged from the research of neuronal cell-sensor coupling to gain further information about the the cleft between cell and sensor (Fromherz et al. [1993], Weis et al. [1996]).

As cell adhesion determines the cleft geometry, it can influence the local voltage in the junction area and hence affect the activity of ion channels and neuronal signal propagation (Fromherz and Stett [1995]). For impedance measurements, a voltage change can be induced by contacting the cell directly with a patch-clamp pipette or indirectly by an applied voltage via a bath electrode. When the membrane voltage V_M is changed directly, the ac modulation couples through the membrane into the cleft between cell and transitor. The resulting change in the drain-source current and hence the change of the voltage in the cleft V_J is measured (Fromherz et al. [1993], Weis et al. [1996]). For an applied voltage V_E to the electrolyte, the voltage can either couple through the membrane or follow the ohmic path through the cleft. Reference measurements in both cases are accomplished with transistors without attached cells. The Nyquist plot of impedance of an adherend neuron, which is contacted with two patch-clamp pipettes shows a double semicircular pattern. From this, the equivalent circuit of a membrane with a pipette is assumed to be given by two pairs of resistors and capacitors (one for the contact of the patch-pipette to the cell and one for the cell membrane). With this circuit, the values for capacitances and resistances can be fitted (Equations 2.24 and 2.25).

$$\begin{aligned} R_M &= 6.82\,M\Omega \\ C_M &= 802\,pF \\ \tau_M &= 5.5\,ms \end{aligned} \qquad (2.24)$$

R_M: Membrane resistance for whole membrane

C_M: Membrane capacitance for whole membrane

τ_M: Relaxation time of membrane

$$\begin{aligned} R_A &= 1.85\,M\Omega \\ C_A &= 16.8\,pF \end{aligned} \qquad (2.25)$$

R_A: Access resistance of pipette

C_A: Access capacitance of pipette

To model the neuron-sensor contact with the neuron adressed via a patch-clamp pipette, the point-contact model (Figure 2.10 and simplified in Figure 2.13 (a)) or the sheet-contact model (Figure 2.13 (b)) are used. The cleft between transistor and membrane has a sheet resistance ρ_J/d_J given by the distance of the membrane to the transistor d_J and the specific resistance of the electrolyte ρ_J, which leads to a global junction resistance R_J. The circuit is defined by the capacitance C_{JM} and the resistance R_{JM} of the membrane in the junction area, the capacitance C_{JG} of the gate oxide in the junction and the resistance R_J. The frequency-dependend transfer-function is determined by Kirchoff´s laws (Equation 2.26).

$$h(\omega) = \left(1 + \frac{R_{JM}}{R_J}\frac{1 + i\omega R_J C_{JG}}{1 + i\omega R_{JM} C_{JM}}\right)^{-1} \qquad (2.26)$$

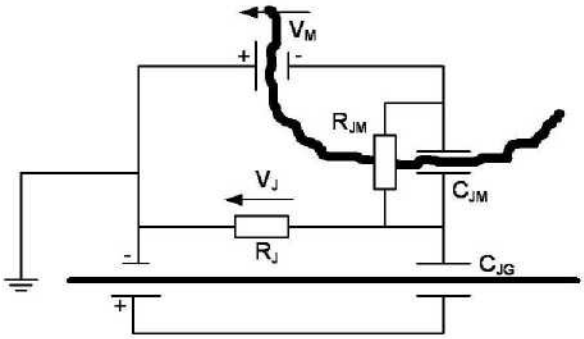

(a) Simplified point-contact model with capacitances of the membrane C_{JM} and the gate oxide C_{JG} in the contact region, as well as the resistances of the membrane R_{JM} and the cleft R_J. The membrane voltage V_M is controlled with a patch-clamp pipette. (The figure was adapted from Fromherz et al. [1993].)

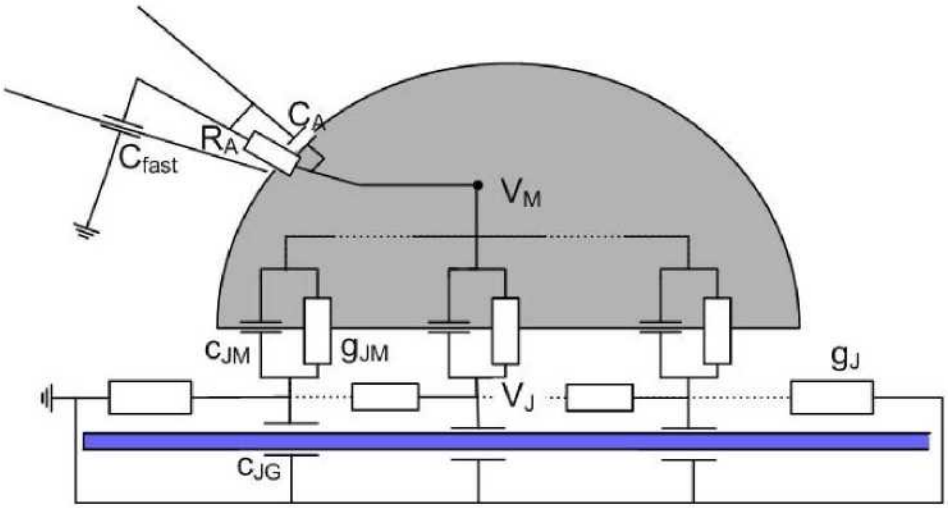

(b) Sheet-contact model with patch-clamp pipette sealed to the cell. The pipette parameters are given by access resistance R_A and capacitances C_A and C_{fast}. The modulated membrane voltage V_M couples through the membrane with specific conductance g_{JM} and capacitance c_{JM} to the cleft (specific conductance g_J). The modulated junction voltage V_J is sensed by the transistor (specific capacitance of gate oxide c_{JG}).

Figure 2.13: Equivalent electrical circuits for the cell-transistor junction with the cell contacted by a patch pipette.

In terms of amplitude |h| and phase φ_h the transfer-function has the form of Equation 2.27.

$$\begin{aligned} |h|^2 &= h_0^2 \frac{1}{1+(\omega\tau_J)^2} + h_\infty^2 \frac{(\omega\tau_J)^2}{1+(\omega\tau_J)^2} \\ tan(\varphi_h) &= \frac{1}{\omega\tau_J + 1/\omega\tau_{JM}} \left(1 - \frac{\tau_J}{\tau_{JM}}\right) \end{aligned} \tag{2.27}$$

The influence of the single parameters depends on the applied frequency. For low frequencies the resistive path dominates (Equation 2.28), while the voltage transfer is determined by the capacitive path for higher frequencies (Equation 2.29).

$$h_0(\omega) = \frac{R_J}{R_J + R_{JM}} \tag{2.28}$$

$$h_\infty(\omega) = \frac{C_{JM}}{C_{JG} + C_{JM}} \tag{2.29}$$

$$\begin{aligned} \tau_{JM} &= R_{JM}\, C_{JM} \\ \tau_J &= R_J\, (C_{JM} + C_{JG}) \end{aligned} \tag{2.30}$$

Instead of the absolute values, specific values can be used for capacitances and resistances (Equations 2.31 and 2.32). The junction area is given by $a_J^2\,\pi$ for the cell radius a_J.

$$\begin{aligned} C_{JM} &= c_{JM}\, a_J^2\, \pi \\ C_{JG} &= c_{JG}\, a_J^2\, \pi \end{aligned} \tag{2.31}$$

$$\begin{aligned} R_{JM} &= (g_{JM}\, a_J^2\, \pi)^{-1} \\ R_{JG} &= (g_J\, a_J^2\, \pi)^{-1} \end{aligned} \tag{2.32}$$

The time constants τ_{JM} and τ_J are determined from experimental data (Bekkers [2006]), some typical values are assumed for c_G and c_M and the set of parameters C_{JG}, C_{JM}, R_{JM} and R_J is fitted. This has been done for retzius cells and rat neurons (Vassanelli [1997]). The parameters for retzius cells are given as an example. From the time constants $\tau_{JM} = 10\,ms$ and $\tau_J = 55\,\mu s$ and with the capacitances $c_G = 0.3\mu F/cm^2$ and $c_M = 3\mu F/cm^2$, the parameters C_{JG}, C_{JM}, R_{JM} and R_J are obtained (Equations 2.33 and 2.34).

$$\begin{aligned} C_{JG} &= 2\,pF \\ C_{JM} &= 20\,pF \end{aligned} \tag{2.33}$$

$$\begin{aligned} R_{JM} &= 0.5G\Omega \\ R_J &= 2.5M\Omega \end{aligned} \tag{2.34}$$

For the sheet-contact model the application of Kirchhoff's laws leads to a partial differential equation as generalization of the usual cable theory (Weis et al. [1996]). For a homogenous stimulation V_M in the neuron, the amplitudes of the junction voltage are obtained (Equation 2.35). The left-hand side of 2.35 refers to the ohmic and capacitive current through the membrane, while the right-hand side describes the ohmic current through the cleft.

$$(1 + i\omega\tau_{JM})(V_J - V_M) = (\lambda^2\Delta - i\omega\tau_{JG})V_J \tag{2.35}$$

$$\begin{aligned} \tau_{JM} &= \frac{c_{JM}}{g_{JM}} \\ \tau_{JG} &= \frac{c_{JG}}{g_{JM}} \\ \lambda &= \frac{1}{\sqrt{g_{JM}\rho_J/d_J}} \end{aligned} \tag{2.36}$$

c_{JM}: Specific capacitance of junction membrane

c_{JG}: Specific capacitance of gate oxide in the junction area

g_{JM}: Specific conductance of junction membrane

λ: Length constant

Assuming a contact area with the radius a_J and the boundary condition $V_J(a) = 0$ at $a = a_J$ the voltage transfer along the radius a is obtained (Equation 2.37). I_0 is the modified Bessel function of the order zero and λ_ω^2 is the complex squared length constant with $\lambda_\omega^2 = \lambda^2/[1+i\omega(\tau_{JM}+\tau_{JG})]$.

$$\frac{V_J(\omega, r)}{V_M(r)} = \frac{1 + i\omega\tau_{JM}}{1 + i\omega(\tau_{JM} + \tau_{JG})} \left[1 - \frac{I_0(r/\lambda_\omega)}{I_0(r_J/\lambda_\omega)}\right] \tag{2.37}$$

Using realistic values for c_{JM}, c_{JG}, g_{JM} and g_J the sheet resistance ρ_J/d_J is fitted to 46 $M\Omega$. From this the width of the cleft is determined to 22 nm.

Although this method delivers realistic values for several parameters associated with cell adhesion, it cannot be applied to all cellular systems. Model systems like membrane vesicles or erythrocyte ghosts have a more fragile membrane and thus, patch clamping cannot be used. The ac voltage is applied to the bath with a AgAgCl electrode instead. The equivalent circuit is again given by the point-contact or sheet-contact model with some modifictaions (Figure 2.14).

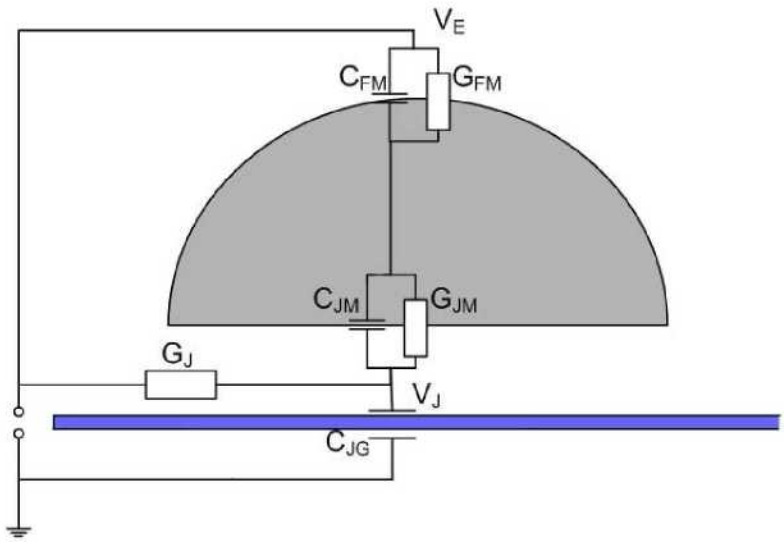

(a) Modified point-contact model for a setup with the voltage V_E applied to the bath via a Ag/AgCl electrode. Two fractions of the membrane now contribute to the circuit with capacitances C_{FM}, C_{JM} and conductances G_{FM}, G_{JM} for free and attached membrane, respectively. G_J denotes the junction conductance and C_{JG} is the capacitance of the gate oxide.

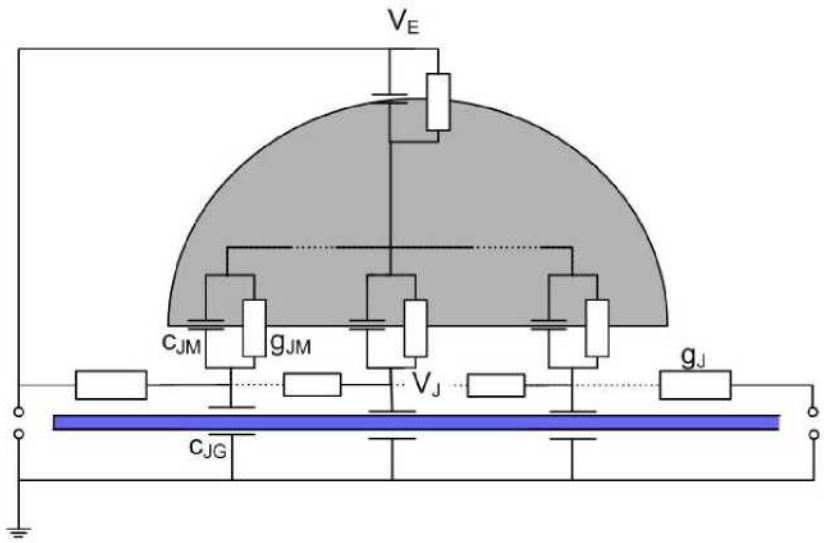

(b) Sheet-contact model for a setup with the voltage V_E applied to the bath via a Ag/AgCl electrode. The specific capacitances c_{JM}, c_{JG} and the specific conductances g_{JM}, g_J determine the circuit.

Figure 2.14: Equivalent electrical circuits for a cell on a transistor with the voltage V_E applied via a bath electrode. The change in the junction voltage V_J is sensed by the transistor.

For erythrocytes the point-contact model is prefered, as the relative position of ghost and transistor is difficult to determine (Kiessling et al. [2000]). For a low conductance of the membrane, the approximations $g_{JM}A_{JM} \ll G_J$ and $g_{FM}A_{FM} \ll G_J$ are made with $G_J = A_{JM}g_J$. The fraction of the attached membrane area is given by the parameter $\alpha = A_{JM}/(A_{JM} + A_{FM})$. The transfer-function is obtained again by applying Kirchoff's laws (Equation 2.38).

$$\begin{aligned} h(\omega) &= \frac{1+i\omega\tau_J h_\infty}{1+i\omega\tau_J} \\ h_\infty &= \frac{(1-\alpha)c_M}{1-\alpha)c_M + c_{ox}} \\ \tau_J &= \frac{(1-\alpha)c_M + c_{ox}}{g_J} \end{aligned} \tag{2.38}$$

From the fit of the experimental data, τ_J is determined to 5.9 μs. With the membrane capacitance $c_M = 0.9\,\mu F$ and the fraction of attached membrane $\alpha = 0.33$ the seal conductance is calculated to $g_J = 136 mS/cm^2$.

For membrane vesicles the sheet-contact model is applied to evaluate the specific resistance g_M of the membrane and the sheet resistance g_J of the cleft (Fromherz et al. [1999]). The transfer-function obtained from the sheet-contact model by Kirchhoff's laws is given by Equation 2.39.

$$\frac{V_J(\omega, a)}{V_E(\omega)} = \frac{I_0(\gamma a)}{I_0(\gamma a_J)} + \frac{\gamma_M}{\gamma_M + i\omega c_{JG}}\left[1 - \frac{I_0(\gamma a)}{I_0(\gamma a_J)}\right] \tag{2.39}$$

$$\begin{aligned} \gamma^2 &= g_J(\gamma_M + i\omega\, c_{JG}) \\ \gamma_M &= (g_M^{-1} + i\omega\, c_M)/(1+\alpha) \end{aligned} \tag{2.40}$$

For $a_J = 25\,\mu m$, $\alpha = 0.7$ and $c_M = 0.6\,\mu F$ the sheet resistance is determined to 50 to 130 GΩ for different vesicles and the resistance of the membrane is fitted to a value of $R_M > 1\,M\Omega\,cm^2$. Therefore, the adhesion of cells and cellular systems can be characterized with parameters drawn from the described equivalent circuits.

However, besides cell adhesion, various other biomaterials can be examined with the method of impedance spectroscopy with field-effect devices. Changes in the resistance of artificial membranes (PVC, polysiloxane) bound to the transistor surface (*chemically modified FETs* CHEMFETs) are observed by transfer-function measurements. For cation-sensitive sensors, the resistance decreases upon addition of receptors, lipophilic borate salts (Gehrig et al. [1990]) or combinations of lipophilic cations and anions (Ammann et al. [1985]). With ongoing leaching of those

substances, the resistance decreases again (Armstrong and Todd [1986]). On the other side, the resistance can be decreased for anion-selective membranes with an increasing concentration of ammonium sites, while addition of receptors only results in a minor effect (Antonisse et al. [2000]). The equivalent circuit of such membranes, which are physically adsorbed to FETs, consists of a bulk impedance contribution in series with the surface contributions (Figure 2.15). The membrane bulk impedance is given by a resistance R_{mem} in parallel with a capacitance C_{mem}. The interfacial section is then described by a double-layer capacitance C_{DL} in parallel with the resistance of the charge transfer at the interface R_{CT} and a Warburg impedance W, which describes the diffusion of ions. For the ISFET, a silicon-electrode resistance R_{SI} contributes in series with the space charge capacitance C_{SC} and the gate oxide capacitance C_{ox}. The resistance of the counter electrode and the electrolyte are denoted as R_{sol}. For frequencies higher than 5 kHz the interfacial contributions are neglected. R_{sol} is also neglected as it is of several orders of magnitude smaller than R_{mem}. This leads so a simplified equivalent circuit, in which C_{ox} is in series with a resistance R_{mem} and parallel to the capacitance C_{mem} (Figure 2.16). These components determine the time constant τ, which states the time needed to establish electrical profiles in the membrane by redistribution of charges. In the measurement setup a sinusoidal ac voltage is applied with a platinum electrode (Figure 2.17). The variations in the gate-source voltage V_{GS} due to changes in the membrane can be monitored as changes in the drain-source current I_{DS}. The output voltage V_{out} is then given as Equation 2.41 with the transconductance of the transistor g_m and the feedback resistance R in the amplification stage (Equation 2.41).

$$V_{out} = -R\,I_{DS} = -R\,g_m\,V_{GS} \tag{2.41}$$

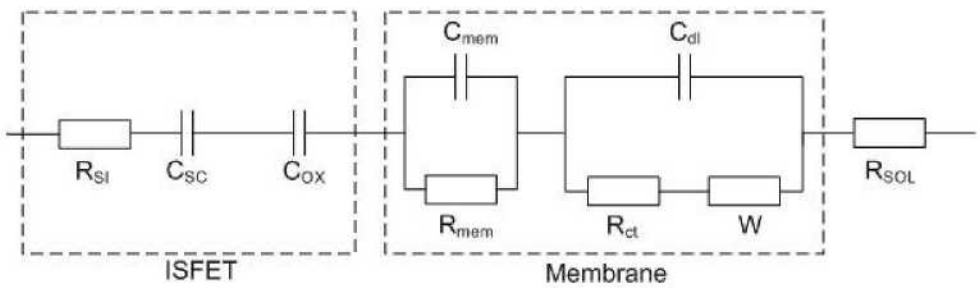

Figure 2.15: Equivalent electrical circuit for a membrane with a capacitance C_{mem} and a resistance R_{mem} on a FET with gate capacitance C_{ox}. R_{SI}, R_{CT} and R_{sol} denote the resistances in the silicon, the charge transfer at the interface of membrane and solution and the solution itself. Ion diffusion contributes with a Warburg impedance.

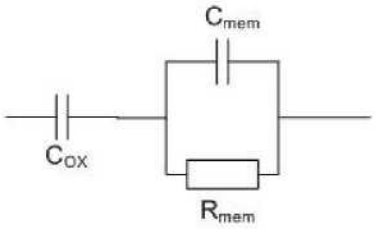

Figure 2.16: Simplified electrical circuit for a membrane with a capacitance C_{mem} and a resistance R_{mem} adsorbed to a FET with gate capacitance C_{ox}.

When a membrane is deposited on the gate, the gate-source voltage is divided over the polymer and the gate oxide. Therefore, the transfer-function is introduced as a multiplication factor of V_{GS} (Equations 2.42 and 2.43).

$$H(i\omega) = \frac{1 + i\omega R_{mem} C_{mem}}{1 + i\omega R_{mem}(C_{mem} + C_{ox})} \tag{2.42}$$

$$V_{out} = -Rg_m H(i\omega) V_{GS} \tag{2.43}$$

For this transfer-function two time constants are determined (Equations 2.44 and 2.45). As C_{ox} is usually 100 times larger than C_{mem} an approximation can be made. Therefore τ_1 serves as indicator for the membrane resistance and τ_2 gives the relaxation time of the polymeric membrane.

$$\tau_1 = R_{mem}(C_{mem} + C_{ox}) \approx R_{mem} C_{ox} \tag{2.44}$$

$$\tau_2 = R_{mem} C_{mem} \tag{2.45}$$

$$C_{mem} = \frac{\epsilon_0 \epsilon_{mem} A}{d_{mem}} \tag{2.46}$$

With a setup like this, biorecognition processes on protein-modified FETs can be examined. Enzyme-labeled antigens or antibodies can be employed as conjugates, which induce changes in the gate potential upon antigen-antibody recognition (*enzyme-based FET* (ENFET)) (Kharitonov et al. [2000], Kharitonov et al. [2001b]). Those systems are usually embedded in a polymer membrane associated with the gate interface. Again, capacitive or impedance changes are analysed as result of alterations in chemical composition of the membrane (Kharitonov et al. [2001a]). Hence, the equations 2.41 to 2.45 can be applied for those systems.

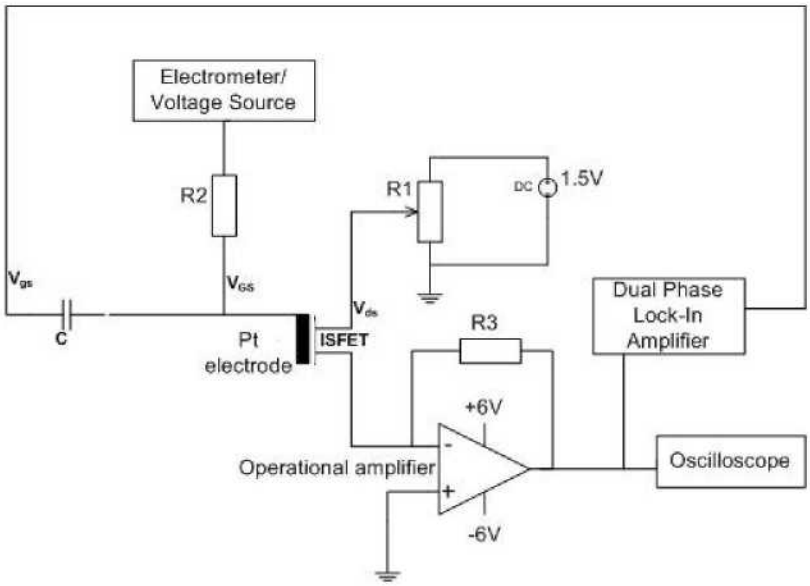

Figure 2.17: Schematic of the setup to measure the transfer-function of a membrane on a FET. The voltage is applied with a platinum electrode. The measured drain-source current is changed to a voltage, amplified with an operational amplifier and monitored with an oscilloscope.

Chapter 3

Materials and Methods

This chapter is divided into two sections. The first section covers the chip processing, while the second section includes methods and materials of the transfer function measurements. The section on chip processing includes the chip design and fabrication of the planar FETs and the buried-channel FETs, as well as the methods used for their characterization. In the section on transfer function measurements, the general setup is explained and the cell experiments are introduced. These cover cell adhesion, apoptosis, vesicles and erythrocyte ghosts as model systems, and cell migration.

3.1 Chip processing

In this work, an open-gate p-FET with a planar surface was designed and fabricated. As an extension of the process, buried-channel FETs were designed and built. The following subsections cover chip design and fabrication. The detailed process flow is provided in the appendix.

3.1.1 Chip design

The fabrication process was based on a former open-gate p-FET (Juelich FET) design with respect to basic process parameters (e.g. implantation doses), transistor pitch, dimensions of conducting lines (drains and common source), bond pads and chip size. 16 transistors in a 4x4 array with a distance of 200 μm were placed in the middle of a (5x5) mm^2 chip (Figure 3.1).

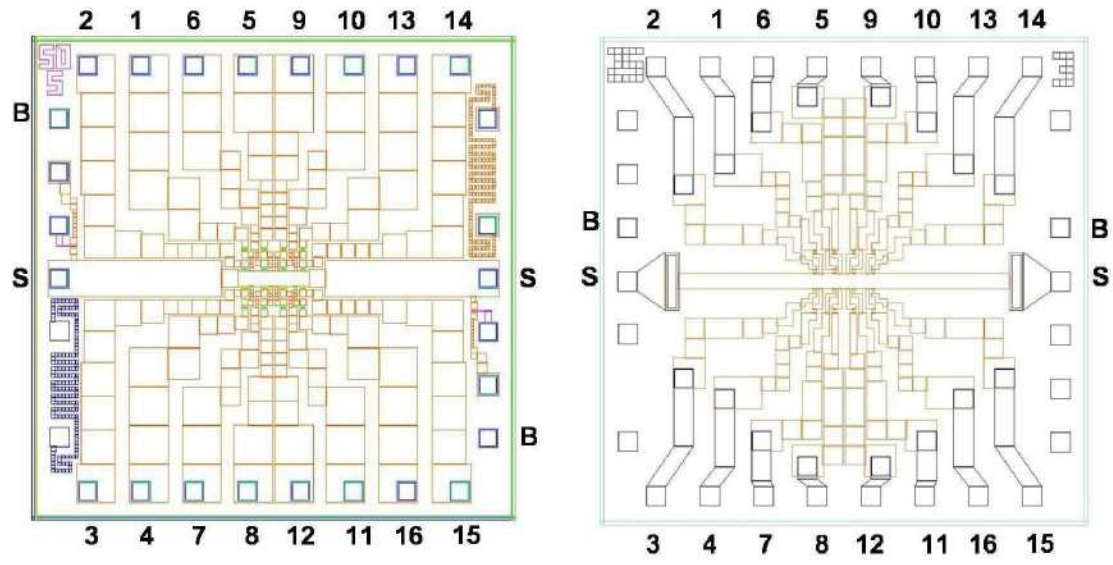

Figure 3.1: Layout of the former Juelich FET (a) and the planar FET (b) fabricated in this work. The contacts include bulk (B), common source (S) and the sixteen drain feed lines (1-16). While the Juelich FET has implanted feed lines with metal contacts, the planar drains consist of half implanted and half metalized feed lines.

Conducting line capacitance and resistivity

To accomplish comparable cell measurements with each transistor on the chip, all transistors must have the same properties. For this reason, conducting line capacitance and resistance should be identical. The former Juelich p-FET process was already optimized regarding low resistivity. Nevertheless, the capacitance still varied due to different areas of the drain lines. This problem was overcome in the planar process of this work. All 16 drains were designed with identical surface area and identical resistivity. This could only be achieved by shortening the implanted part of the feed lines and elongate their metalized part (Figure 3.1). Source and drain capacitance and resistivity of both processes are compared in Table 3.1. The capacitance was calculated with Equations 3.1 and 3.2. Capacitance and resistance of the feed lines were used to calculate the cut-off frequency of the transistors transfer function (Equation 3.3). Note that only the area in direct contact to the electrolyte after encapsulation was taken into account for the calculation (circle with diameter $\mathbf{2.8}\,mm$ for the planar FET and a circle of 4 mm for the Juelich FET). The resistance of the metalized conducting lines was neglected.

Given the challenge of processing and the aim to use the chip as proof-of-principle design we restricted to 16 transistors per chip, although the general trend goes to higher integrated systems. The chosen design is very suitable for single cell measurements. Nevertheless, transistor arrays with 256 and 1024 transistors in square grids were designed additionally. As a sufficient

$$C = \epsilon_0 \epsilon \frac{A}{d} \tag{3.1}$$

$$\frac{1}{C_{all}} = \sum \frac{1}{C_i} \tag{3.2}$$

$$f_c = \frac{1}{2\pi R_{el} C} \tag{3.3}$$

C: Capacitance
ϵ_0: Dielectric constant ($8,8542 \cdot 10^{12}$ $[Fm^{-1}]$)
ϵ: Dielectric constant of insulating oxide/nitride (3.8/7.5)
R_{el}: Resistance of the reference electrode and the electrolyte
A: Area of feed line
d: Thickness of insulating layer
C_i: Capacitance of a single insulating layer
C_{all}: Capacitance of a layer stack
f_c: Cut-off frequency

	Juelich FET	**planar FET**
Source capacitance	$96\,pF$	$126\,pF$
Drain capacitance	$49\,pF$ (drains 1,4,13,16); $35\,pF$ (drains 2,3,14,15); $31\,pF$ (drains 5,8,9,12); $39\,pF$ (drains 6,7,10,11)	$47\,pF$ (drains 1,4,13,16); $45\,pF$ (drains 2,3,14,15); $46\,pF$ (drains 5,8,9,12); $45\,pF$ (drains 6,7,10,11)
C_{all}	$145\,pF$; $131\,pF$; $128\,pF$; $135\,pF$	$173\,pF$; $171\,pF$; $172\,pF$; $171\,pF$
Drain resistivity	$192\,\Omega$	$488\,\Omega$
Source resistivity	$94\,\Omega$	$250\,\Omega$
Resistance of electrode and electrolyte	$2\,k\Omega$	$2\,k\Omega$
Cut-off frequency $f_c = \frac{1}{2\pi R_{el} C}$	$600\,kHz$	$460\,kHz$

Table 3.1: Capacitance and resistivity for feed lines in the Juelich and the planar layout.

passivation and encapsulation procedure has yet to be developed, those chips were not used for cell measurements within this work. Still, process documentation shown in the following sections also refers to the large array transistors.

Gate area

For cell measurements, sensing gate areas roughly of the size of a cell diameter or less are most useful. Thus, the cells can cover the whole gate and create a big seal resistance. For smaller model systems like erythrocyte ghosts (subsection 3.2.3) smaller gate widths are required. Additionally, the ratio of gate width to gate length should be big, increasing the transistors transconductance. Hence, we decided to include gatewidths of $25\,\mu$m, $12\,\mu$m and $6\,\mu$m. Gate lengths were set to $3\,\mu$m and $1.5\,\mu$m. In the second run, gate lengths were extended to $5\,\mu$m, $4\,\mu$m and $3\,\mu$m, omitting the short gates ($1.5\,\mu$m) (Figure 3.2).

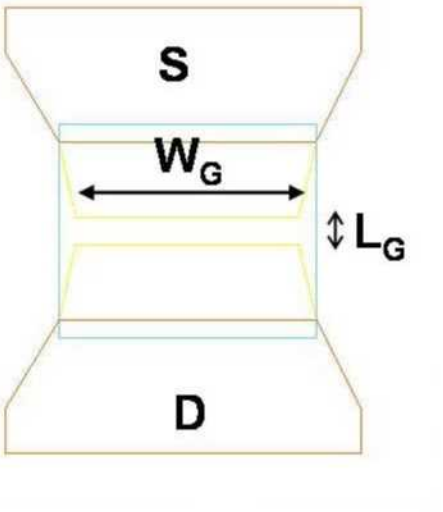

Figure 3.2: Source (S) and drain (D) connect the gate, which is defined by width W_G and length L_G. The gate plateau is shown in blue.

Planarization

For cell adhesion and cell migration experiments, surface topography becomes as important as the intrinsic transistor properties. It is known that cells react highly sensitive to topographical and biochemical cues (Jung et al. [2001], Arnold et al. [2004], Chen et al. [1997], Berry et al. [2004]). These parameters determine cell adhesion and therefore also cell migration and proliferation. Usually, both types of cues are present and hence cannot be distinguished. With a planar device, topographical cues are reduced. For cell measurements, planarity is defined by the cells detection limit. Hence, steps smaller than $30\,nm$ are taken to be planar. Additionally, planar devices might be used for the characterization of fragile biological systems like artificial membranes. For the good quality of surface tethered membranes chips with a very uniform surface are mandatory (Naumann et al. [2003], Atanasov et al. [2005]). Finally, the planar design is a good basis to upgrade the device with additional multi-electrode arrays fabricated on top. Such combined devices could then be used for cell stimulation and detection of electrical cell activity (Wallys [2007]).

One conflict to solve is the need to passivate the conducting lines with an insulating layer of a few hundred nanometers and on the other hand cover the gate only with a thin thermal gate oxide (typical thickness around $10\,nm$). Passivation is normally achieved by an oxide-nitride-oxide stack (ONO-stack), which is then reopened in the gate area by etching. This unavoidably leads to steps of several hundred nanometers in proximity of the gate area. Therefore, this method cannot be used in a planar process. This problem was overcome with an extra lithography, protecting the

gate-plateau with nitride (Figure 3.2), while the rest of the wafer was thermally oxidized to SiO_2 (subsection 3.1.2). This oxide was removed by selective etching to the height of the lower nitride edge. With this process, the substrate oxide formed a passivating layer on top of the conducting lines. Consequently, the gate area was lifted onto a plateau with respect to the conducting lines, ensuring its sensing properties.

3.1.2 Fabrication

The planar FET process was completed twice in the framework of this thesis. In this section, the process is described in a general way, while Table A.3 lists all process parameters in detail (1^{st} and 2^{nd} run). Values given in the text refer to the second run, as it showed improved and stable conditions. The processing equipment is listed in Table A.6 in the appendix.

Conducting lines

Wafers with low n-doping were used as substrate. First of all, $30\,nm$ of oxide were thermally grown and $100\,nm$ of nitride were deposited by LPCVD (low pressure chemical vapour deposition) (Figure 3.3). Drain and source regions were defined by structuring the ON-layer with the

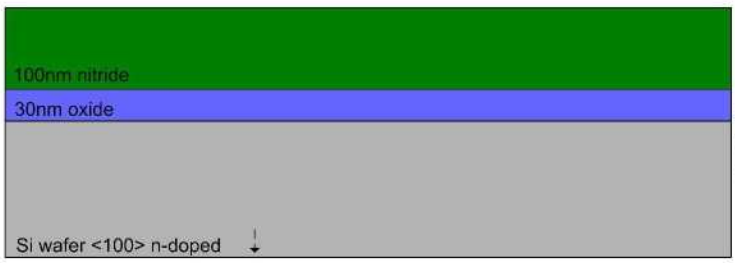

Figure 3.3: Silicon substrate, with deposited oxide and nitride layer. (Not to scale)

1^{st} lithography. The lithography resist was used as a mask for etching the oxide and nitride layer by reactive ion etching (RIE) with CHF_3 gas, as well as an implantation mask. The doping in the conducting line regions was set by a double implantation of boron ions. These implantaions created a combination of gaussian shaped profiles beneath the wafer surface (Sze [1985]). The second implantation was chosen to ensure an overlap with the implanted source and drain extensions at a later process stage. After the nitride and oxide etch, the resist was removed with reactive ion etching using an oxygen plasma.

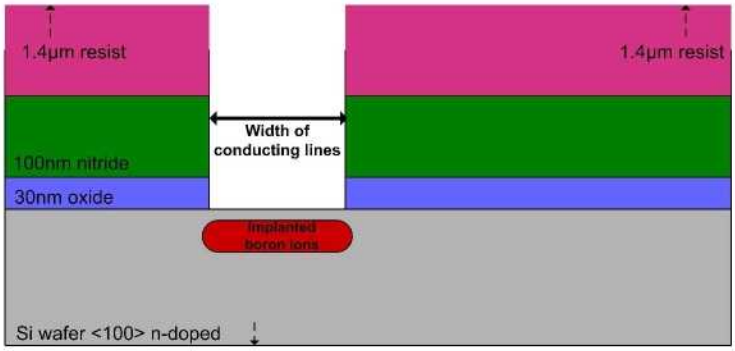

Figure 3.4: Source and drain were structured with the 1^{st} lithography, followed by the first boron implantation. (Not to scale)

Definition of gate plateau

With the 2^{nd} lithography the gate plateau areas were defined (Figure 3.5). Nitride and oxide, which were not covered by resist, were removed by RIE (CHF_3) leaving the gate plateau covered. Afterwards, the resist was removed by RIE (O_2) (Figure 3.5) and the structure was checked optically (Figure 3.6).

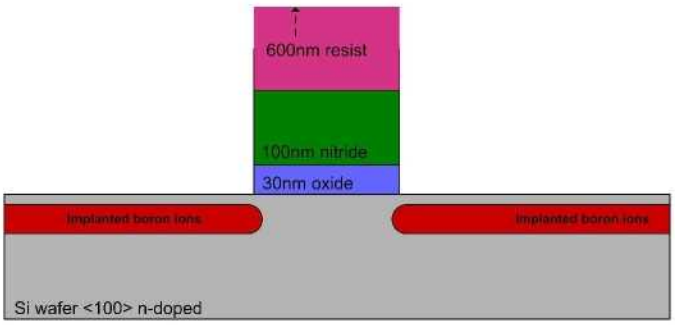

Figure 3.5: The gate plateau was defined with the 2^{nd} lithography. Nitride and oxide were removed. (Not to scale)

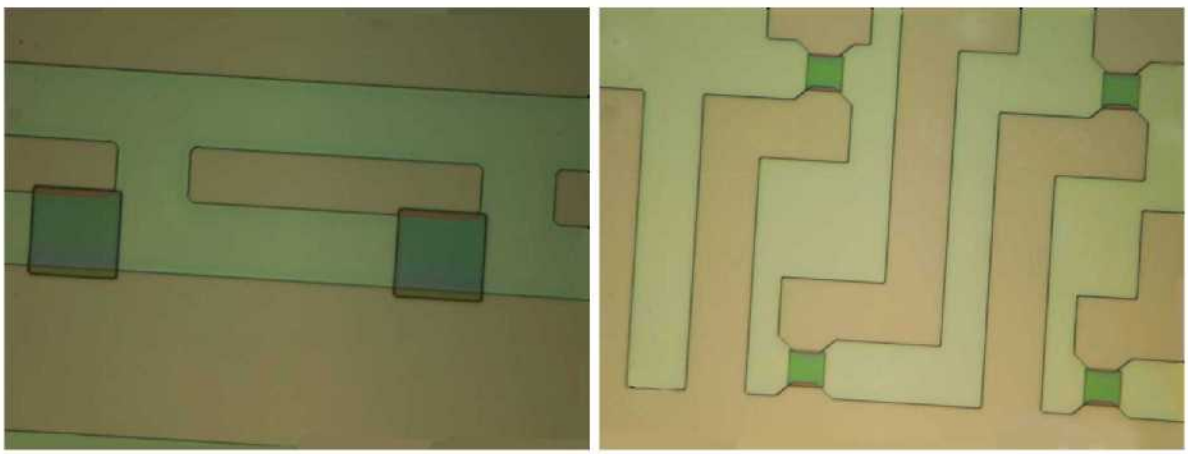

(a) (b)

Figure 3.6: The transistor area was covered by resist, defining the gate plateau. Transistors in a large array (a) and transistors on 16 channel chip (b).

Planarization

The wafers were cleaned with the standard RCA cleaning procedure (details given in Table A.4). To lower the conducting lines and hence lift the gate plateau, a dry LOCOS oxide (Local oxidation of silicon) was grown. The oxide thickness was then determined by ellipsometry (average thickness $\approx 260\,nm$) (Figure 3.7). 44% ($\approx 115\,nm$) of the oxide grew into the substrate, while 56% ($\approx 145\,nm$) grew on top of the surface. The oxidation temperature of 1000°C also activated the implanted boron ions. Consequently, a broadening of the gaussian implantation profile was expected. The planarization step was done with a selective hydrofluoric acid etch (HF 1%) of the

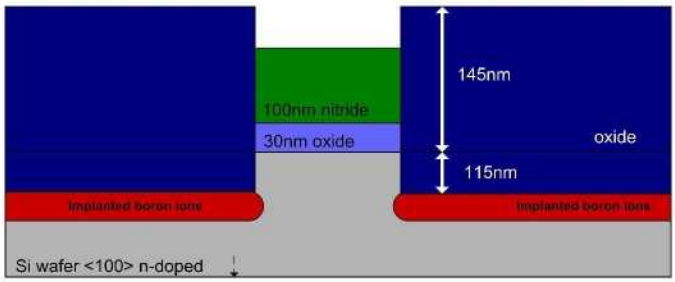

Figure 3.7: The wafer was oxidized around the gateplateau areas. (Not to scale)

LOCOS oxide (Figure 3.8). Step heights were measured before and after etching with a surface profilometer (data shown in chapter Results). After a short HF-dip (1%), the wafers were put

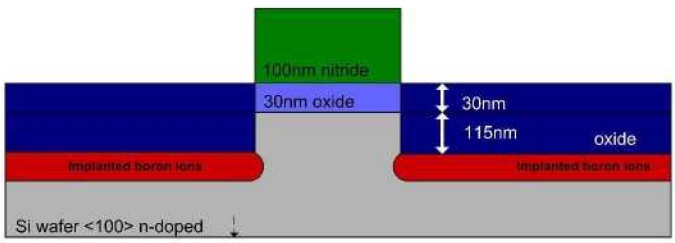

Figure 3.8: The planarization etch was accomplished, etching the oxide until the lower nitride edge was reached. (Not to scale)

into boiling phosphoric acid to remove the nitride layer on the gate plateau. At this point, the achieved planarity was determined (data shown in 4.1). The remaining oxide was thinned to a sacrifical oxide layer (Figure 3.9).

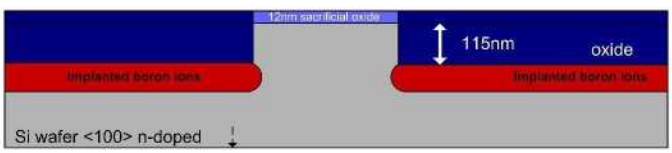

Figure 3.9: All nitride was removed and the oxide was thinned to a sacrificial oxide. (Not to scale)

Definition of gate geometry

Drain and source were defined by the 3^{rd} lithography, also determining the position of the gate areas (Figure 3.10) and the structure was checked optically (Figure 3.11). Boron was implanted to contact the feed lines to source and drain. The resist was removed by RIE (O_2). After a RCA cleaning, the wafers were annealed at 900°C and the grown oxide ($\approx 13\,nm$) was etched away with HF 1%. Subsequently, the dry oxidation of the gate oxide followed.

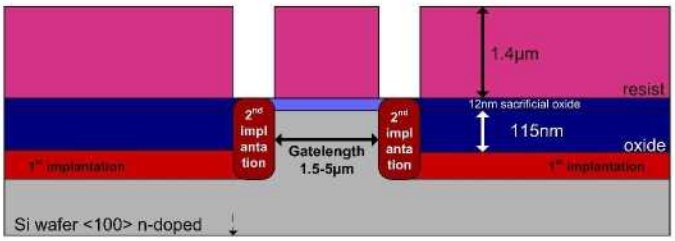

Figure 3.10: The third lithography defined the area of the second source and drain implantation, fixing the gate geometry. (Not to scale)

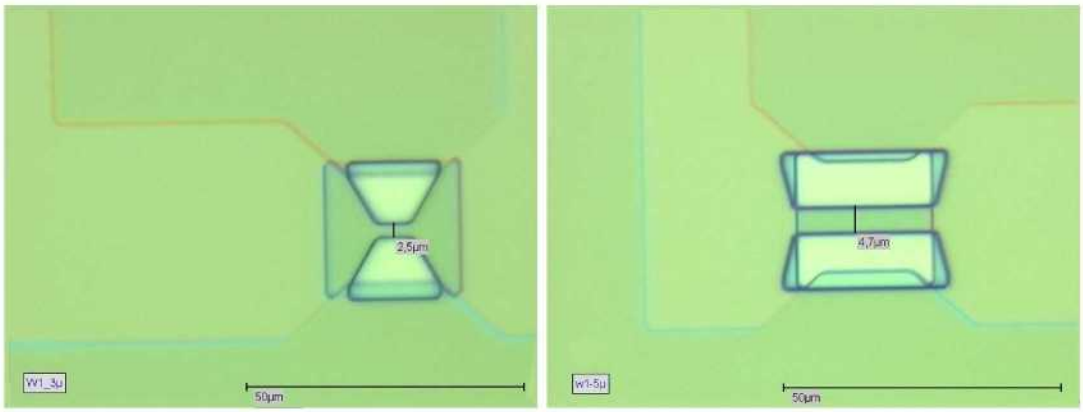

(a) (b)

Figure 3.11: Transistor with gate width x gate length of 6μm x 3μm (a) and 25μm x 5μm (b) after the 3^{rd} lithography and subsequent development.

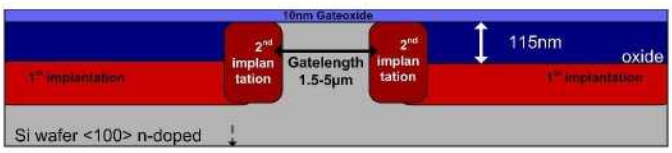

Figure 3.12: After removal of the resist and the sacrificial oxide, a thermal gate oxide was grown. (Not to scale)

Metalization

To apply metal contacts to the implanted source and drain feed lines, the silicon oxide passivation was opened. Contact windows were defined by the 4^{th} lithography. The contact holes were etched by AF91 (buffered hydrofluoric acid 10%) and the resist was removed with acetone. The metal feed lines were defined by the 5^{th} lithography in an image reversal process. Then a triple layer of metal was deposited. Aluminum ($150\,nm$) was chosen to form a good electrical contact to the doped silicon. Gold ($150\,nm$) as top layer was taken to facilitate the encapsulation procedure and Titanium ($10\,nm$) was used as intermediate layer to avoid alloying of Al and Au. The metal layers were defined with a lift-off process, revealing the metal leads. To ensure good electrical contact, the metal was tempered at 325°C. The finished wafers were cut into single chips. Encapsulation of the chips is described in detail in appendix B.1.

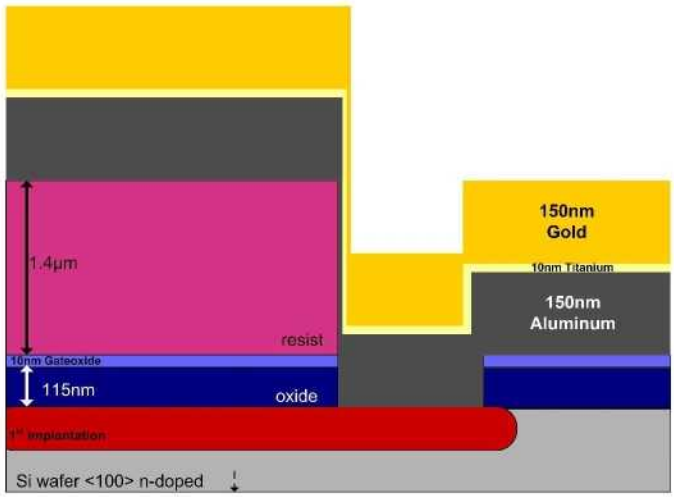

Figure 3.13: Contacts between implanted and metalized feed lines were openend with the 4^{th} lithography. The metal feed lines were defined by the 5^{th} lithography. Al, Ti and Au were deposited. (Not to scale)

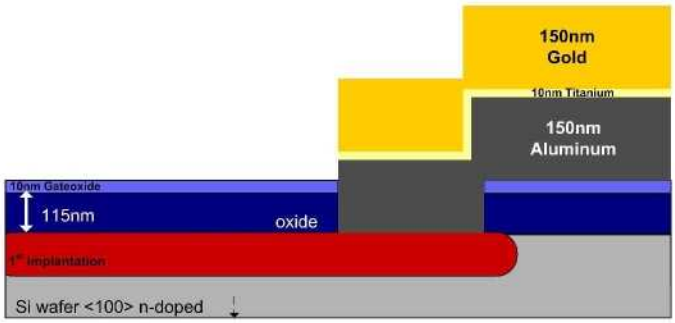

Figure 3.14: The unnecessary metal was removed by lift-off. (Not to scale)

3.1.3 Buried-channel field-effect transistors

Buried-channel FETs were built to improve the noise properties of the FET. As mentioned before, noise can originate from the silicon-oxide interface and hence be reduced by burying the channel into the substrate. For one of the wafers a parameter test for an additional implantation was carried out, placing a buried channel into the gate area and resulting in an depletion-mode FET. The wafer was taken out of the regular process after the source and drain implantation and the subsequent anneal. The oxide was not dipped off, but left as a sacrificial oxide for the additional implantation. The wafer was broken into samples of nine chips each. Every sample held chips of identical gate length, but with three different gate widths. The mask of the 2^{nd} lithography was used to structure the resist in an image reversal process. Hence, the gate plateau area was opened for the implantation, while the surrounding was covered by a resist mask. Boron ions ($7 \cdot 10^{12}/cm^2$) were implanted with varying implantation energies, ranging from 5 to $20\,keV$. Pictures 3.16 and 3.17 show a simulation (SRIM2003) of the channel depth in dependency of the implantation energy. The further process was accomplished as described in the last section (Metalization).

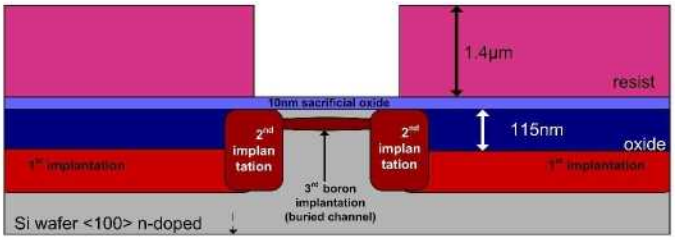

Figure 3.15: The buried channel was defined with an additional lithography followed by a third boron implantation into the gate area. (Not to scale)

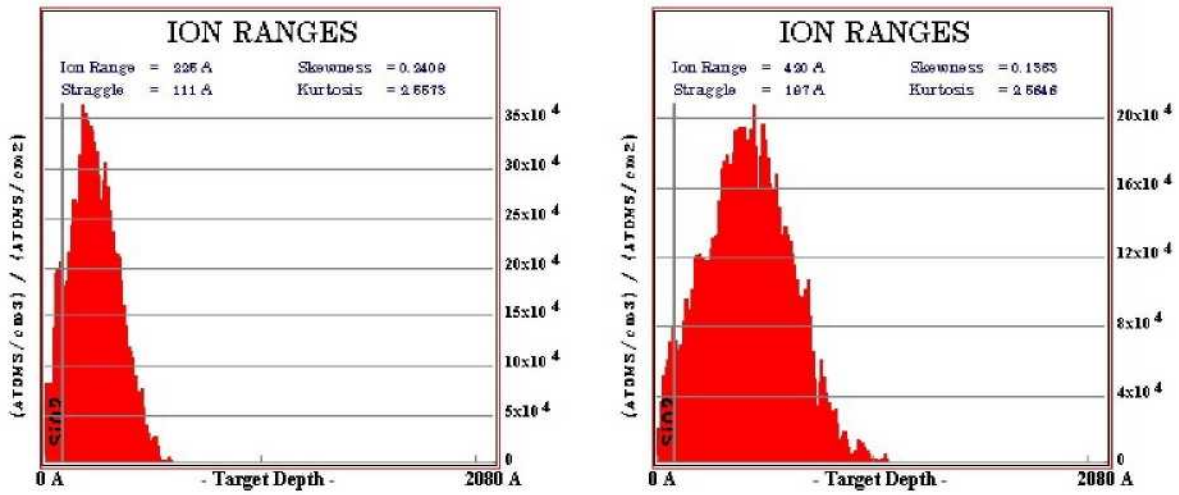

Figure 3.16: Simulated implantation profile for implantation energies of 5keV and 10keV. The channel is buried in an approximate depth of $15\,nm$ and $40\,nm$, respectively. (SRIM2003)

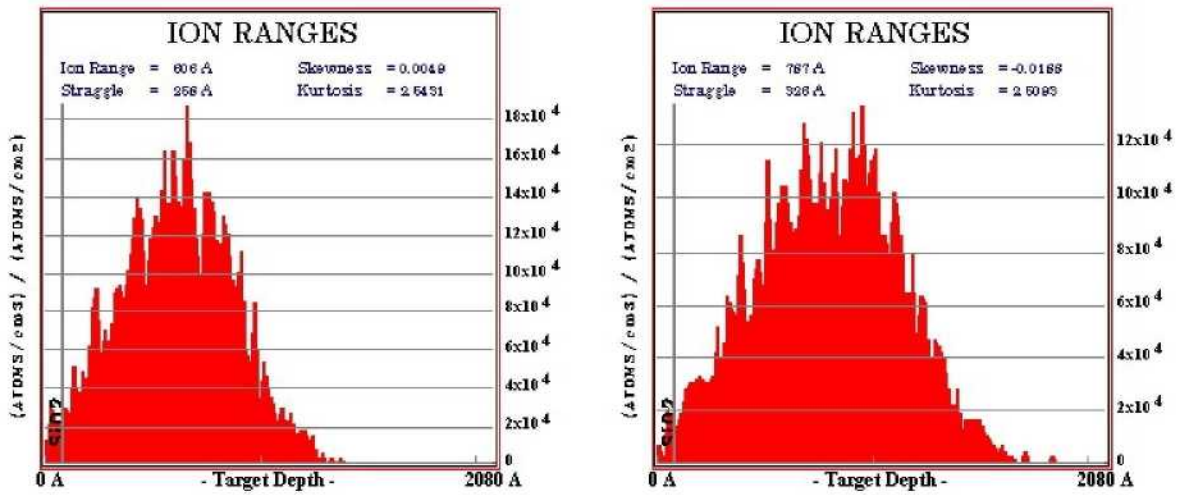

Figure 3.17: Simulated implantation profile for implantation energies of 15 keV and 20 keV. The channel is buried in an approximate depth of $60\,nm$ and $80\,nm$, respectively.(SRIM2003)

3.1.4 Transistor characterization

Characterization with the probestation

Before encapsulation, the chips were characterized at a wafer probe station. The chip was fixed by vacuum and its position was controlled with a light microscope (Figure 3.18). Source and drain were directly contacted by two tungsten pins, while the gate was contacted via a third pin, which was carefully dipped into a droplet of Milli-Q water on the transistor surface (inset of Figure 3.18). The source contact was set to ground (triax wire lead) and negative voltages were applied to drain and gate contacts (coax wire leads), controlled by a software (Kite 6.0, Keithley). Output $I_{DS}(V_{DS})$ and transfer $I_{DS}(V_{GS})$ characteristics were measured. From this data, the transconductance g_m was calculated by derivation of $I_{DS}(V_{GS})$. Threshold voltages and the substhreshold slope were determined from the transfer characteristics as shown in Figure 3.19.

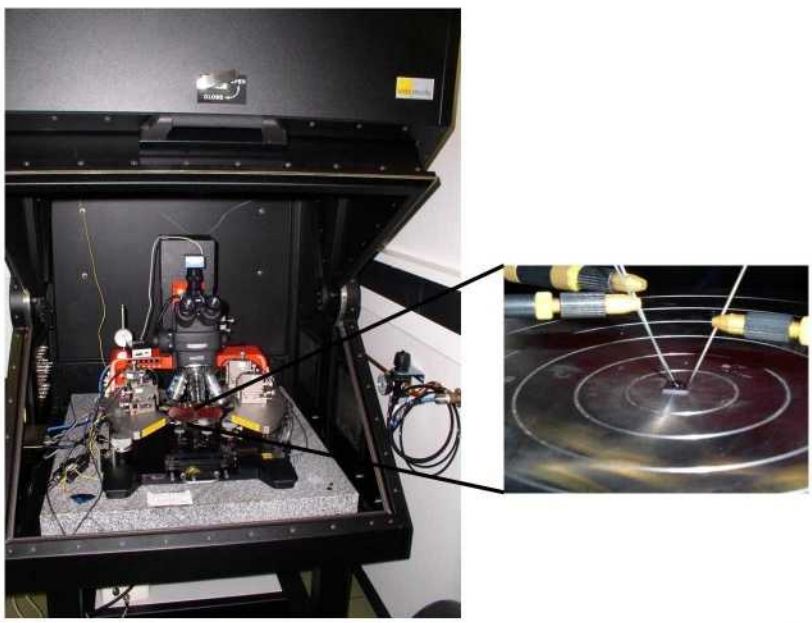

Figure 3.18: Transistors were characterized with a transistor probe station. Probe station and microscope were operated inside a Faraday cage. The chip was contacted with three tungsten pins (Inset).

Characterization with BioMol

After encapsulation (appendix B.1) the chips were characterized with the *transistor-transfer function* box (TTF-box). For this, the chip was mounted in a socket on the TTF-box and filled with electrolyte solution (extracellular patch solution, Table C.2 in the appendix), which was con-

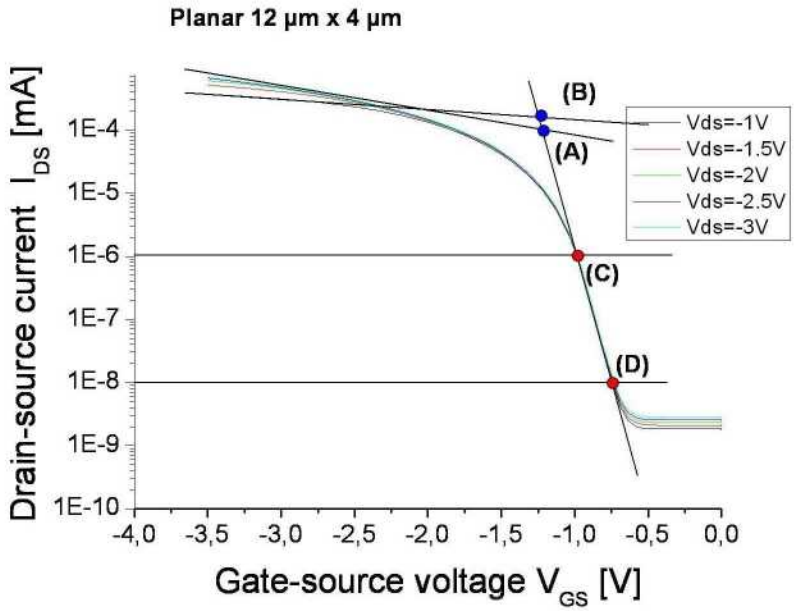

Figure 3.19: Transfer characteristics of a planar FET with gate width 12 μm and gate length 4 μm with logarithmic scaling of I_{DS}. The threshold voltage for drain-source voltages -1 V and -3 V was determined from the x-value of the points (A) and (B) (blue marks). The subthreshold slope was estimated from the slope fitted in the linear region between the data points (C) and (D) (red marks).

tacted by a Ag/AgCl electrode (Figure 3.20). The applied gate-source and drain-source voltages were controlled with the BioMol software (Lomparski 2007) (Figure 3.21). All 16 transistors on the chip were characterized and the transconductance was calculated. This process was repeated before each cell measurement and the transistors were set to a working point showing a high transconductance.

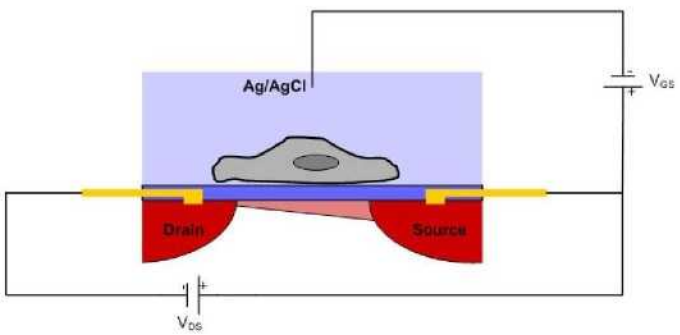

Figure 3.20: Open-gate p-FET in the enhancement mode. The electrolyte was grounded with a Ag/AgCl electrode. The picture was adapted from Meyburg [2005].

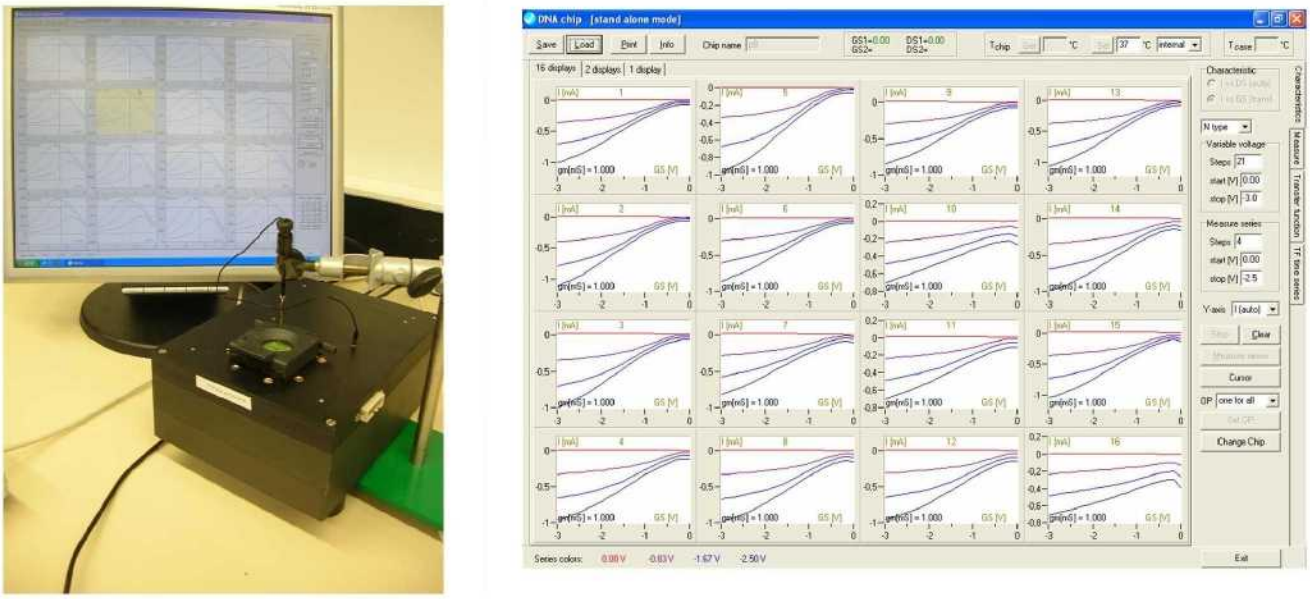

(a) (b)

Figure 3.21: The TTF-box (a) and the BioMol software with transistor transfer characteristics (b) for all 16 channels in parallel.

Noise measurements

Noise measurements were conducted with the headstage presented by Meyburg [2005] (Figure 3.22). It consists of a patch panel for chip control, two operational amplifiers and a zero-force socket to hold dual-inline chips (DIL). The pre-amplifier converts the drain-source current I_{DS} into a voltage, then the DC offset is compensated by a voltage V_{comp} and the main amplifier amplifies the signal again by the factor 10. Data aquisition of the output signal was completed with a DAQ-board (NI 6071E). Due to the socket, the chips were encapsulated on top of 28 pin dual-inline carriers and the contacts were bonded (appendix B.1). First, one transistor of the chips was characterized with the software SA3Cell (Meyburg [2005]) and set to its working point. A time measurement for 5 s with a sampling frequency of 20 kHz was performed and the *power spectral density* (PSD) was calculated using a *Fast Fourier Transform* (FFT) algorithm (Eick [2007]). To get a better estimate of the PSD, 100 of these spectra were averaged. Those measurements could either be conducted with a defined sinusoidal input signal (10 mVpp, 109 Hz) applied to the bath electrode to calculate the *signal to noise ration* (SNR) or without any input signal for the noise characteristics.

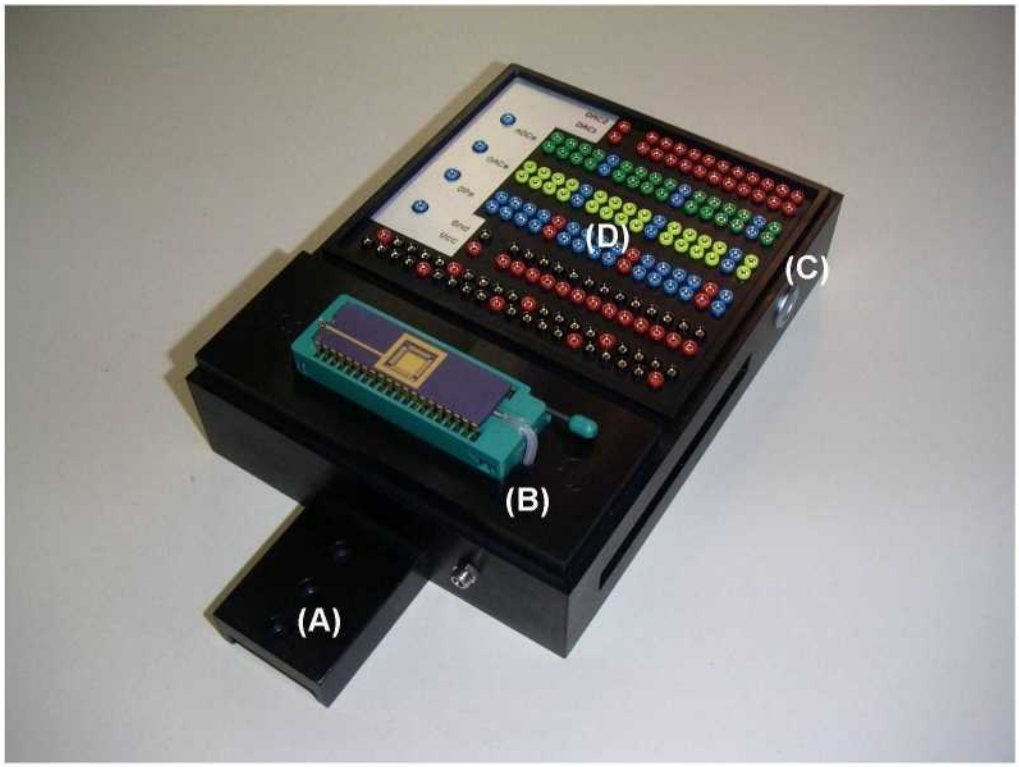

Figure 3.22: Headstage for noise measurements: mounting (A), zero-force socket (B), power supply (C) and patch panel (D).

3.2 Transfer function measurements

3.2.1 The Setup

To perform cell measurements, the TTF-box was mounted on a x-y-table underneath a microscope and an external power supply was attached (Figure 3.24). The included microprocessor (Tiger, BTI-ACI-4/4) was addressed by the BioMol software. With this setup three measurement modes were possible:

- Mode 1: Frequency-dependent transfer function measurements with AC signal V_{IN} sweep
- Mode 2: Time-dependent TF-measurement with AC signal V_{IN} constant
- Mode 3: Time-dependent transistor measurement in constant-voltage mode

In Mode 1, V_{OUT} was measured for various frequencies in the range of 1 Hz to 1 MHz with roughly equal distances at a logarithmic scale. The values were normalized and saved. Measurements without cells were dependent on the transistor conducting line capacitance (C_{CL}) and the resistance of electrolyte and reference electrode (R_{el}). A typical lowpass-behaviour was seen with a distinct cut-off frequency. When cells were cultured on the transistors, this behaviour was

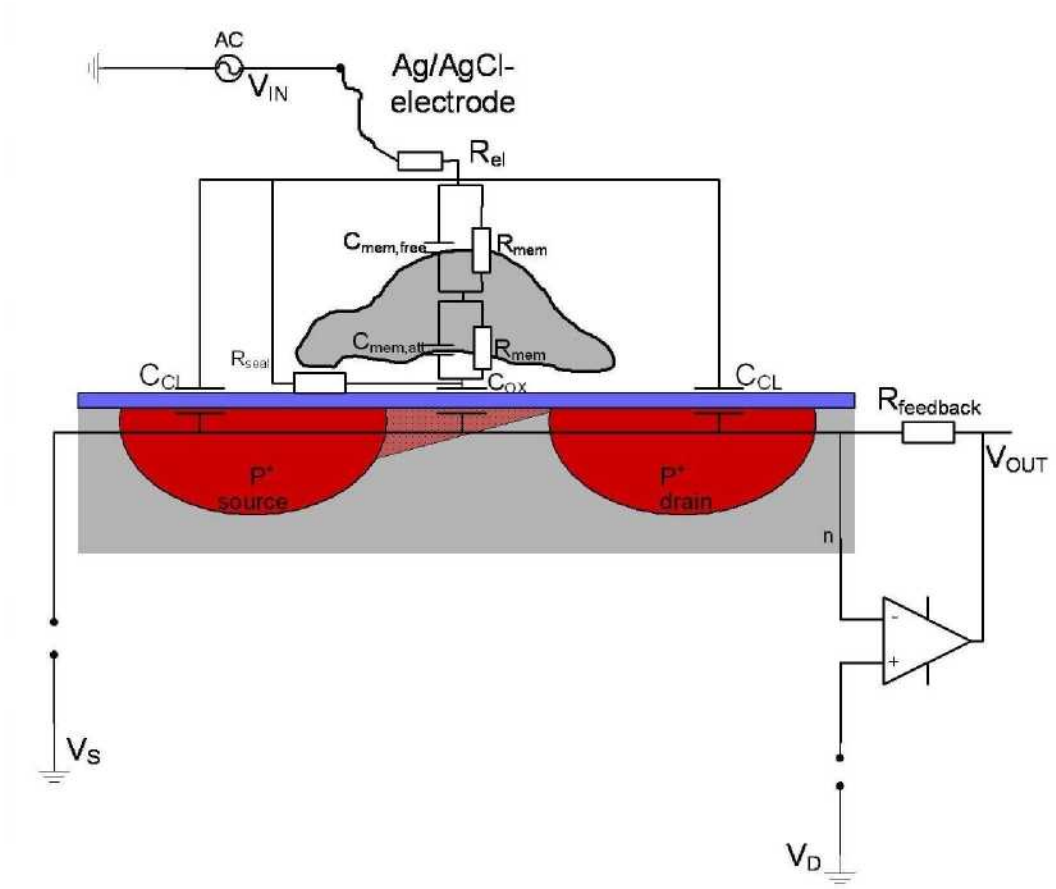

Figure 3.23: Schematic circuit of a transistor with a single cell on top. V_{in} and V_{out} denote applied and output voltage, V_D and V_S denote drain- and source-voltage, respectively. The cell is represented as the electrical components contributed to the circuit: membrane capacitance (C_{mem}) for free and attached membrane, membrane resistance (R_{mem}) and the sealing resistance in the cleft between cell and transistor (R_{seal}).

modified by additional electrical components due to cell adhesion (see Figure 3.23). With Mode 2, the transconductance was followed over time at a constant frequency with a sinusoidal AC voltage of varying frequency and phase. In Mode 3 the potentiometric change in the drain-source current was followed over time with a constant voltage. Using the Tiger microprocessor for data aquisition, the maximum sampling rate for the time-dependent modes was limited to 1 Hz. For higher sampling rates a data aquisition device (DAQ-device NI6071) was connected to the TTF-box, offering sampling rates up to 1.25 MS/s for one channel.

All cell measurements were done with encapsulated and precoated chips. Fibronectin (for fibroblasts) and poly(L)lysine (all other cellular systems) were used as coating to promote cell adhesion. Preparation of cells and other model systems is described in appendix C.

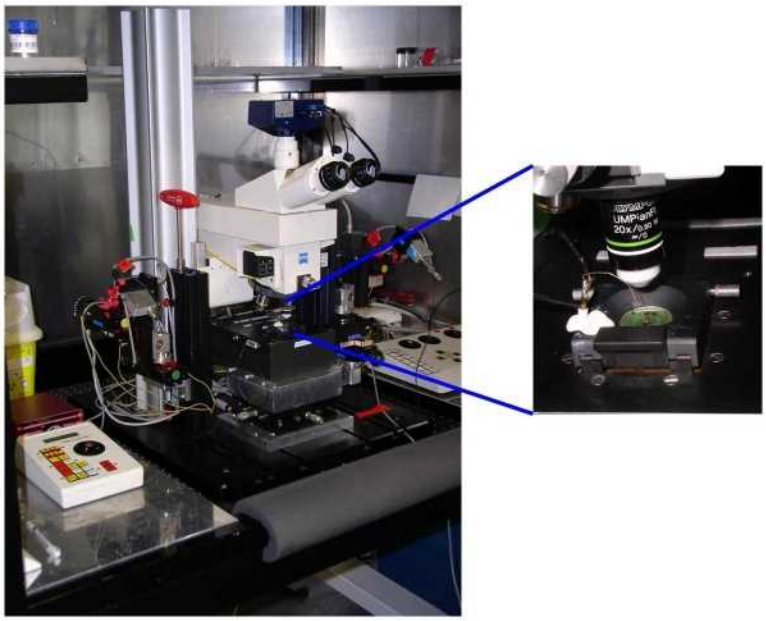

Figure 3.24: For optical control of the electrical measurements, the TTF-box was mounted on a x-y-table underneath a microscope equipped with an immersion objective.

3.2.2 Cell adhesion measurements

The cell adhesion measurements were done with human embryonic kidney cells (HEK293) of the EAG type (appendix C.1). This cell type expresses voltage gated potassium channels from the family *éther-a-gogo* (EAG) (Frings et al. [1998]). HEK cells are often used as a model system, e.g. for the examination of ion channel kinetics (Wrobel et al. [2005]). The cells were cultured for minimum two days on the chips before measurement. Before the measurement the cell medium was exchanged to extracellular patch solution (37°C). The chip was mounted to the TTF-box and temperature was set to 37°C. The transistors were set to their working point and an alternating current was applied to the bath electrode. The position of the cells on the transistor area was checked optically to distinguish gates with adherent cells from free gates (Figures 3.25 (a) and 3.27 (a)), and the transfer function was measured. Afterwards, the cells were removed from the chip mechanically with a Q-tip soaked with ethanol and the measurement was repeated without cells.

Trypsin activity

To induce cell detachment without mechanical force, trypsin was used. Trypsin is a serine endopeptidase, which cleaves poly(L)lysine, and therefore removes the basis for cell anchorage to the substrate (Waley and Watson [1953]) (see inset of Figure 3.26). This was observed by frequency- and time-dependent measurements. A transfer function measurement of Mode 1 was completed, then a time-dependent measurement was started at a constant frequency, where the biggest change to the transfer function was expected (typically about 200 kHz). After several minutes, 200 μl of trypsin were added and the detachment of the cells from the surface was monitored electrically and optically. Afterwards the frequency-dependent measurement (Mode 1) was repeated. Due to the trypsin activity, the protein layer was cleaved and subsequent detachment of the cells resulted in a change in cell morphology towards roundly shaped cells (Figure 3.25). While the cell-substrate cleft changed significantly, the cell membrane seemed to stay intact, simply changing the ratio of attached to free membrane (Figure 3.26).

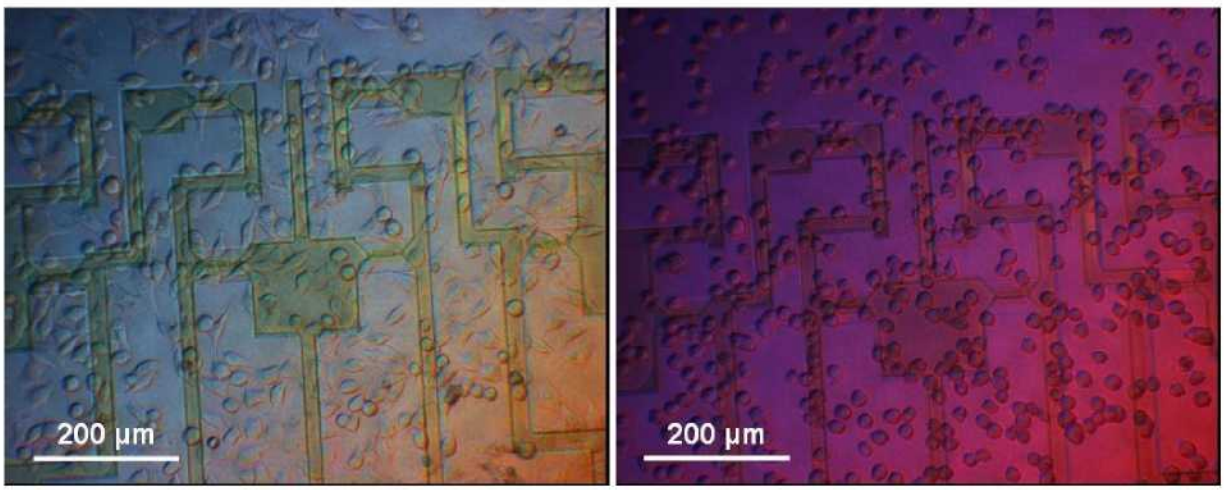

(a) (b)

Figure 3.25: Healthy looking cells on transistor surface (*days on chip* (DOC) 2) (a) and after trypsin treatment (b).

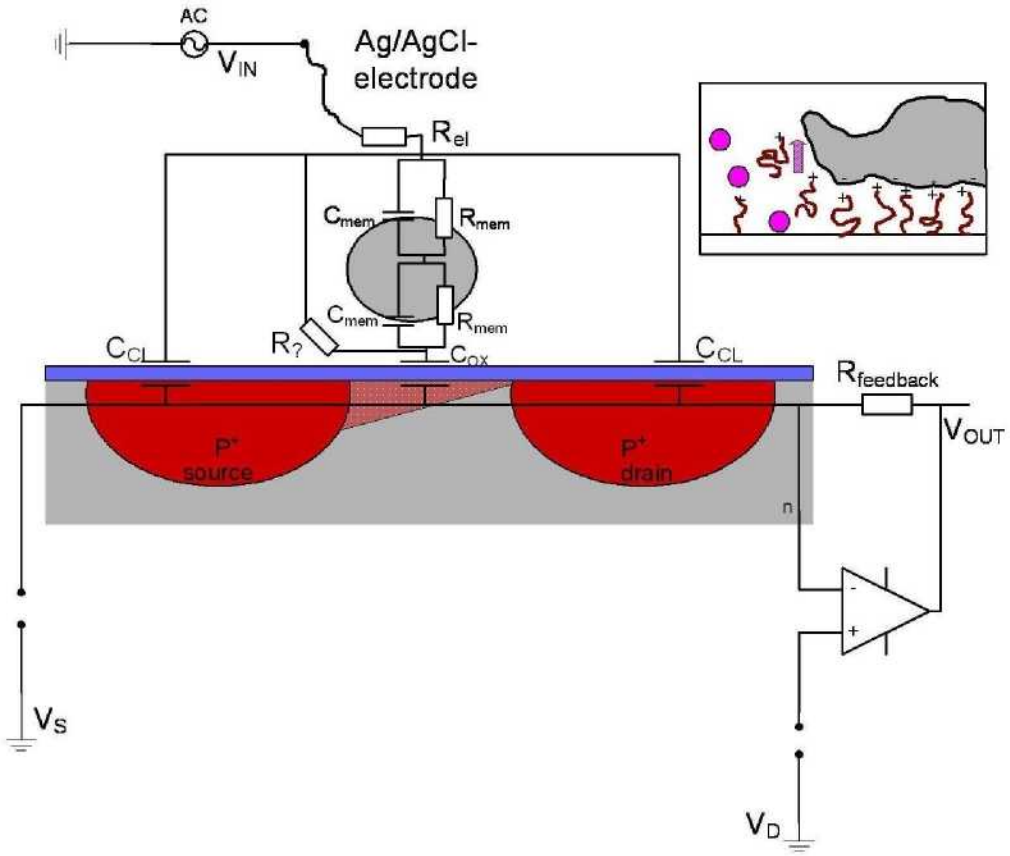

Figure 3.26: When trypsin cleaved the protein layer, the cells became roundly shaped and detached from the chip surface (inset). Therefore the values of the electrical components inside the circuit changed.

Amphotericin B activity

In a second experimental configuration, the ionophor Amphotericin B (AmB) was chosen because of its ability to affect the cell membrane. This antibiotic is known to bind to sterins in the cell membrane and to permeabilize it for K^+-ions. This was controlled optically (Figure 3.27) and electrically by continous frequency-dependent TF-measurements as well as TF-measurements in Mode 2. 200 μl of extracellular patch solution were exchanged with 200 μl of AmB (0.1 mg/ml). Massive changes in the cell membrane capacitance C_{mem} were expected, as well as an alteration of the sealing resistance R_{seal} (Figure 3.28).

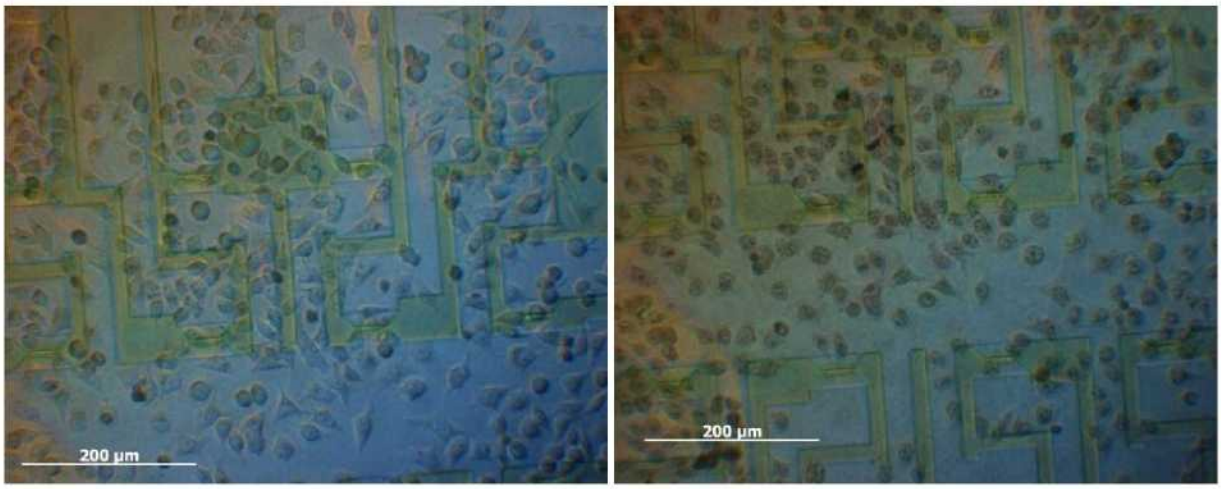

(a) (b)

Figure 3.27: Healthy looking HEK cells on transistor surface (DOC 2) (a) and after AmB treatment (b).

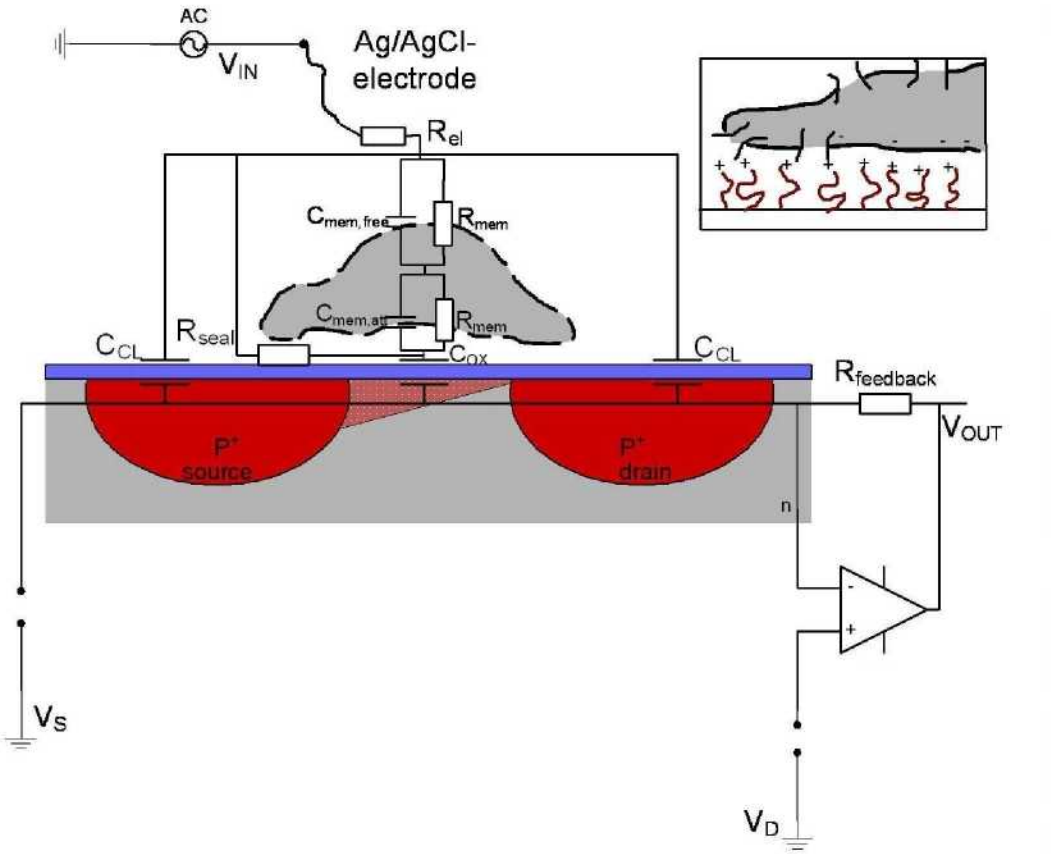

Figure 3.28: AmB was used to perforate the membrane (inset), leading to changes in the transfer function.

Apoptosis measurements

When cells undergo apoptosis or programmed cell death they permeabilize their membrane, one effect also observed after amphotericin treatment. Now, as a third configuration, we induced apoptosis with the anti-cancer agent irinotecan hydrochloride (CPT-11) (Conti et al. [1996]). Cells were cultured as described before and measured on the fourth day after plating them on the chips (Figure 3.29 (a)). The transistors were characterized and set to their working point. A transfer-function measurement in Mode 1 was conducted and a photograph was taken, both showing the gates with adherent and free of cells. Measurements of Mode 2 and 3 were started simultaneously, thus leading to time-dependent potentiometric measurements of the drain-source current and impedimetric measurements of the transconductance at a constant frequency of 200 kHz. After about 5 min, the cell medium was completely exchanged against a solution which contained CPT-11 and the apoptosis markers annexin-V and propidium iodide (Table C.4). The electrical measurement was continued while the fluorescence light source was switched off for

an incubation time of 60 to 110 min. During this period, apoptosis started and the annexin-V bound to the cell membrane due to flip-flop movements. It therefore served as a marker for early apoptosis (Figure 3.29 (b)). Once the membrane had become permeable, propidium iodide could diffuse into the cell and bind to the DNA, hence marking a late state of apoptosis (Figure 3.29 (c)). After the staining, photographs were taken to verify the state of the programmed cell death and the transfer-function measurement in Mode 1 was repeated. Those pictures served as optical control for the time-series measurements.

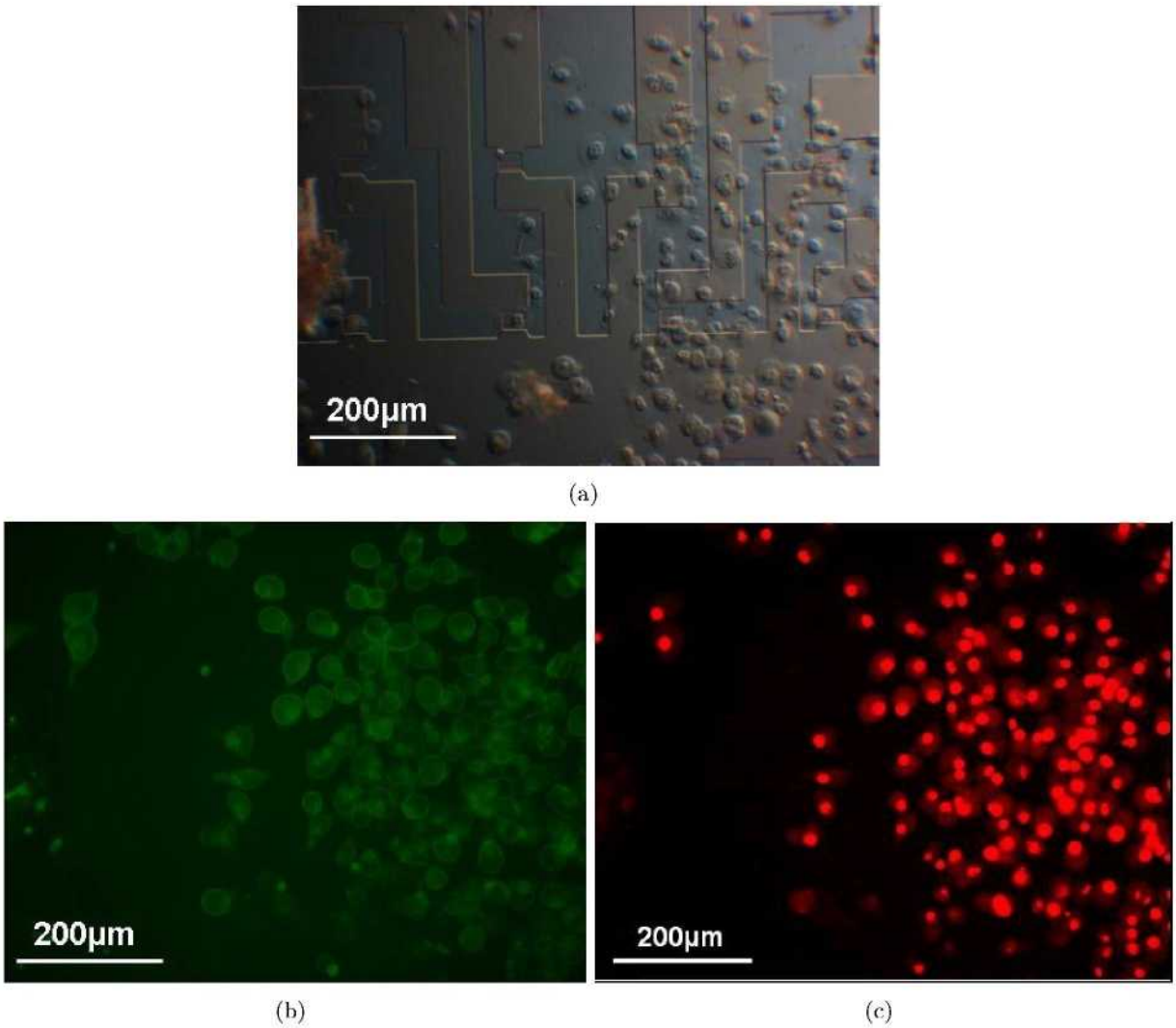

(a)

(b)

(c)

Figure 3.29: Healthy HEK cells (a), HEK cells stained with FITC labeled annexin-V during early apoptosis (b) and HEK cells stained with propidium iodide during late apoptosis (c).

3.2.3 Vesicles and erythrocyte ghosts as model systems

Although HEK cells are a widely used model system in our cell research group, there is a demand for even simpler cellular model systems. In this subsection, two model systems of smaller size and less complexity were used.

Vesicles

Vesicles were chosen as biomimetic system, as their lipid composition can be controlled by the preparation. They lack any kind of adhesion-mediating proteins or spacing molecules in their membrane and are therefore assumed to stay close to the surface (Fromherz et al. [1999]). The cleft height was reported to be in the range of 10 nm, with the vesicle membrane following the surface smoothly.

Vesicles were prepared by the electroswelling method as described in appendix C.2. Negatively charged lipids were incorporated to ensure an electrostatic interaction with the positive PLL surface coating. Furthermore, the vesicles were labeled with a fluorescent die. After preparation they were stored in glucose solution and measured within the next hours. As the vesicles tend to split over time, the biggest vesicles could be found right after preparation (Figure 3.30). Osmolarities of the intra- and extravesicular solution were set to 300 mOsm and 310 mOsm, respectively. Hence, the membrane was not tense, but elastic, allowing the vesicles to adapt to the surface smoothly. Firstly, the chips were characterized with glucose solution as electrolyte and a frequency-dependent TF-measurement was taken as reference. Then the vesicles were carefully added with a BSA coated pipette to avoid rupture of the sensitive membranes. Due to the fluorescent die, the vesicles could be checked optically while sinking to the chip surface. After about 30 minutes the vesicles had settled. The chip surface was then photographed and a second frequency-dependent TF-measurement was performed. The measurement could easily be repeated by applying a slight shear force to the solution with a pipette, thus reorganizing the vesicles on the surface. Nevertheless, the number of repetitions was limited, as the vesicles burst eventually.

Erythrocyte-ghosts

Furthermore, erythrocyte ghosts were chosen as cellular model system of low complexity, but also of small size. Usually, the cell remnants called ghosts can either be isolated from bacteria (bacteria ghosts) (Paukner et al. [2003]) or from red blood cells (erythrocyte ghosts). Here, red blood cells

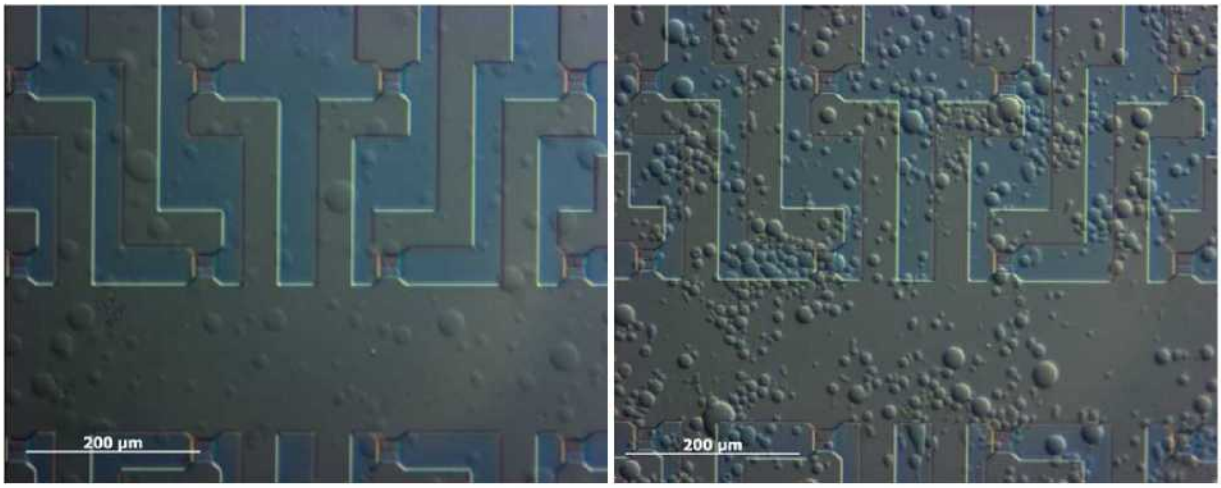

(a) (b)

Figure 3.30: Vesicles on chip surface 1 hour after preparation (A) and 6 hours after preparation (B).

were used for preparation, which is described in detail in appendix C.3. After controlled lysis of the red blood cells and subsequent resealing, membrane shells of approximately $7\,\mu m$ diameter remained. Those ghost membranes did not contain proteins, which might have acted as spacers. This usually results in a very close distance to the substrate of $12 \pm 1\,nm$ (Hutzler and Fromherz [2004]) and good sealing properties to a surface were expected. The ghosts were plated on the transistor chips and stored at 4°C while sinking to the surface. After 30 to 45 minutes, transfer function measurements were conducted at room temperature. The buffer ISP7.4 (appendix, Table C.6) was used as electrolyte. As the ghosts were immediately detached by shear forces when the immersion objective was dipped into the electrolyte, optical control during the measurement was very difficult.

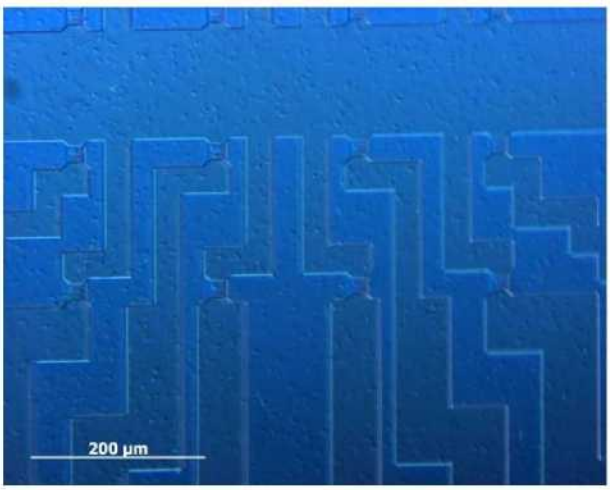

Figure 3.31: Ghosts prepared from red blood cells were almost transparent and of a diameter of $7\,\mu m$.

3.2.4 Cell migration measurements

Cell migration is strongly linked to the cells' ability to adhere to a surface. Therefore time-dependent TF-measurements were also used to observe cell migration. For those experiments, fibroblasts were chosen as cellular system, as they are very motile and a prefered model system in migration research. Fibroblasts are mainly present in the connective tissue. They play an essential role for synthesis of the extracellular matrix, e.g. by producing collagen. This is especially important for healing processes after tissue rupture. The fibroblasts were taken from the umbilical cord of the rat and plated onto the fibronectin coated chips in numbers of 2 000 to 15 000 cells per chip (Figure 3.32). They were cultured for 1 to 2 days at 37°C in an incubator. To stimulate cell migration, 50 nM epidermal growth factor (EGF) was added 1 hour before the measurement. Fibroblast culture medium (appendix C.7) was used as electrolyte. While accomplishing the transfer function measurements, a time series of photographs was taken with one photograph per minute to correlate cell motion and electrical signal.

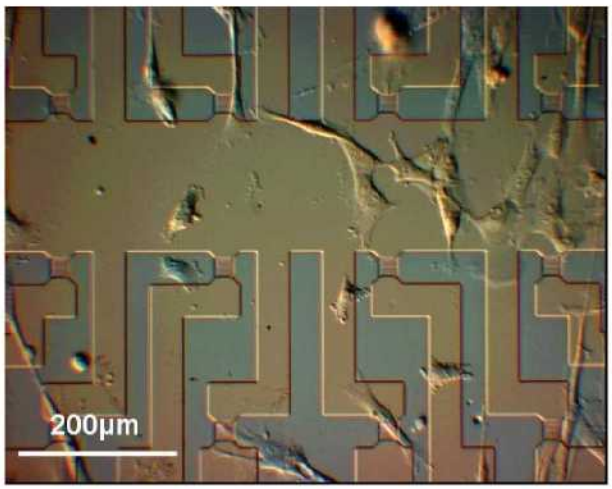

Figure 3.32: Fibroblasts were cultured on fibronectin coated transistor chips.

Chapter 4

Results

4.1 Characterization of the planar FET

In this section the results of the chip characterization during and after processing are shown. This covers the achieved planarization as well as the transistor characteristics, including threshold voltages and subthreshold slopes. Finally a noise comparison of open-gate p-FETs and buried-channel p-FETs is given.

4.1.1 Planarization

The planarization process was examined on wafer 2 with a surface profilometer and an *atomic force microscope* (AFM). Profiles were measured before the LOCOS etch, after the LOCOS etch and after the nitride layer had been removed. To optimize the etching time of the LOCOS oxide, this process step was tested on wafer 5 before etching the other wafers. The step height from the conducting lines (see Figure 4.1(B)) to the gate area d_{CG} (see Figure 4.1(A)) as well as the height of the birds beaks d_{bb} (Figure 4.1(E)) were of special interest. In the first profile, the step height d_{CG} was 12.4 nm, determining the oxide thickness to be etched to about 100 nm (Figure 4.1). Birds beaks had an approximate height of 20 nm. After etching, the profile showed a height difference d_{CG} of 77.4 nm (Figure 4.2). From this value, the thickness of the nitride layer was determined to approximately 47 nm ($77.4\,nm - 30\,nm$ oxide).

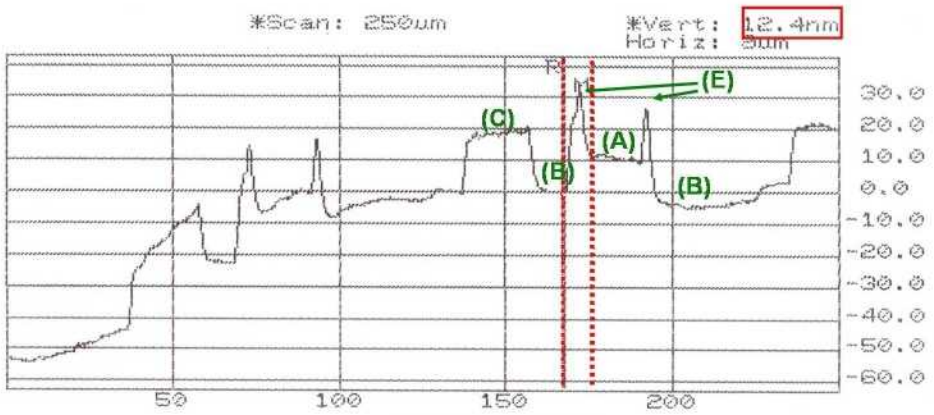

Figure 4.1: The step height d_{CG} from the conducting lines (B) to the gate area (A) was determined with a surface profilometer before etching. The interspace between the transistors is marked with (C), birds beaks are denoted with (E).

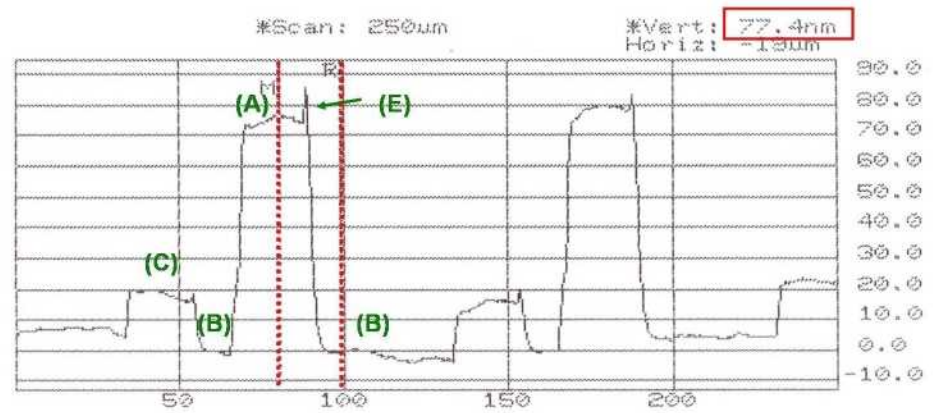

Figure 4.2: Step heights on wafer 2 were measured after the LOCOS etch. d_{CG} was 77.4 nm, consisting of 30 nm oxide and approximately 47 nm nitride.

The nitride layer was removed and the topography was mapped again. For test wafer 5, a step height $d_{CG,final}$ of 25.1 nm was measured with birds beaks of the approximate height of 10 to 15 nm (Figure 4.3). All other wafers were etched with optimized etching time and d_{CG} was thus reduced to even lower values. Wafer 4 thereby showed the lowest step height $d_{CG,final}$ of -2 nm and birds beaks of 30 nm (Figure 4.4). This final profile data was aquired for all wafers, resulting in an averaged $d_{CG,final}$ of 4 nm (wafer 5 excluded). An even better planarity was achieved for

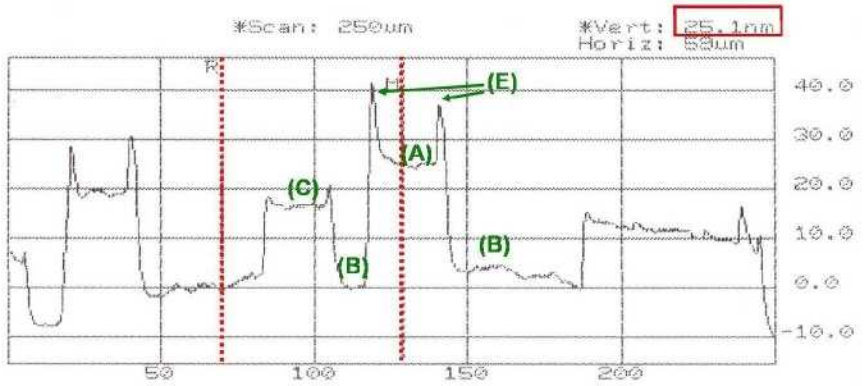

Figure 4.3: Wafer 5 was measured after nitride removal. d_{CG} was approximately 25 nm and the birds beaks were 10 to 15 nm high.

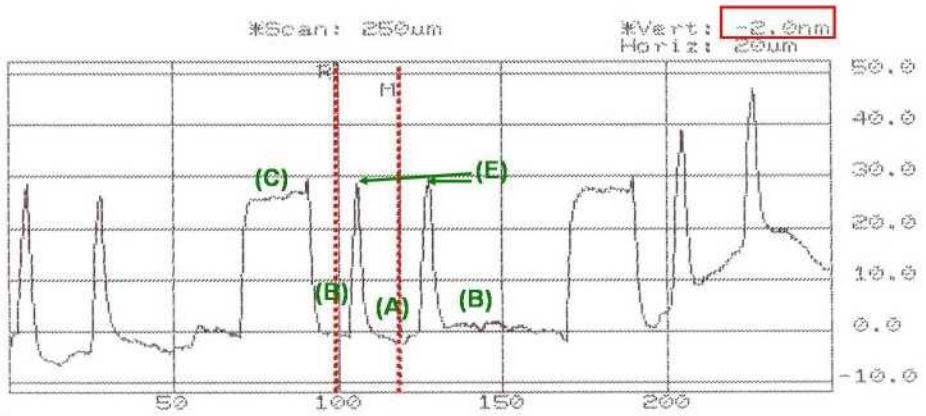

Figure 4.4: Wafer 4 after planarization with optimized etching time. d_{CG} was -2 nm and the birds beaks had a height of 30 nm.

wafer 2, which was observed with the AFM (Picture 4.5). $d_{CG,final}$ was less than 1 nm and birds beaks were approximately 24 nm high. Therefore the topography was significantly reduced by this planarization procedure compared to the Juelich FET. The maximum step heights of 30 nm due to the birds beaks were taken as planar.

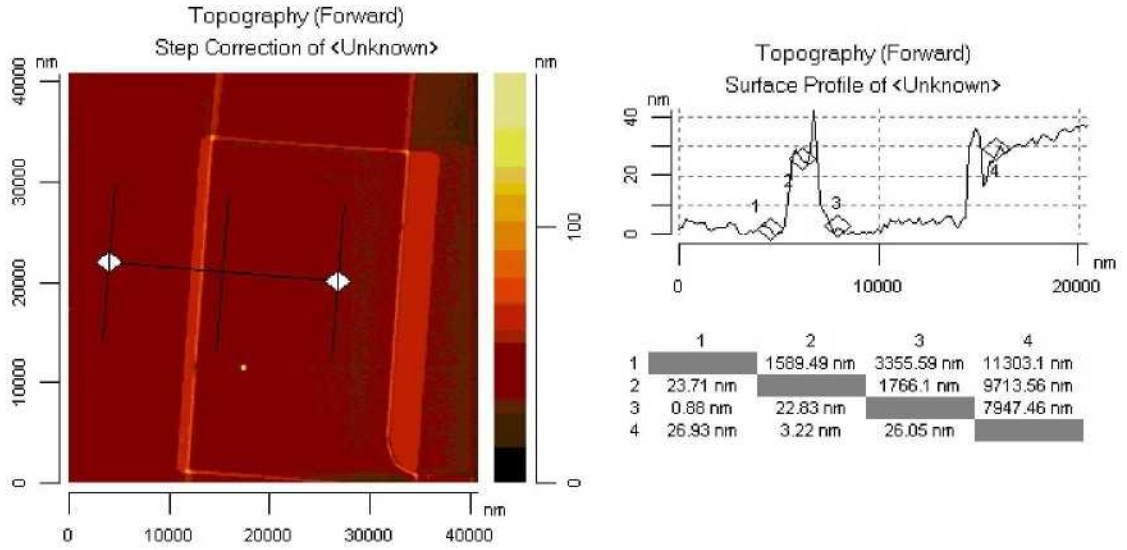

Figure 4.5: Wafer 2 had a step height d_{CG} of less than 1 nm after the planarization. Birds beaks were approximately 25 nm high. The table lists all vertical step heights (left of grey mark) and the lateral distances (right of grey mark).

4.1.2 Characterization with the probe station - Threshold voltage and subthreshold slope

Threshold voltage and subthreshold slope of the planar open-gate FETs were determined with the wafer probe station. The drain-source voltage was plotted in logarithmic scale versus the logarithmically measured gate-source voltage (Figure 4.6).

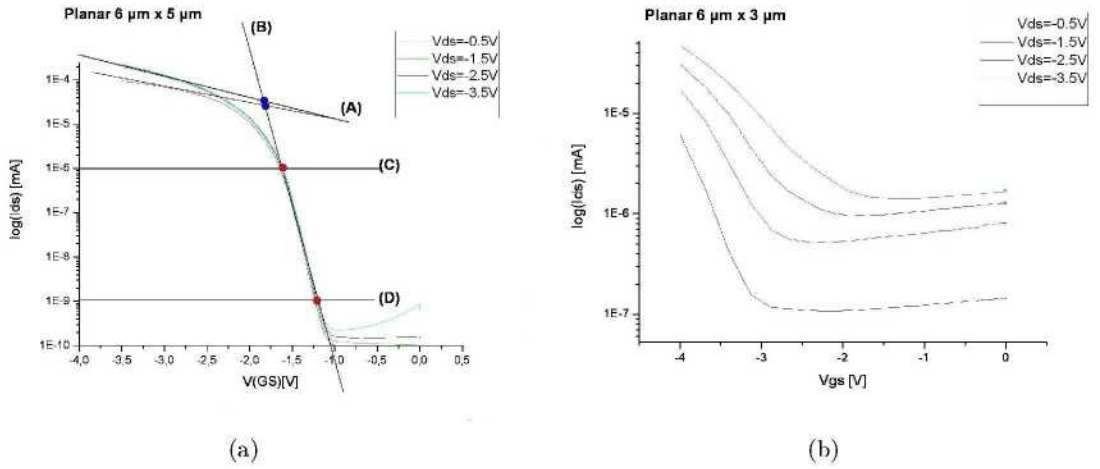

(a) (b)

Figure 4.6: The logarithmic plot $I_{DS}(V_{GS})$ was fitted in the linear and the saturation region ((A), (B)). The threshold was determined from the x-values of the intersection point (blue dots). The subthreshold slope was estimated from the slope of the linear region ((C), (D), between red dots) (a). This method could not be applied for the chip with gate dimension 6 μmx3 μm, because neither a single linear fit in the linear region was possible, nor a linear fit in the saturation region (b).

Gate geometry [μm^2]	Threshold voltage [V]	Subthreshold slope [$\frac{mV}{dec}$]
6x3	-	-
12x3	-2.3	180
25x3	-2.3	200
6x4	-1.9	110
12x4	-1.2	130
25x4	-1.1	100
6x5	-1.8	100
12x5	-1.4	110
25x5	-1.3	100

Table 4.1: List of threshold voltages and subthreshold slopes of the FETs out of the second process.

The linear and the saturation region of the transfer characteristics were fitted linearly and the threshold value was determined from the x-value of the point of intersection of the linear fits (Figure 4.6 (A) and (B), blue dots). In case the fit varied for different drain-source voltages, the values of the points of intersection were averaged. The subthreshold slope was estimated from the linear region (Figure 4.6 (C) and (D), red dots). These measurements were only conducted for the FETs of the second run, as the transistors from the first process did not show a distinct threshold. For transistors with the gate length 4 μm threshold voltages lay in the range of -1.9 V to -1.1 V, for transistors with the gate length 5 μm threshold voltages of -1.8 V to -1.3 were obtained (Table 4.1). For transistors of the same gate length the threshold voltage decreased with increasing gate width. The threshold voltage was plotted in dependency of the ratio of gate width to gate length and fitted linearly (Figure 4.7).

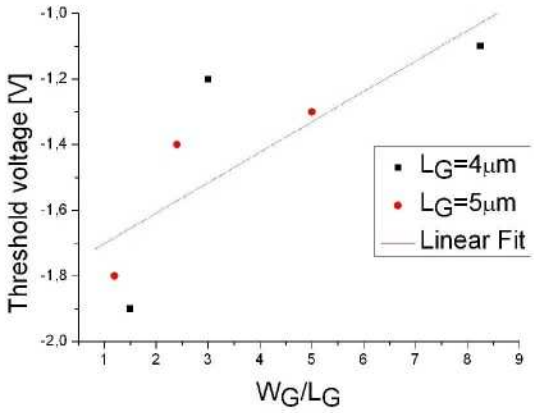

Figure 4.7: The threshold voltage was linearly dependent on the ratio of gate width and gate length W_G/L_G for gate lengths of 4 and 5 μm.

As the FETs with a gate length of 3 μm showed an unusual high threshold voltage compared to the transistors with bigger gate length, they were omitted in this plot. For gate dimensions 6 μm x 3 μm the values could not be obtained within the measurement range (Figure 4.6 (b)). The subthreshold slope for the transistors with gate length $4\mu m$ and $5\mu m$ lay between 100 and 130 mV/dec, revealing respond of the drain-source current for an applied gate-source voltage (Figure 4.1). The transistors with $3\mu m$ gate length had a subthreshold slope in the range of 180 to 200 mV/dec. Therefore they cannot react as quickly as the transistors with a bigger gate length to the applied gate-source voltage.

4.1.3 Characterization with BioMol

Characteristics of planar open-gate FETs

The encapsulated chips of both processes were characterized with the BioMol software. For this purpose, the gate-source voltage was swept from 0 to -3 V, the drain-source voltage was varied from 0 to -3 V in steps of -1 V and the drain-source current was measured (Figure 4.8 (a) and Figure 4.9 (a)). While the transistors of the first process did not close completely for negative voltages, the transistors of the second run had distinct threshold voltages. Nevertheless, both transistors behaved in a typical manner for field-effect transistors. For FETs of the first process the transfer characteristics were occasionally found to decrease with a higher slope for negative voltages in the range of $V_{GS} = -2.5V$ as it is typical for short-channel transistors (Figure 4.8 (a)). The maximum current of all transistors was in the mA range, though higher for the FETs of the first process.

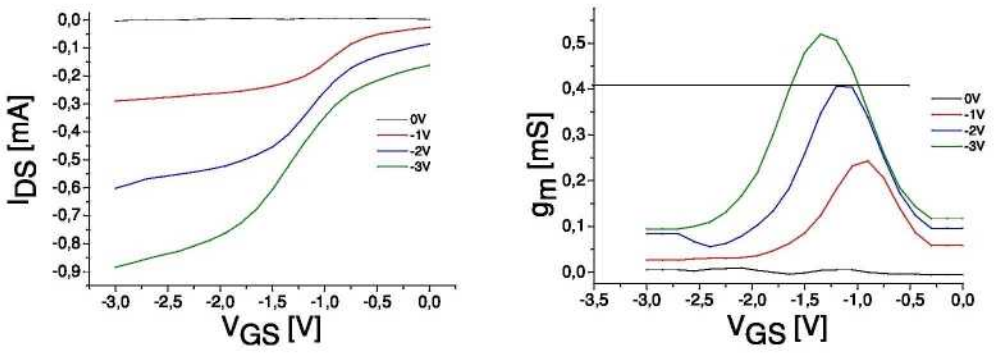

(a) (b)

Figure 4.8: Transfer characteristics (a) and transconductance (b) of a transistor from the first process with gate dimensions 25 μm x 3 μm. For comparison, the maximum transconductances at $V_{DS} = -2\,V$ (vertical line) were chosen.

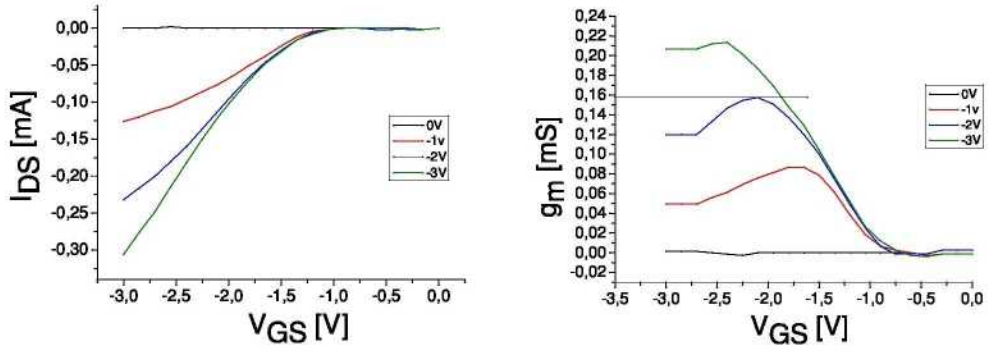

(a) (b)

Figure 4.9: Transfer characteristics (a) and transconductance (b) of a transistor from the second process with gate dimensions 12 μm x 4 μm. For comparison, the maximum transconductances at $V_{DS} = -2\,V$ (vertical line) were chosen.

Transconductance

The difference in the reached maximum current was also reflected by the transconductance, which was calculated by derivation of $I_{DS}(V_{GS})$. It increased with the applied drain-source voltage (Figure 4.8 (b) and Figure 4.9 (b)) and was also strongly dependent on the gate geometry as g_m grows proportional to the ratio W_G/L_G. All transistor transconductances were compared regarding the gate geometries at a drain-source voltage of -2 V (Table 4.2), as this is the drain-source voltage typically used in the cell adhesion measurements. Thereby the transistors of the first process showed almost three times higher transconductances as the transistors of the second process. As expected, the transconductance increased linearly with the ratio of gate width and gate length W_G/L_G (Figure 4.10).

(A) g_m [mS] ($atV_{DS} = -2V$)	$W_G = 6\mu m$	$W_G = 12\mu m$	$W_G = 25\mu m$
$L_G = 3\mu m$	0.29	0.34	0.41
(B) g_m [mS] ($atV_{DS} = -2V$)	**$W_G = 6\mu m$**	**$W_G = 12\mu m$**	**$W_G = 25\mu m$**
$L_G = 3\mu m$	0.14	0.11	0.15
$L_G = 4\mu m$	0.11	0.14	0.19
$L_G = 5\mu m$	0.09	0.12	0.15

Table 4.2: Transconductances of transistors fabricated in the first (A) and second (B) process at a drain-source voltage of -2 V.

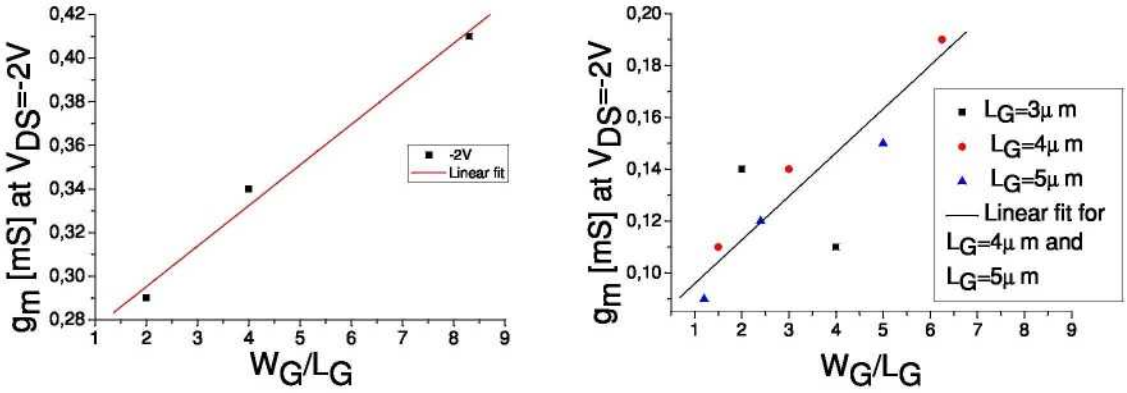

(a) (b)

Figure 4.10: Comparison of transconductances in the first process (a) and the second process (b).

Buried-channel transistor characteristics

The encapsulated *buried-channel transistors* (bc-FET) were characterized with the BioMol software. While reasonable transfer characteristics were observed for buried-channels with the implantation energies of 5 kev and 10 keV, the transistors with a higher implantation energy were not functionable. Two aspects of the characterization were of major interest. Firstly, the threshold shift to positive values (Figure 4.11) and secondly, the transconductance in comparison to the open-gate FETs at $V_{DS} = -2\,V$ (Figure 4.12). As the buried channel FETs with a gate length of $5\,\mu m$ showed the most reproducible transfer characteristics, they were chosen for all further evaluations. The threshold shift was determined from comparison of the threshold of open-gate and bc-FETs with the same gate geometries (gate length $5\,\mu m$, gate width 25, 12, and $6\,\mu m$) (Table 4.3). All buried-channel transistors had positive threshold voltages. The measured absolute shift was found between 2.1 and 2.4 V. At $V_{GS} = 0\,V$ the bc-FETs were operated in the linear region (Figure 4.11 (b) and (c)).

threshold voltage [V]	$6\mu m \times 5\mu m$	$12\mu m \times 5\mu m$	$25\mu m \times 5\mu m$
open-gate p-FET	-0.6	-0.75	-0.75
5 keV	1.8	1.35	1.35
threshold shift	2.4	2.1	2.1

Table 4.3: The threshold shift was evaluated from the comparison of open-gate FETs and buried channel FETs of the same gate geometry.

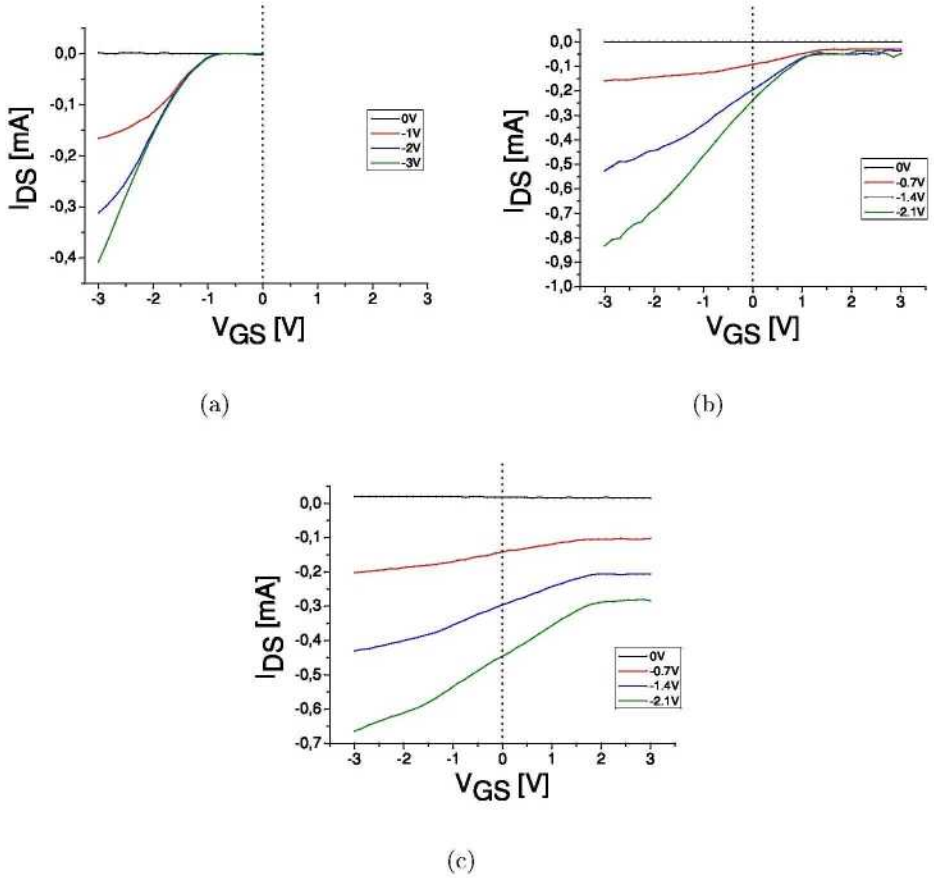

Figure 4.11: Transfer characteristics of an open-gate FET (A) and bc-FETs with implantation energies of 5 keV (B) and 10 keV (C), respectively.

The transconductance was calculated by derivation of $I_{DS}(V_{GS})$. For bc-FETs the transconductances were found to be in the same range as for the open-gate FETs. However, the bc-FETs with an implantation energy of 5 keV had a higher transconductance than those with an implantation energy of 10 keV. The transconductance at a gate-source voltage of 0 V was of special interest with respect to future measurements of voltage sensitive biosystems. For $V_{GS} = 0\,V$ the transconductances of the bc-FETs with 5 keV were almost identical to the values calculated for the open-gate FETs. For some of the transconductance plots two maxima were observed with one maximum for a negative and one for a positive gate-source voltage.

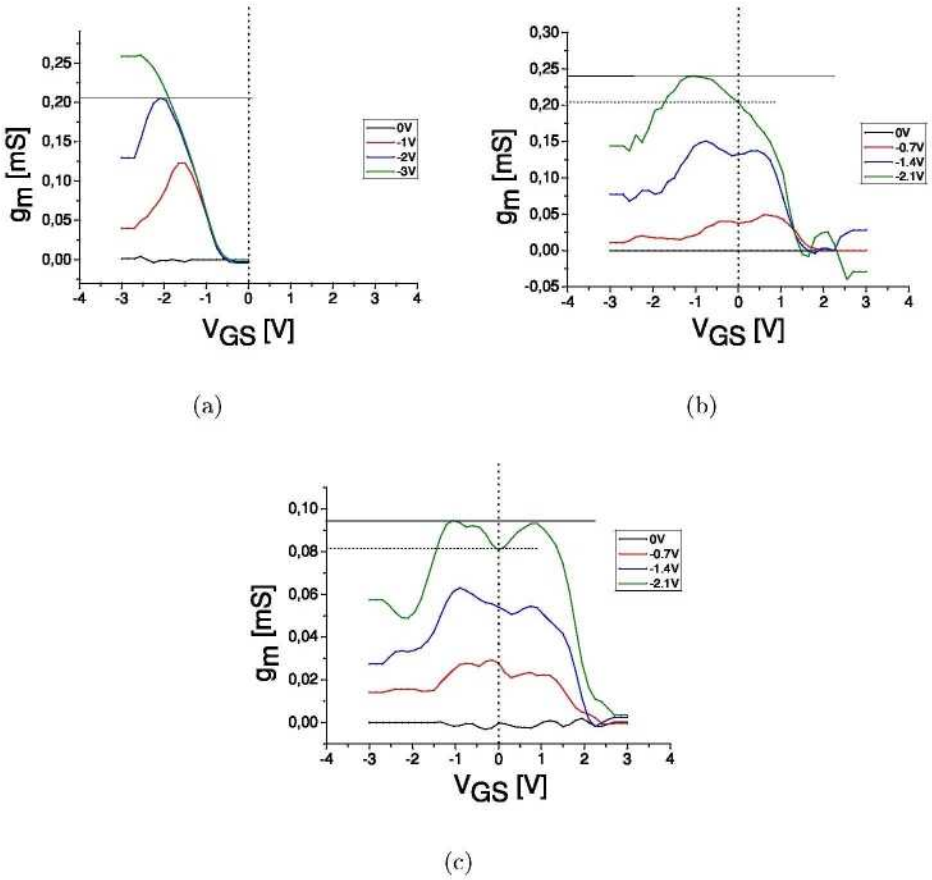

Figure 4.12: The transconductance maxima were compared for open-gate and bc-FETs. Furthermore, the transconductance of the bc-FETs was estimated for a gate-source voltage of 0 V.

transconductance [mS]	$6\mu m$ x $5\mu m$	$12\mu m$ x $5\mu m$	$25\mu m$ x $5\mu m$
open-gate p-FET	0.17	0.21	0.24
5 keV	0.23	0.24	0.3
at $V_{GS} = 0\,V$	0.19	0.2	0.26
10 keV	0.14	0.09	0.16
at $V_{GS} = 0\,V$	0.10	0.08	0.15

Table 4.4: Transconductances were compared for open-gate FETs and bc-FETs of gate length $5\,\mu m$ and all three gate widths.

Noise

To complete the transistor characterization, the noise properties of open-gate and bc-FETs were examined in comparison. For this, the gate geometry $12\,\mu m \times 5\,\mu m$ was chosen exemplary for all geometries and the spectral noise density was aquired for FETs without buried-channel and with 5 keV and 10 keV implantations, respectively (Figure 4.13). The value at 1 Hz of the spectral noise density was in the range of $10^{-9}\,V^2Hz^{-1}$ for the open-gate FET and the bc-FET with 5 keV. The noise decreased until a spectral noise density of $10^{-13}\,V^2Hz^{-1}$ was reached for 10 kHz. The initial spectral noise density of the 10 keV bc-FET was approximately $10^{-8}\,V^2Hz^{-1}$ and decreased to $10^{-12}\,V^2Hz^{-1}$ for 10 kHz. While no significant difference was found for open-gate FET and bc-FET with 5 keV, the noise of the 10 keV bc-FET was one order of magnitude higher than the noise of the open-gate FET.

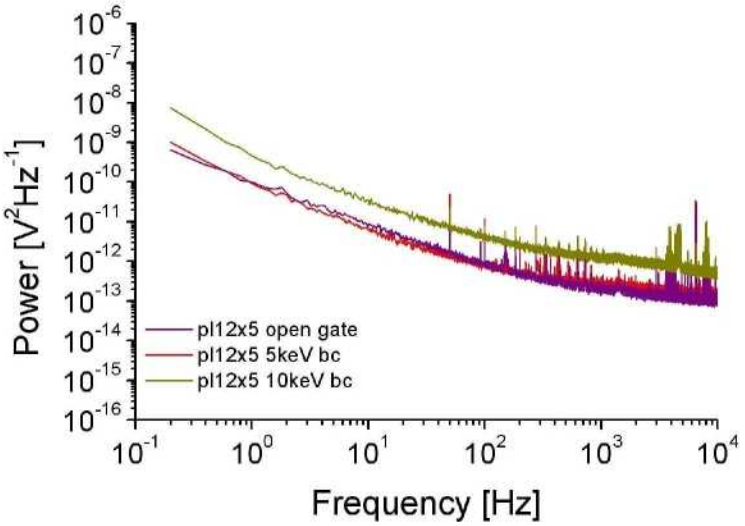

Figure 4.13: Spectral noise density of open-gate and bc-FETs (5 keV,10 keV) for $12\mu m\,x\,5\,\mu m$ gates.

The comparison of different gate geometries (Figure 4.15) proofed the exemplary measurement for the $12\,\mu m \times 5\,\mu m$ FETs to be representative for other gate widths. Furthermore, the spectral noise density did not vary significantly for bigger gate widths compared to the smaller ones. The high frequency noise in all plots was caused by the data aquisition card, but was of no importance for this comparison.

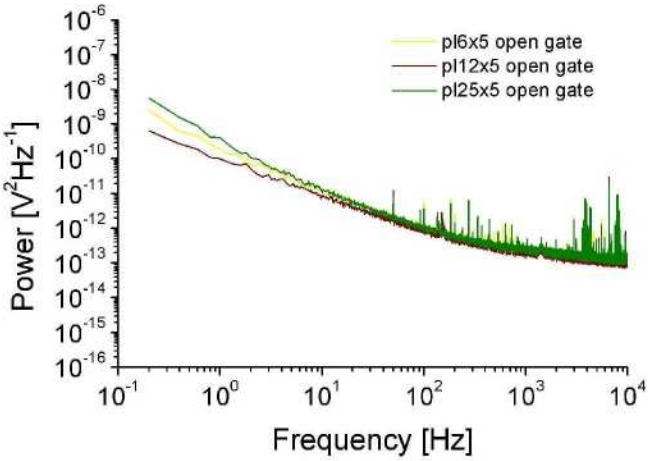

Figure 4.14: Comparison of the spectral noise density for open gate FETs with gate length $5\,\mu m$ and gate widths of $6\,\mu m$, $12\,\mu m$, and $25\,\mu m$.

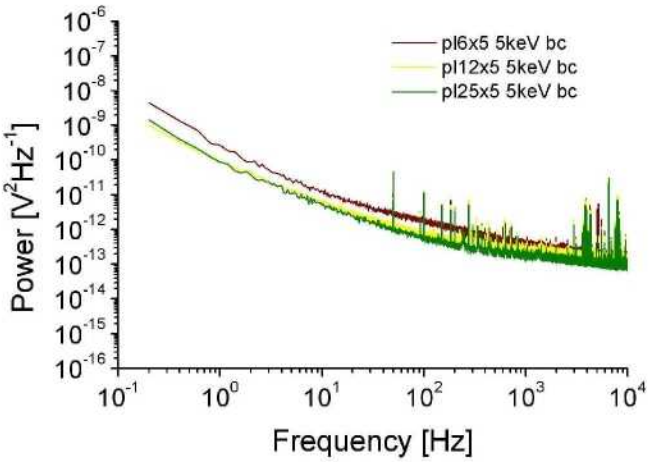

Figure 4.15: Comparison of the spectral noise density for 5keV bc-FETs with gate length $5\,\mu m$ and gate widths of $6\,\mu m$, $12\,\mu m$, and $25\,\mu m$.

4.2 Transfer-function measurements with field-effect transistors

In this section the transfer-function measurements of cellular systems with field-effect transistors will be presented. Firstly, experiments on cell adhesion are shown and the typical transfer-function shapes are introduced. Secondly, cell adhesion and detachment are examined over time after the treatment with varying reagents. In this context, data of cells undergoing apoptosis will be given. Furthermore, measurements with vesicles and erythrocyte-ghosts as cellular model systems will be presented. The cell adhesion measurements will be concluded with a subsection on the analytical approach of modelling the cell-transistor equivalent circuit. In the last subsection, transfer-function measurements of migrating cells will be presented.

4.2.1 Cell adhesion measurements

The transfer-functions of all 16 transistors on a chip were aquired simultaneously with a frequency-dependent measurement in Mode 1 (see subsection 3.2.1). The measurement was conducted in extracellular patch solution (Appendix Table C.2), which had a resistivity of 64.3 Ωcm. In the first exemplary cell adhesion experiment provided here, five of the transfer-functions differed significantly from reference gate 14 without cell (Figure 4.16). Those gates varied in cut-off frequency and appeared in multiple shapes.

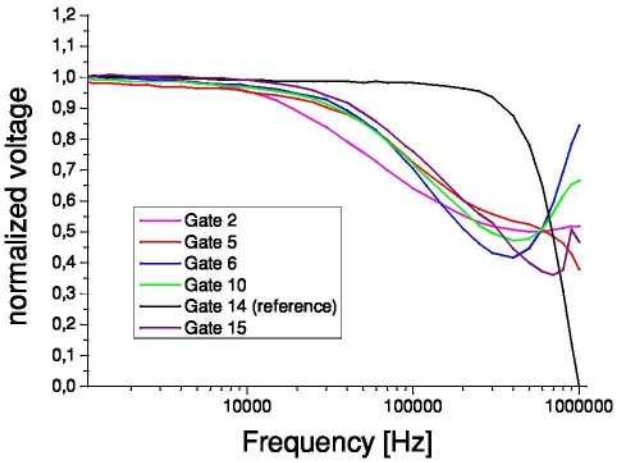

Figure 4.16: Frequency-dependent TF-measurement of a transistor chip with cells cultered on top. The different gates showed a variation of different forms of the transfer-function compared to reference gate 14, which was cell-free.

In this measurement, the reference gate had a transfer-function shape as expected and the amplitude dropped at a distinct cut-off frequency. Nevertheless, a different behaviour was observed for the same gate during another measurement (Figure 4.17). There the transfer-function increased in amplitude showing a turning point at about 500 kHz before descending. This variation in shape, although the gate was not cell-covered in either case, indicated that parameters within the cleaning and coating procedure, e.g. the protein layer thickness or general wear and tear of the chip, had an influence on the ground state of the transistor even without cell coverage. A third shape, which was frequently observed for cell-free gates (Figure 4.18), showed a sharp bend upwards with the amplitude increasing towards infinity for high frequencies (200 to 300 kHz).

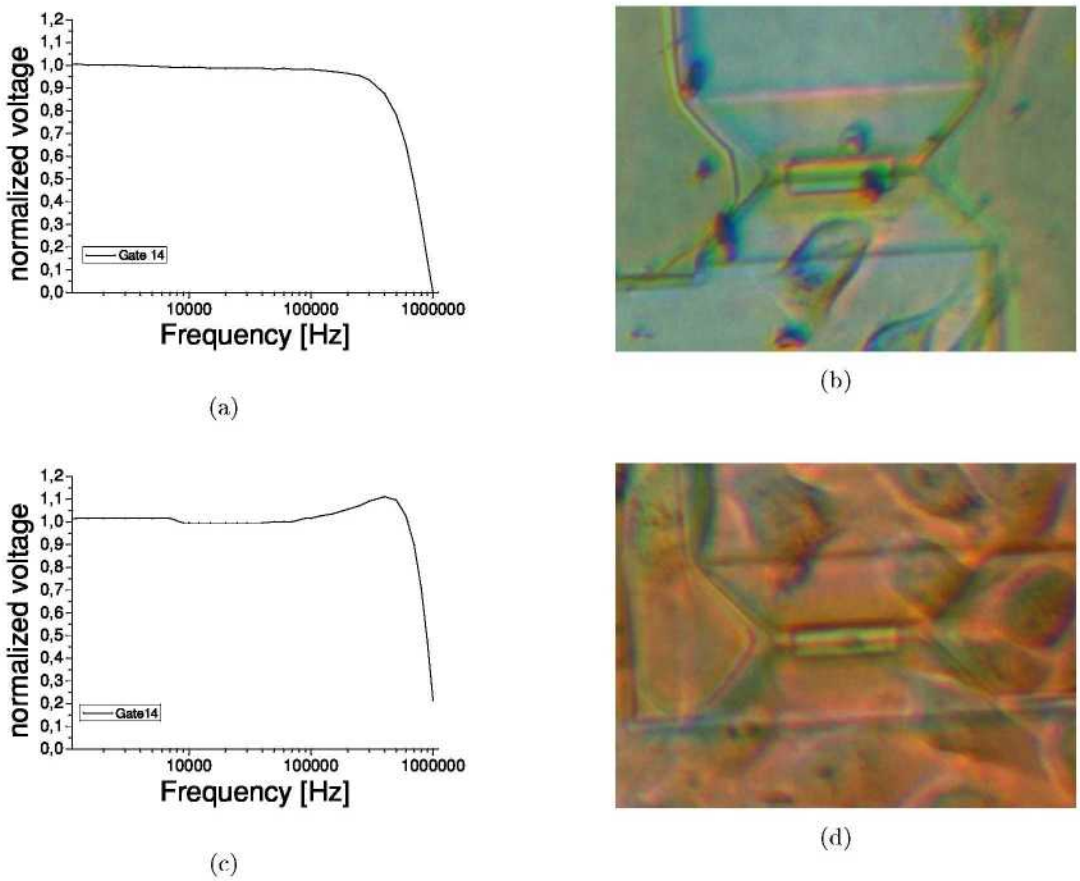

Figure 4.17: (a) shows gate 14 of Figure 4.16, while (c) shows the same gate at a measurement at a later day. In both cases the gate was cell-free ((b) and (d))

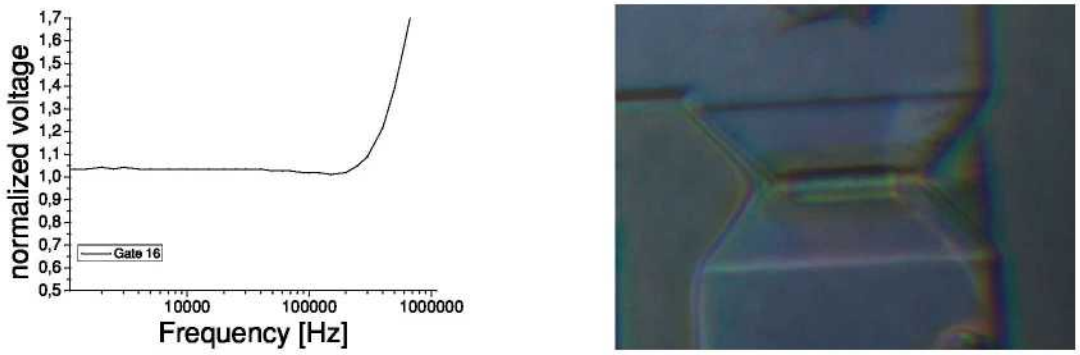

(a) (b)

Figure 4.18: For cell-free gates (b) a sharp bend of the transfer-function towards infinity was commonly observed for high frequencies (a).

For cell-covered transistor gates, most commonly a smoothly curved shape was found (exemplary measurement in figure 4.19). The amplitude decreased to values as low as 0.2 and increased again after a turning point towards infinity. These smoothly curved transfer-functions differed in

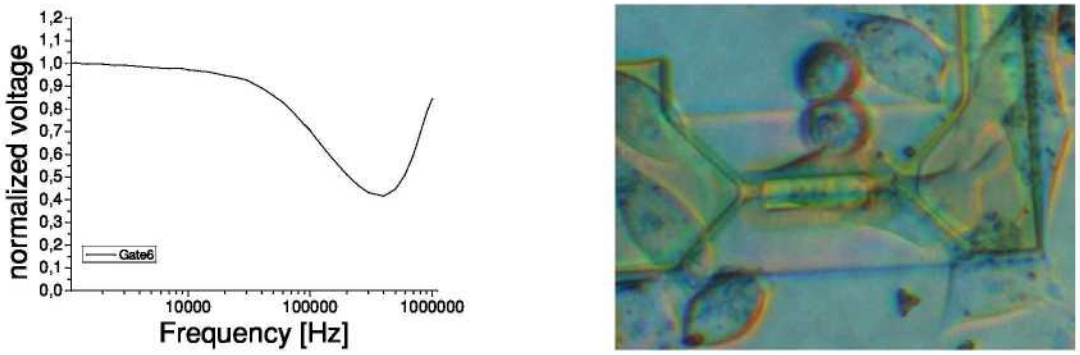

(a) (b)

Figure 4.19: Gate 6 of the first example showed the most common function shape (A). The gate was covered by a spindle formed cell (B).

terms of cut-off frequency and the reached minimum of the amplitude (exemplary measurement in figure 4.20). The cut-off frequencies were found as low as 20 kHz and up to 250 kHz. The turning point of the function was in the range of 100 to 300 kHz. In all measurements, the transistor surface was controlled optically to observe the different morphology of the cells adhering on top of the gates. Gate 7 showed the strongest signal, with two cells spread over the whole gate. The cells appeared to be flat although roundly shaped and were settled close to each other. Gate 13 showed the second highest change in amplitude and was covered by one single cell with a flat cell body. Gate 1 was partially covered by two cells.

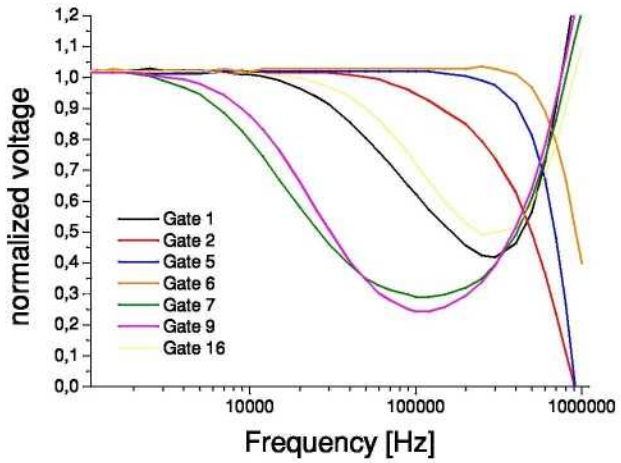

(a)

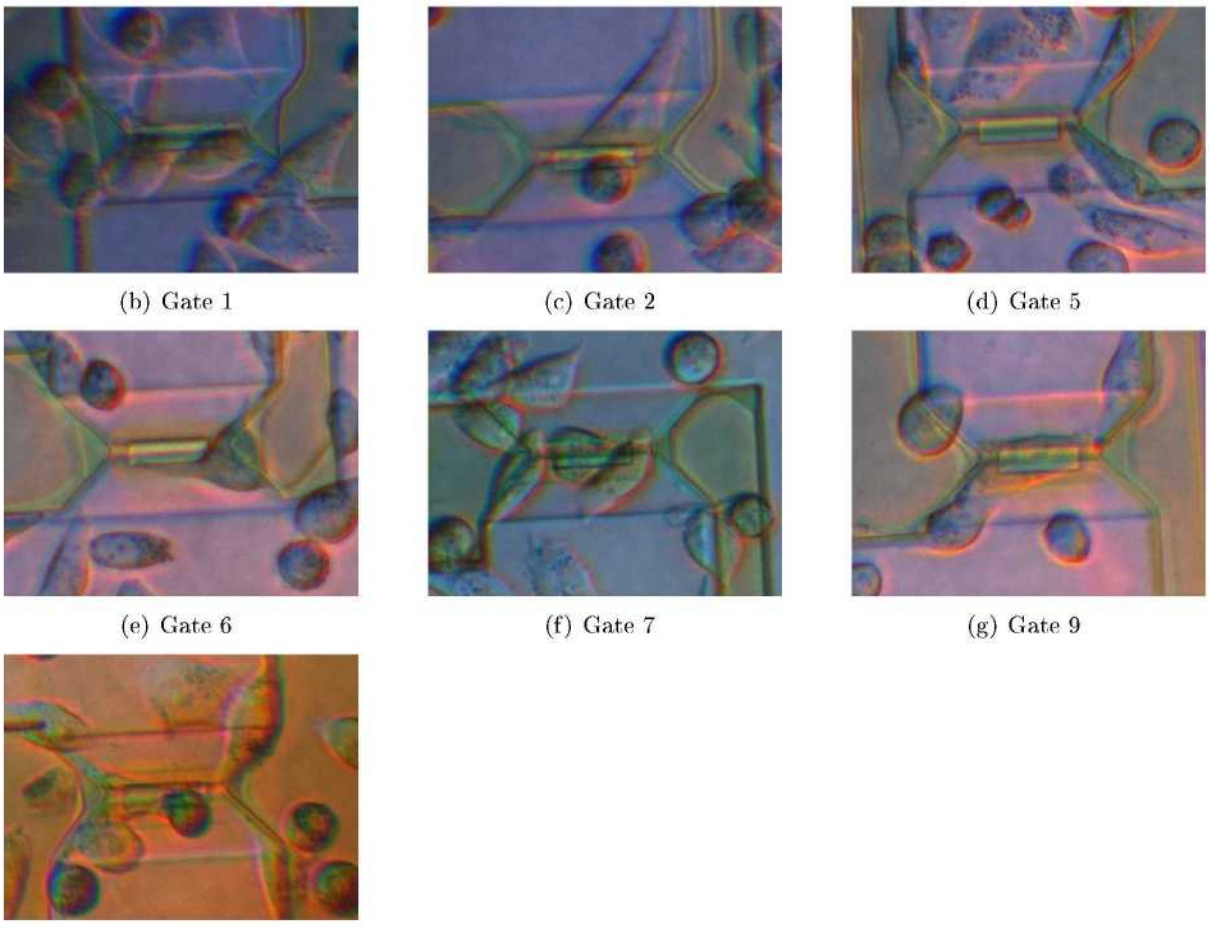

(b) Gate 1

(c) Gate 2

(d) Gate 5

(e) Gate 6

(f) Gate 7

(g) Gate 9

(h) Gate 16

Figure 4.20: The smoothly curved transfer-function shape appeared in various strengths in dependency of the cells adhering to the gates.

On both, gate 16 and gate 2, a small round cell and a bigger flat cell had grown. Finally, gate 5 and 6 were cell-free, although cells had settled in the proximity of the gate. In this experiment a good correlation was found between electrical measurement and optical control. Generally, single cells could be monitored and their morphology showed a high influence on the recorded signal shape.

Besides the transfer-function shapes introduced so far, intermediate shapes were found (Figure 4.21). For those functions, the amplitude decreased in a lower slope. These forms can be divided into two cases again. In the first case the transfe-function had a late turning point at about 400 kHz and increased again (a). In the second case the function showed a saddle point in the range of 200 to 300 kHz and then decreased further (c). For those gates the optical control showed full cell coverage with at least two cells.

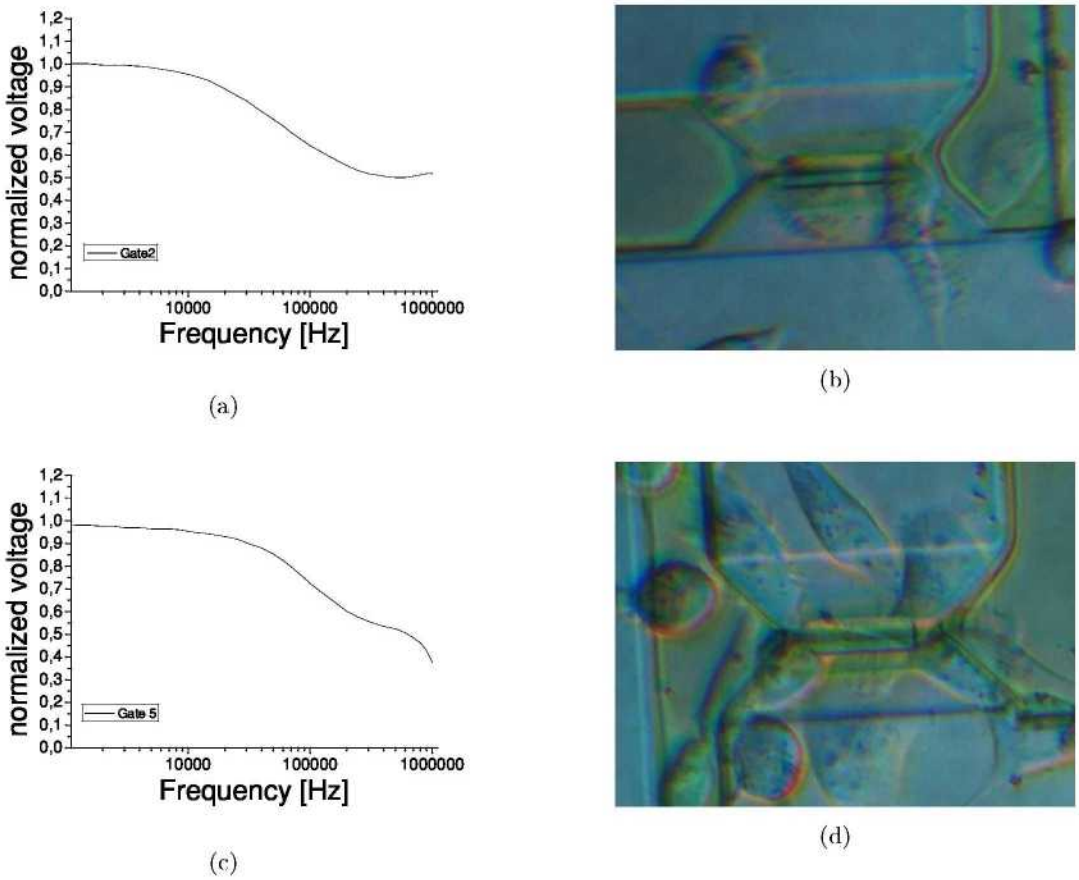

Figure 4.21: The transfer-functions of gate 2 and 5 of the first example showed the so called intermediate shapes.

In an additional measurement (Figure 4.22), two more cases occured (gate 7 and gate 10), which will be further on called inclined shapes ((a) and (c)). They were different from the shapes introduced so far, inclining straight and with low slope before they rapidly decreased from frequencies in the range of 600 to 800 kHz on. For both gates a partial cell coverage was observed, involving two cells for (b) and only one round cell for (d). For reference measurements the cells were mechanically removed with a Q-tip ((a) and (c), red lines).

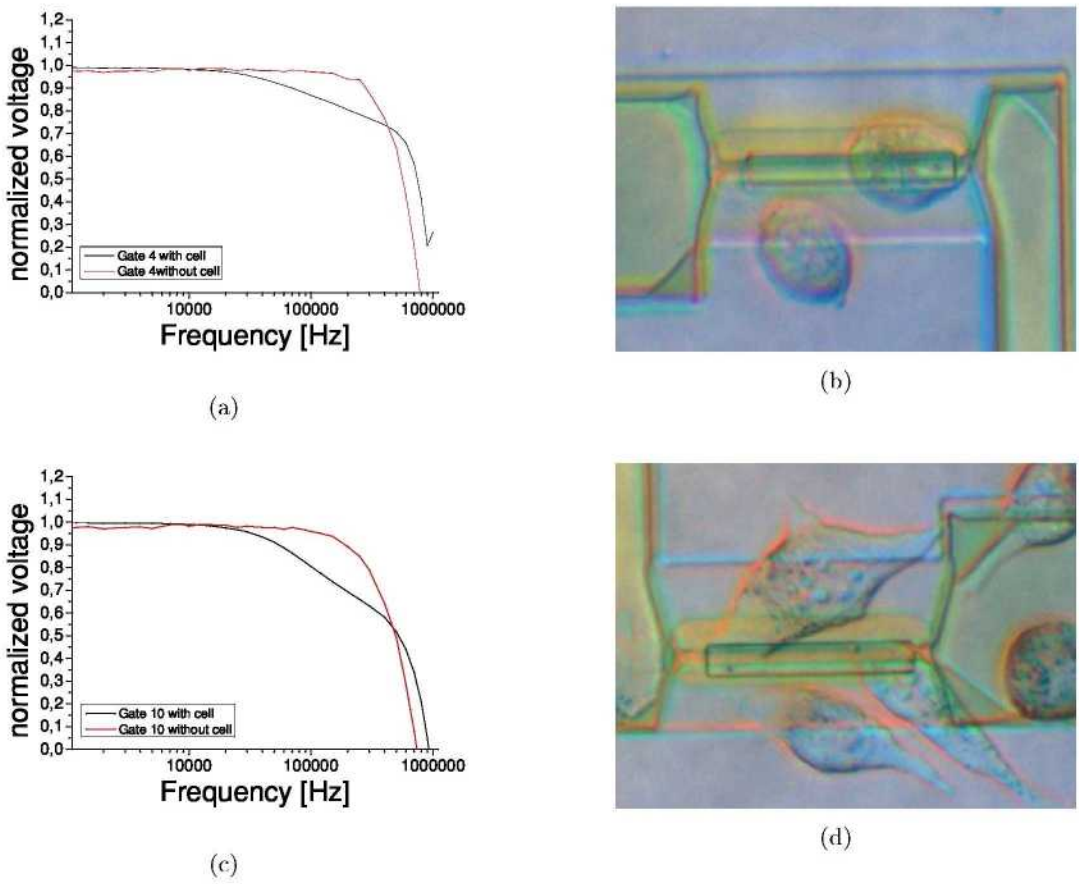

Figure 4.22: The inclined function shapes were rarely observed. Cells were mechanically removed for the respective reference measurements.

Detachment induced by trypsin-comparison before and after detachment

After the first experiments on cell adhesion, the dynamics of the detachment was examined. Trypsin was used to detach the cells without mechanical force. The normalized transfer-functions with adherent cells showed the typical smoothly curved shape with turning points in the range of 150 to 250 kHz and minimum amplitudes between 0.5 and 0.25 (Figure 4.23, solid lines). The second transfer-function measurement was conducted after 10 minutes of trypsin treatment. The functions had changed significantly (Figure 4.23, dotted lines). After cell detachment the turning points were at higher frequencies and the amplitude did not decrease lower than 0.8 at 200 kHz. Nevertheless, only gate 11 behaved like a completely cell-free gate compared to the reference (gate 3). The optical control was taken before the first TF-measurement and after 600 s of trypsin activity (Figure 4.24). Gate 3 was free of cells before and after trypsin treatment. Gate 8 and 10 both were fully covered by one single flat cell before trypsin activity. Afterwards the detached round cells still partially covered the gates. For gate 11 full gate coverage by a single cell was assumed, although the cell membrane was hardly recognized due to its flat shape. After trypsin treatment, the detached cell was then clearly visible, but had retracted from the gate area. On gate 15 two cells of flat spindle shape were found. They also changed their morphology to roundly shaped cells. However, these cells were still loosely attached on top of the gates.

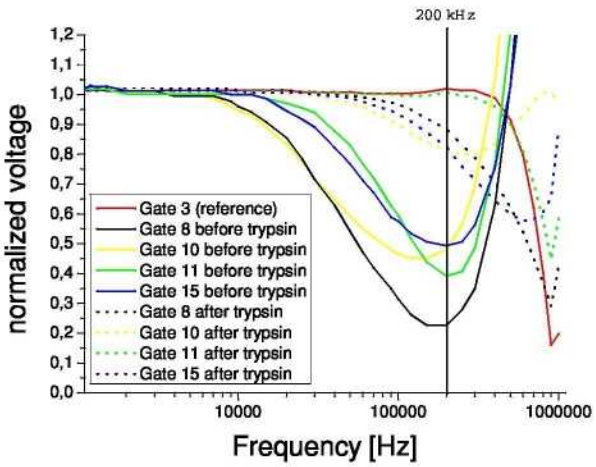

Figure 4.23: The transfer-functions changed due to the treatment with trypsin. Gate 3 served as a cell-free reference gate in this exemplary measurement.

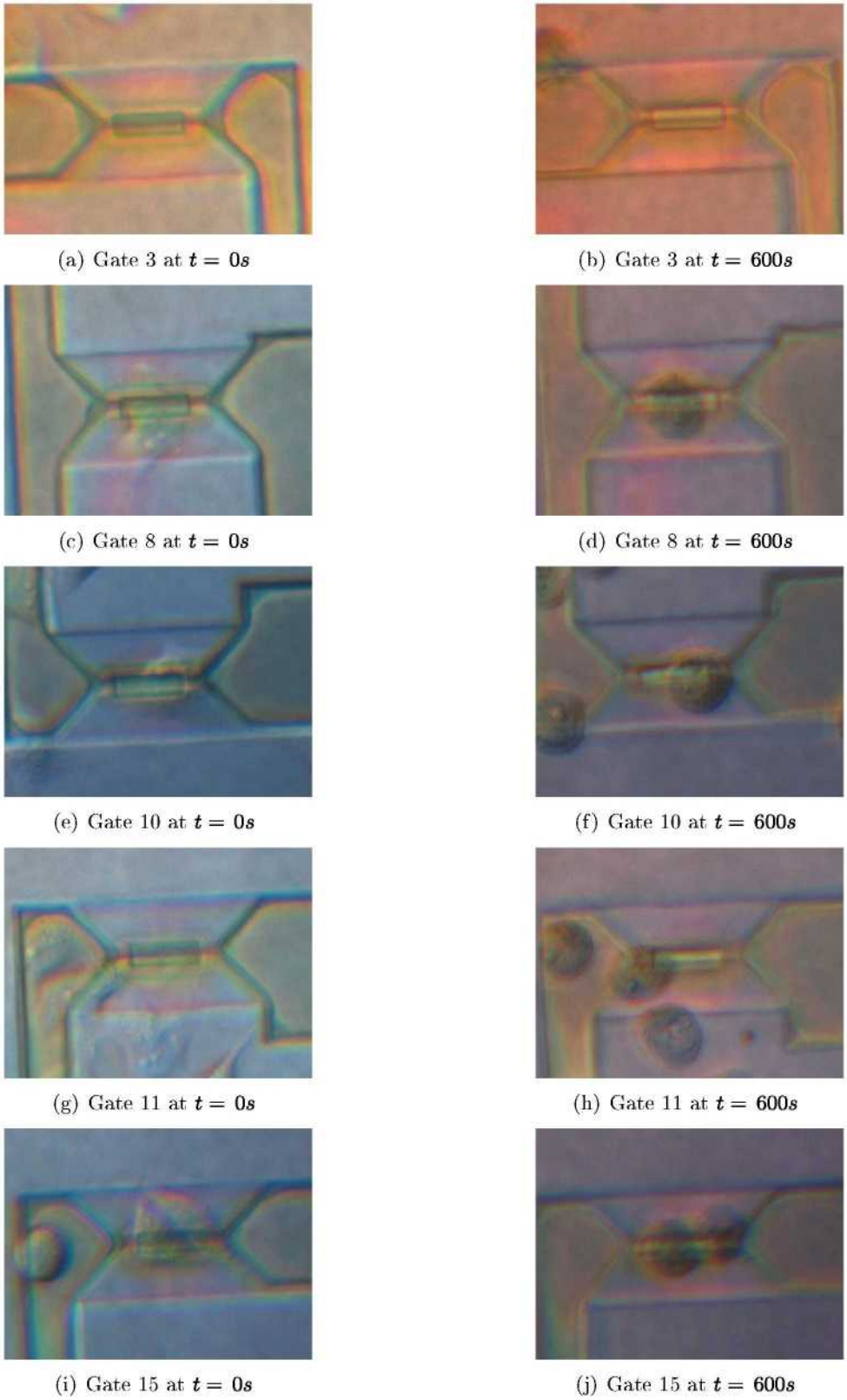

(a) Gate 3 at $t = 0s$

(b) Gate 3 at $t = 600s$

(c) Gate 8 at $t = 0s$

(d) Gate 8 at $t = 600s$

(e) Gate 10 at $t = 0s$

(f) Gate 10 at $t = 600s$

(g) Gate 11 at $t = 0s$

(h) Gate 11 at $t = 600s$

(i) Gate 15 at $t = 0s$

(j) Gate 15 at $t = 600s$

Figure 4.24: The gates of interest were optically controlled during trypsin treatment. Within 600 s the cells changed their morphology and detached from the substrate.

Time-dependent monitoring of trypsin activity

During trypsin activity, the detachment was monitored with a time-dependent TF-measurement at the constant frequency of 200 kHz, as this was the frequency where the highest change in amplitude was expected for most gates (Figure 4.25). The same chip was used for this time-dependent experiment as for the previous comparison before- and after measurement. All cell-covered gates responded with a significant increase in the amplitude within a few minutes after trypsin was added, whereas no change was observed for the reference gate 3. After 6 minutes saturation was reached for all gates. The highest change was measured for gate 8, followed by the gates 11, 15 and 10, respectively. By comparison with the previous experiment this outcome was quite obvious. In the time-dependent measurement, the transfer-function of gate 8 had unsteady points at 70 s and 170 s. After 170 s the function increased with lower slope and saturation was reached after 270 s. Gate 11 behaved in a similar way, exhibiting one unsteady point at 100 s. Also, the function increased with a lower slope afterwards and saturated at 220 s. The transconductance of gate 15 generally increased smoother, reached its highest value at 200 s and saturated at 360 s after a slight decrease. The transconductance of gate 10 increased with a much lower slope than all other gates. It also saturated after 360 s.

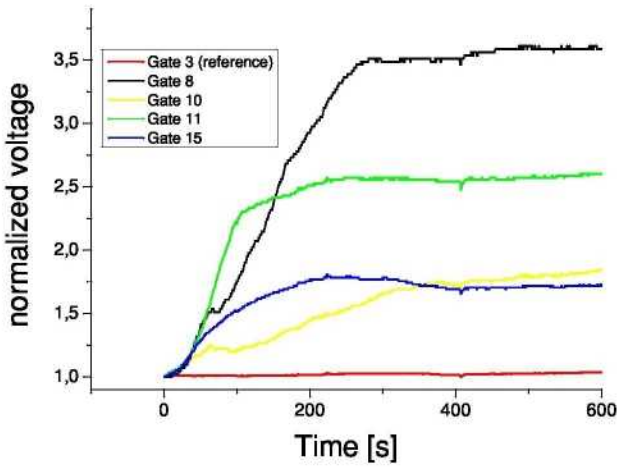

Figure 4.25: Time-dependent measurement of the normalized transconductance. Trypsin was added at $t = 0\,s$, which led to an increase of transconductance for all cell-covered gates. Gate 3 was used as a cell-free reference.

The electrical measurements were in good agreement with the optical control. Therefore, cell detachment was succesfully monitored with the TF-method in Mode 2 (see subsection 3.2.1). Nevertheless, this kind of measurement strongly depended on the chosen constant frequency. When the constant frequency did not match the frequency of the voltage minima, the major changes in the signal could not be detected to their full extend.
Another possibility to monitor the dynamics of cell detachment was the repetitive TF-measurement in Mode 1 with one measurement per minute (Figure 4.26). In the next exemplary measurement, three gates with adherent cells were chosen (Figure 4.26 (a)) and the evolution of the TF-shape was measured during trypsin treatment (Figure 4.26 ((b), (c), (d))). The measurement duration was set to 8 minutes, after which saturation was expected like in the time-dependent measurement. The turning point and therefore the point of lowest transconductance was seen to shift to higher amplitudes and higher frequencies for all three gates in a mostly homogenous manner. While gate 5 responded immediately to the addition of trypsin, gate 1 and gate 9 showed a delay of two and four minutes, respectively, in which the transfer-functions only varied slightly. Furthermore, the voltage increase of gate 1 stagnated between minute 4 and 6 and the function series of gate 5 showed a stagnation between minute 5 and 6. The net increase of the amplitude (measured at the turning point) within 8 minutes of trypsin activity was 0.23 (49%), 0.26 (40%) and 0.24 (63%) for the gates 1, 5, and 9, respectively. The reached minima values of every TF-measurement were fitted linear for gate 1 and exponentially for gates 5 and 9, both methods matching reasonably well (Equations 4.1, 4.2, 4.3).

$$Gate1 : f(x) = -0.7105 + 5.1527\,10^{-6} \cdot x \tag{4.1}$$

$$Gate5 : f(x) = 0.00008 \cdot exp\left(\frac{x}{51389}\right) + 0.4321 \tag{4.2}$$

$$Gate9 : f(x) = 0.00003 \cdot exp\left(\frac{x}{46449}\right) + 0.4491 \tag{4.3}$$

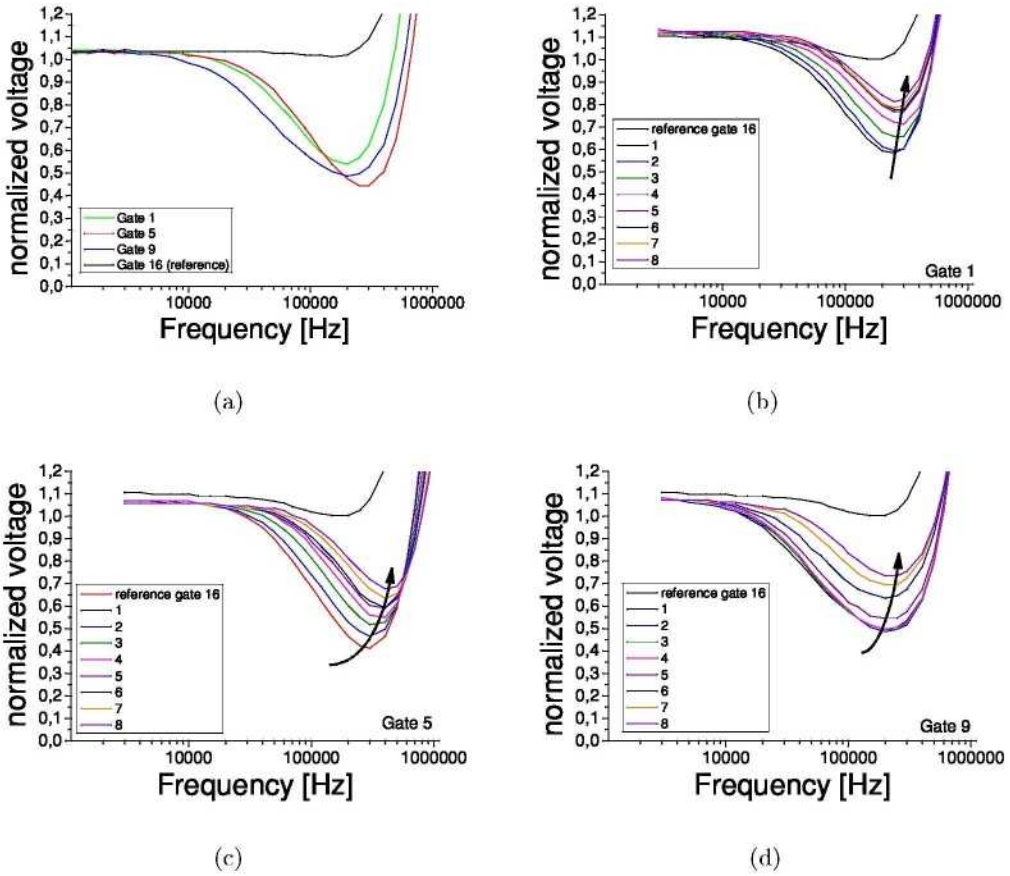

Figure 4.26: Overview of the monitored cell-covered gates (a). The normalized voltage was measured frequency-dependent and over time with one measurement conducted per minute ((b),(c),(d)). The black arrows indicate the shift of the function minima over time.

The optical control (Figure 4.27) showed the initial cell coverage and the change from flat to round cell morphology during trypsin activity. Gate 1 initially was covered by a big round cell and a spindle shaped cell, gate 5 was covered by one round and one flat cell, whereas gate 9 was completely sealed by one flat cell. Although the cells adapted a round morphology over time, they did not fully detach and therefore still caused a partial coverage of the gate area after trypsin treatment.

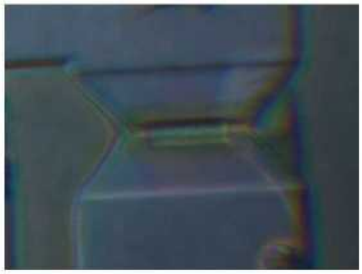

(a) Gate 16 as reference

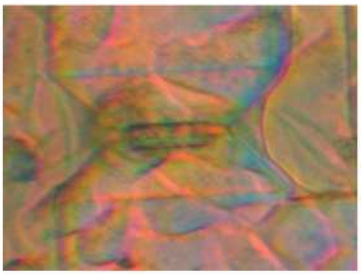

(b) Gate 1 at $t = 0min$

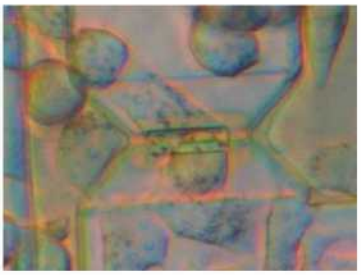

(c) Gate 5 at $t = 0min$

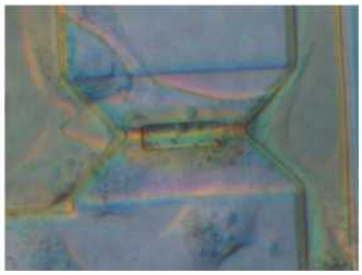

(d) Gate 9 at $t = 0min$

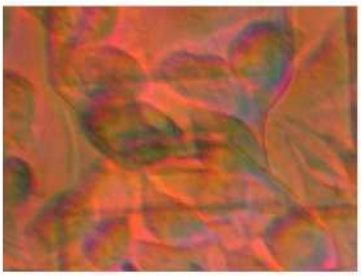

(e) Gate 1 at $t = 2min$

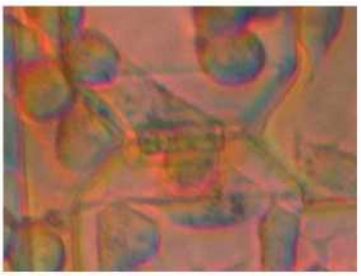

(f) Gate 5 at $t = 2min$

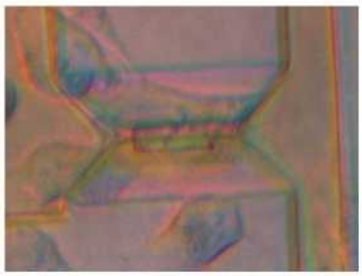

(g) Gate 9 at $t = 2min$

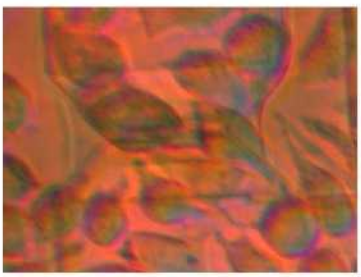

(h) Gate 1 at $t = 4min$

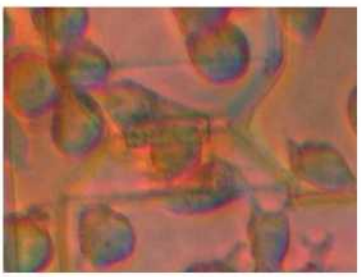

(i) Gate 5 at $t = 4min$

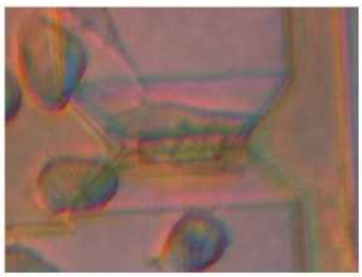

(j) Gate 9 at $t = 4min$

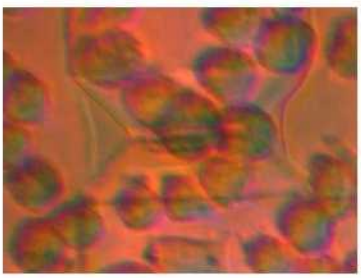

(k) Gate 1 at $t = 8min$

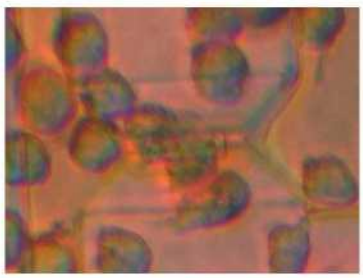

(l) Gate 5 at $t = 8min$

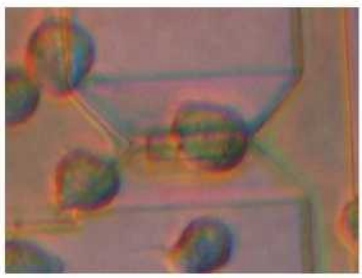

(m) Gate 9 at $t = 8min$

Figure 4.27: The cells on the gates 1, 5, and 9 detached and changed their morphology due to trypsin treatment. Gate 16 was used as a cell-free reference gate.

Influence of Amphotericin on the cell membrane

In this experiment the cells were treated with the ionophore *Amphotericin B* (AmB). Instead of directly changing the seal resistance by protein cleavage, the membrane properties were affected by permeabilization. The transfer-function measurement of all gates mostly showed the typical curved shape (Figure 4.28). Three gates with a high change in voltage amplitude were chosen for the repetitive TF-measurement in Mode 1 (gate 11, 12, 16). Gate 3 served as reference gate as it was free of cells. Transfer-functions were repetitively measured for 15 minutes with

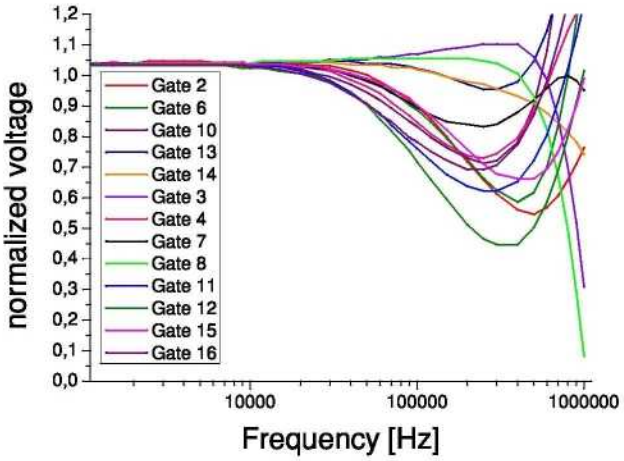

Figure 4.28: For the AmB experiment, firstly a frequency-dependent TF-measurement was done and gates with a high signal change in normalized voltage were chosen. Gates 11, 12, and 16 were selected and gate 3 served as reference gate.

one measurement per minute (Figure 4.29). For the AmB measurement, a completely opposite behaviour was observed compared to the trypsin measurements. Generally, the minima of the transfer-function shifted to lower frequencies and lower normalized voltages. This can be seen in Figure 4.29 (a) and (c). The overall change in magnitude after 15 minutes of AmB treatment was determined to 0.18 (27%) and 0.25 (33%) on gates 11 and 16, respectively. It was found that the major shift took place after three to four minutes. Again, the shift of the minima was fitted exponentially (Equations 4.4 and 4.5), which matched reasonably well. For gate 12 a less regular behaviour was found (Figure 4.29 (b)). After two minutes, the minimum of the transfer-function had shifted upwards and to a lower frequency, before declining for the remaining duration of the measurement. Due to the upwards shift at the beginning of the measurement the overall change in the minimum voltage was neglectable compared to the other cell-covered gates. The reference gate was seen to stay stable without significant shifts.

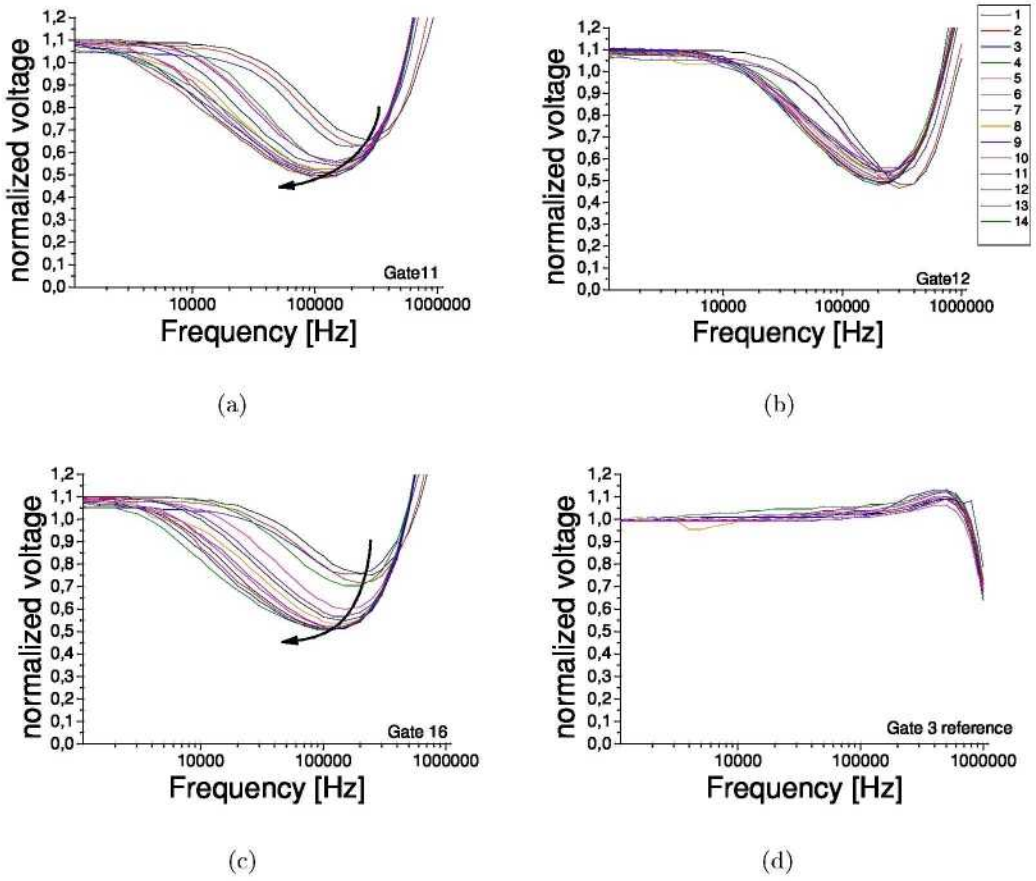

Figure 4.29: The repetitive TF-measurement in Mode 1 was conducted for three cell-covered gates and a reference gate (d). The minimum of the normalized voltage was seen to shift towards lower voltage values and lower frequencies.

$$Gate11 : f(x) = 0.54647 \cdot exp\left(\frac{x}{636609}\right) - 0.15118 \tag{4.4}$$

$$Gate16 : f(x) = 1.54 \cdot exp\left(\frac{x}{970468}\right) - 1.19369 \tag{4.5}$$

By the optical control, gate 11, 12 and 16 were confirmed to be fully covered by at least two cells, while gate 3 was free of cells. In the first 4 minutes of the AmB treatment the cells still looked healthy, but became increasingly permeabilized with ongoing AmB activity. After 9 minutes they seemed to start collapsing and adapted an extremely flat morphology. After 15 minutes the cells were assumed to be dead, due to the permeabilization. In this measurement an increase in the normalized voltage had been expected due to a bigger leakage current through the cells interior. On the contrary, a decrease in the minimum voltage values was found. Furthermore the frequencies at which the minima occured were shifted to the left. Although the cell membrane was permeabilized and the cell viability was clearly affected, the sealing properties of the cell increased with ongoing AmB treatment.

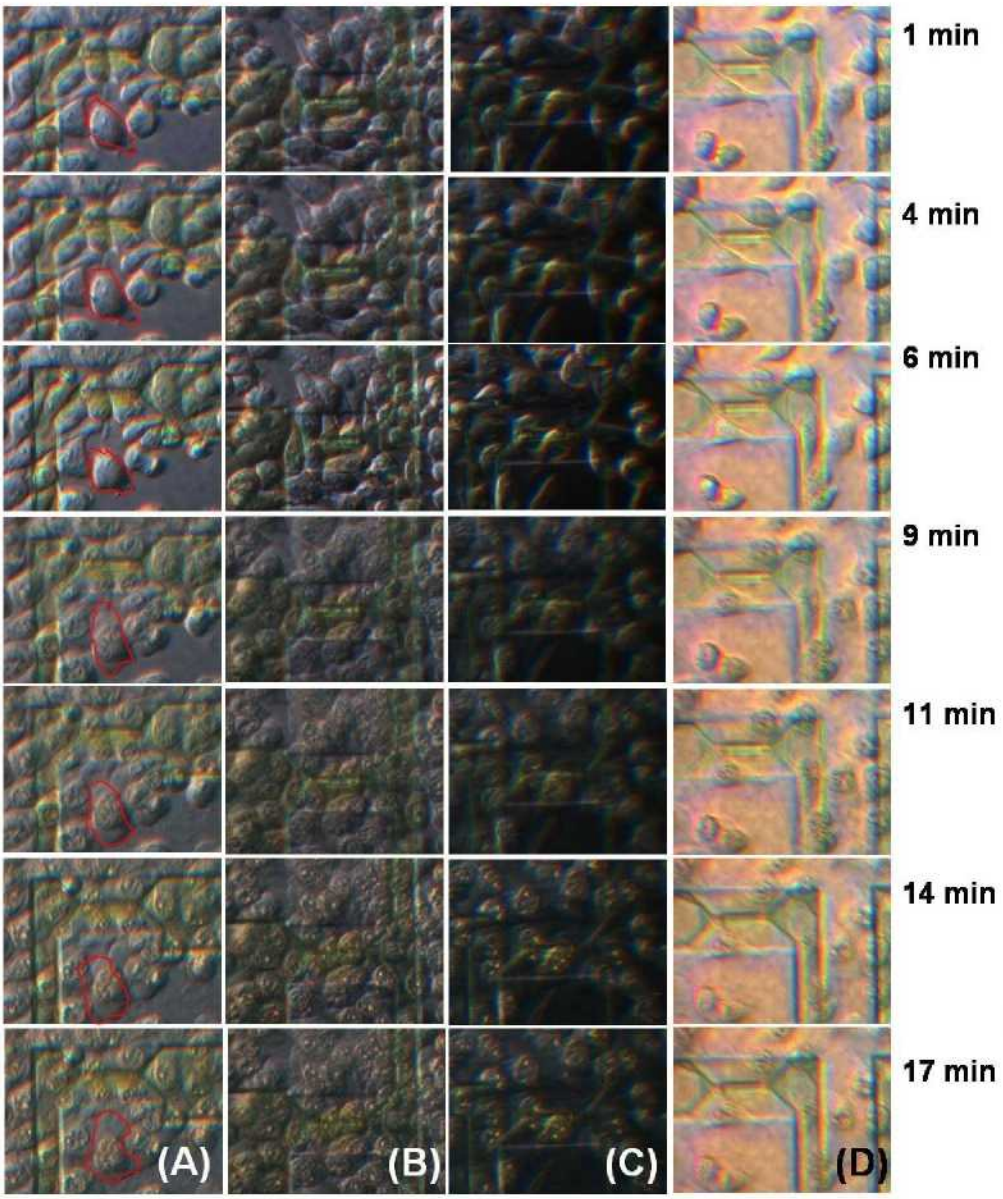

Figure 4.30: During the first minutes of AmB treatment the cells remained intact before being permeabilized (gate 11 (A), gate 12 (B) and gate 16 (C)). Permeabilization also led to a very flat cell morphology ((A), red lines). Gate 3 (D) was used as reference.

Additional measurements of the transfer-function in Mode 2 were performed to gain more information on the dynamics of this system (exemplary result shown in Figure 4.31). The frequency was set to 10 kHz, because the change of amplitude was expected to be high for this frequency. AmB was added after 2.5 minutes and the normalized voltage was followed for another 15 minutes. The transfer-functions responded to the agent immediately and decreased to values in the range of 0.98 to 0.92 for different cell coverage of the gates. After 17 minutes, the voltage had saturated and the measurement was aborted. Although the observed effect was much

smaller compared to the trypsin treatment, a significant change in the normalized voltage values was observed. The decrease of the transfer-function values matched well with the outcome of the continuous TF-measurement in Mode 1. Like in the trypsin experiments, this measurement mode was restricted to one freuquency, omitting possibly bigger effects at other frequencies.

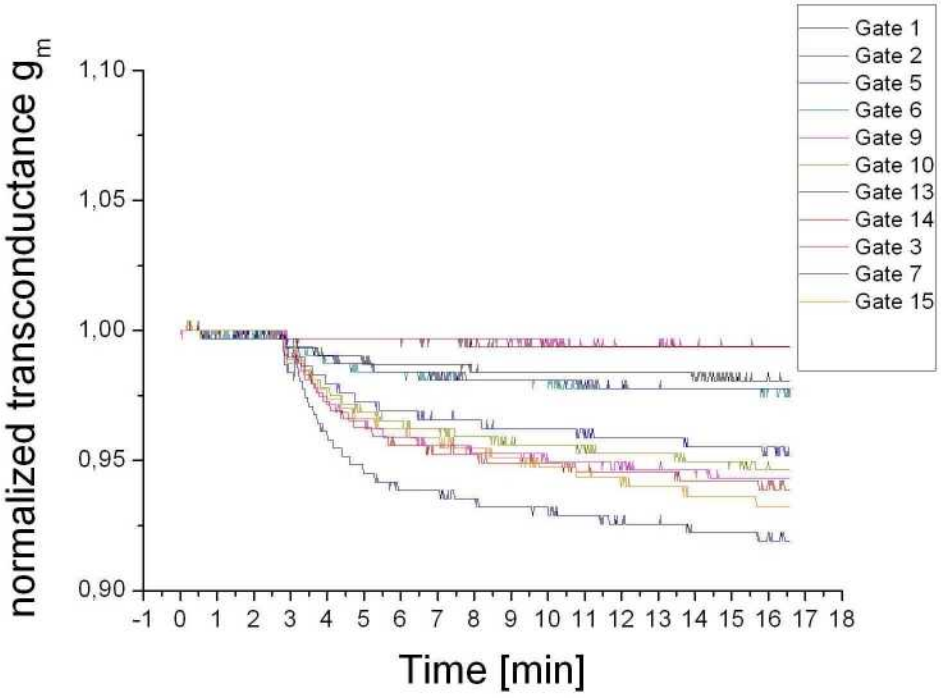

Figure 4.31: The normalized voltage decreased during AmB treatment to minimum values of 0.98 to 0.92. After 17 minutes the values had saturated.

4.2.2 Apoptosis measurements

As a pre-experiment for electrical apoptosis monitoring with FETs, CPT-11 was tested on cells cultured on a chip. The optical control was obtained with a staining kit consisting of annexin-V, which was FITC-labeled, and propidium iodide. At the beginning of the measurement, the cells appeared healthy and CPT-11 was added. After 60 minutes of incubation, the first fluorescence pictures were taken (Figure 4.32). Approximately 50 % of all cells were stained with annexin-V (green) with most them also being stained with propidium iodide (red). This showed, that within 60 minutes 50 % of all cells were apoptotic with the majority being already in a late phase of apoptosis. After 110 minutes another set of fluorescence pictures was taken (Figure 4.33). Then all

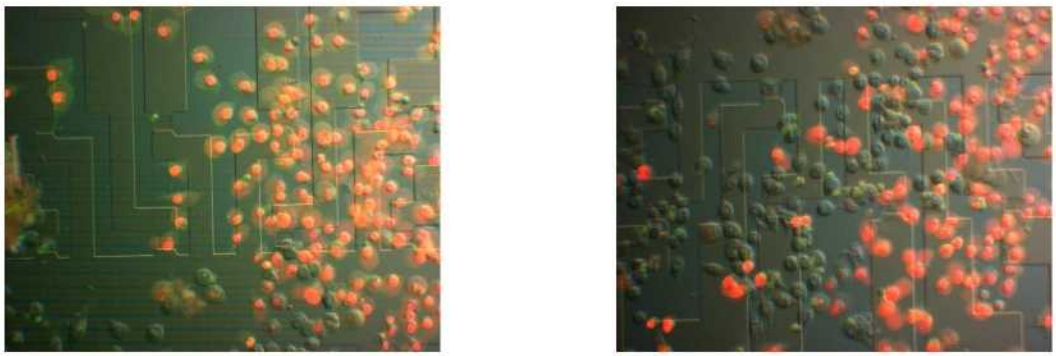

(a) (b)

Figure 4.32: Fluorescent images of EAG cells on a chip surface after 60 minutes of CPT-11 treatment.

cells showed a fluorescent signal for annexin-V and propidium iodide, indicating that all cells had entered a late phase of apoptosis. It was clearly visible for all images that annexin-V only bound to the membrane, while propidium iodide exclusively intercalated with the DNA and therefore only stained the cell nucleus. As a result, early and late apoptosis could clearly be distinguished.

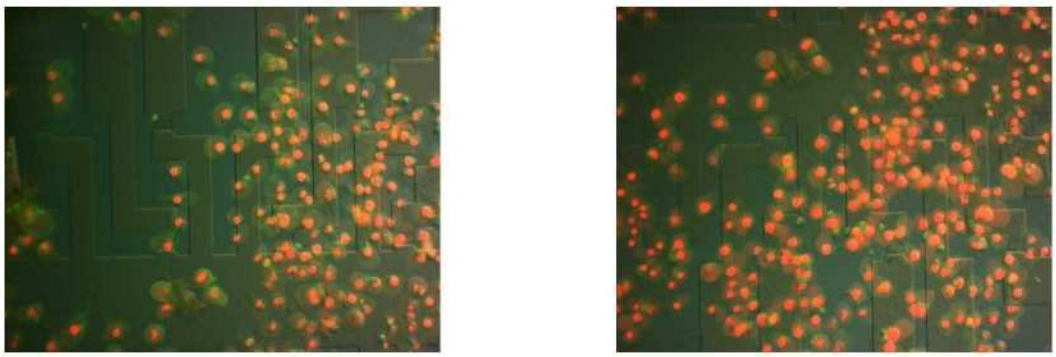

(a) (b)

Figure 4.33: Fluorescent images of EAG cells on a chip surface after 110 minutes of CPT-11 treatment.

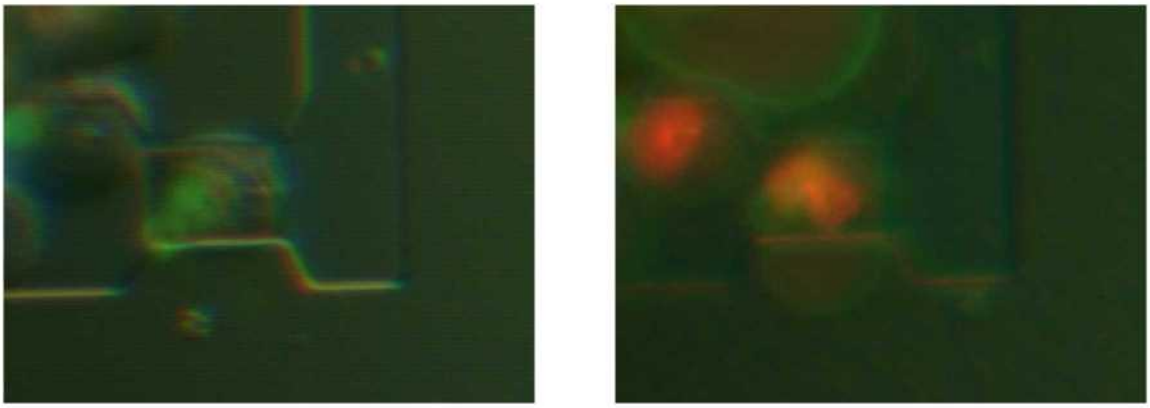

(a) (b)

Figure 4.34: After 60 minutes the cell on gate 2 was found in a state of early apoptosis (a), while it was in a late apoptotic state after 110 minutes (b).

As a proof-of-principle experiment, impedimetric and potentiometric changes in the voltage were simultaneously followed over time (Figure 4.35 (b) and (c), respectively). Furthermore, the transfer-function was compared at $t = 0\,min$ and at $t = 110\,min$ of the CPT-11 treatment, respectively. Hereby, the transfer-function minimum was shifted to a higher frequency, but did not significantly change in amplitude. The transfer-function in Mode 2 was relatively constant druing the first 60 minutes of the measurement, but decreased significantly in amplitude afterwards (Figure 4.35 (b)). Thereby, the overall decrease corresponded to the voltage change of the frequency-dependent transfer functions at 200 kHz (Figure 4.35 (a)). Conversely, for the measurement in Mode 3 no significant changes were detectable (Figure 4.35 (c)). The optical control pictured the cell on gate 2 in early apoptosis after 60 minutes. After 110 minutes the cell was found in the state of late apoptosis (Figure 4.34).

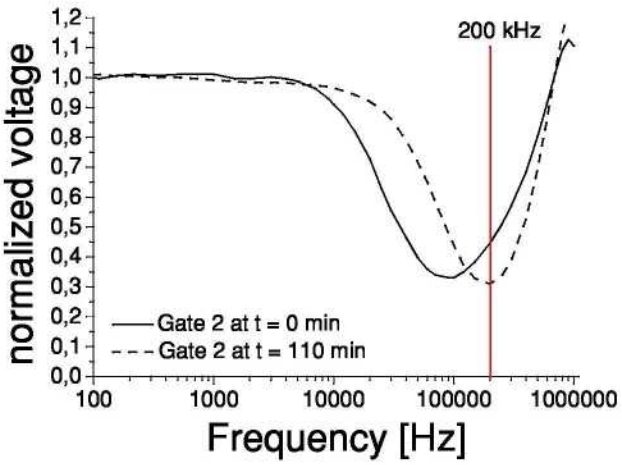

(a) Exemplary transfer functions of gate 2 at $t = 0\,min$ (solid line) and $t = 110\,min$ (dotted line) of the CPT-11 treatment. The red vertical line denotes the constant frequency of the following transfer-function measurement in Mode 2.

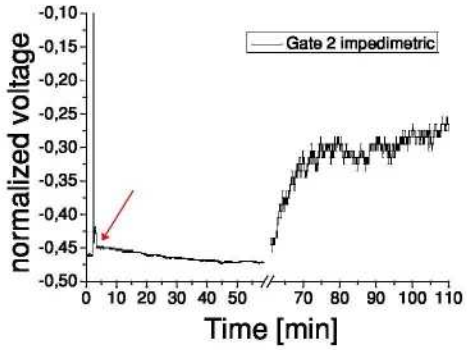

(b) Impedimetric transfer function measurement of gate 2 in Mode 2. CPT-11 was added after approx. 5 minutes (red arrow).

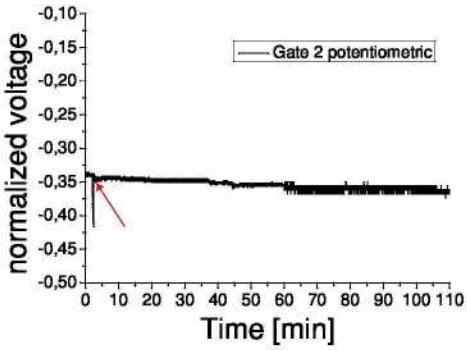

(c) Potentiometric transfer function measurement of gate 2 in Mode 3. CPT-11 was added after approx. 5 minutes (red arrow).

Figure 4.35: Proof-of-principle transfer-function measurement of apoptotic cell on a transistor in frequency-dependent Mode 1 (a), time-dependent Mode 2 (b) and the constant voltage Mode 3 (c).

4.2.3 Vesicles on a field-effect transistor

As a simple cellular model system, vesicles were observed with a TF-measurement in Mode 1. The measurement was conducted in glucose solution (resistivity $\mathbf{3.05 \cdot 10^3\ \Omega}$cm) before addition of the vesicles and after they had settled to the chip surface. The transfer-functions appeared all in the same shape. They had a cut-off frequency of approximately 15 kHz and reached their minimum at 50 kHz. For higher frequencies, the voltage increased again slowly. With attached vesicles the cut-off frequency and hence the voltage minimum was shifted to smaller values. For small vesicles the voltage minimum was found at approximately 25 kHz, exhibiting a shift of 25 kHz compared to the function before vesicle attachment. Nevertheless, the minimum of the normalized voltage did not decrease. The optical control showed that the small vesicles were not directly adhered to the gate. It was assumed, that they had shifted when the objective was immersed. Bigger vesicles were seen to cover the whole transistor gate, causing a shift in frequency and voltage minimum. The minimum voltage was shifted 30 kHz to the left and the magnitude was decreased for 0.09 and 0.06 for gate 11 and gate 16, respectively. In this experiment vesicles were found to show enough sealing properties to be detected with the TF-method. Therefore they are a suitable model system for further experiments.

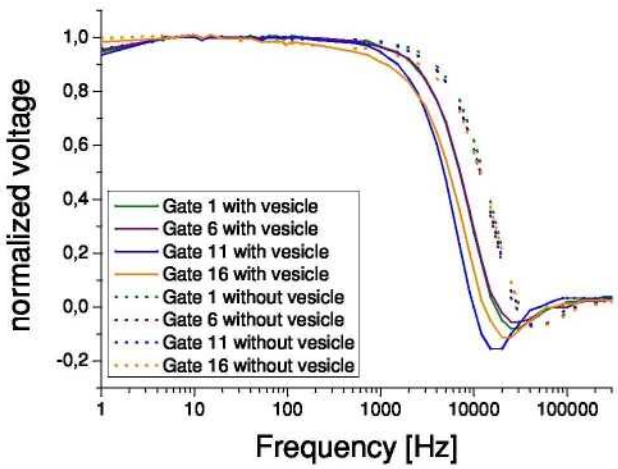

Figure 4.36: Transfer-functions of gates with attached vesicles (solid lines) and without vesicles (dashed lines).

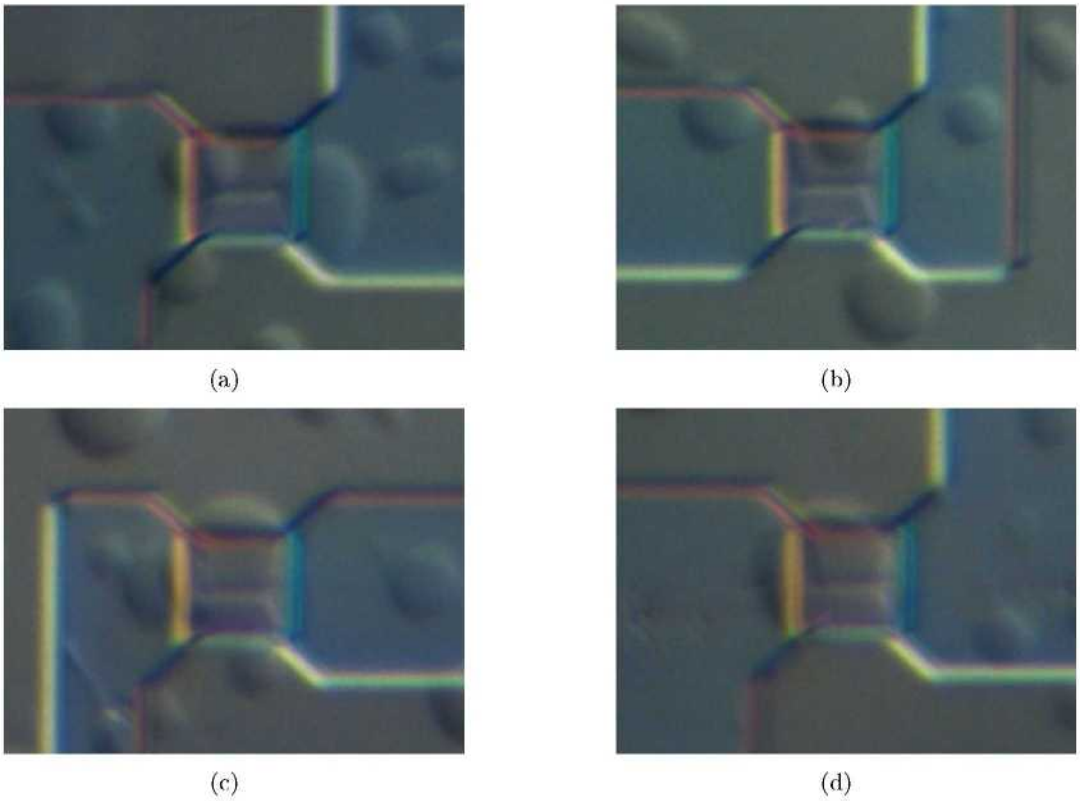

Figure 4.37: Small vesicles were attached to the connections of conducting lines and transistor channel of gate 1 and gate 6, while bigger vesicles completely covered gate 11 and gate 16.

4.2.4 Erythrocyte-ghosts on a Field-Effect Transistor

As a second cellular model system, erythrocyte-ghosts, which had been prepared from red blood cells, were examined with a TF-measurement in Mode 1. ISP7.4 buffer was used as electrolyte (resistivity $8.38 \cdot 10^2\,\Omega$cm). Transfer-functions were aquired and free gates were compared to gates with attached ghosts (Figure 4.38). The general shape of the functions for free gates resembled the vesicle measurements. The cut-off frequency was found at 30 kHz and the voltage minimum lay at approximately 150 kHz. For gates with attached ghosts different transfer-function shapes occured. Two gates showed intermediate shapes with a saddle point at approximately 1 kHz. The transfer-function of a third gate was shaped like the ones for the free gates, but with a smaller cut-off frequency. The voltage minima were not shifted for gates with attached ghosts. Although the ghosts were small in diameter (approximately 7 μm) they could be detected with the TF-method using gates with the width of 6 or 12 μm. Hence the system can be scaled down in size to smaller systems than single cells.

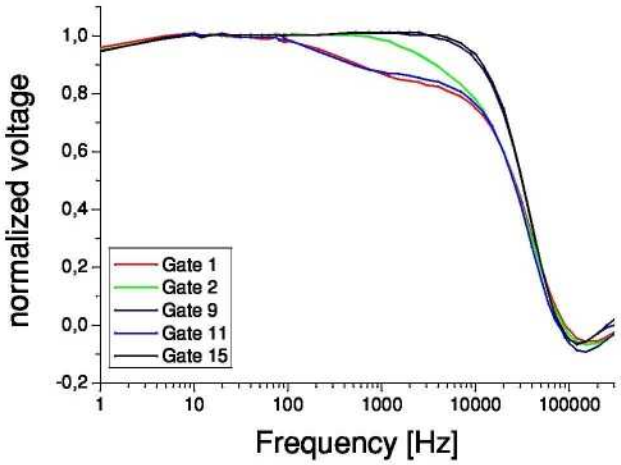

Figure 4.38: Transfer-functions of free gates (gate 9 and 15) and gates with attached ghosts in ISP7.4 buffer (gates 1, 2, and 11).

4.2.5 Modelling the TF-system

To get a deeper understanding of the obtained results, an electrical equivalent circuit of the system was used (Figure 4.39) (Eschermann [2007]). A sinusoidal ac voltage was applied with a Ag/AgCl electrode to the electrolyte solution. The electrode and the electrolyte contributed to the circuit with a resistance R_{el} in parallel to an interfacial capacitance C_{el}. The capacitive pathway over the conducting lines of the transistor contributed with two capacitances C_{CL}, while the resistance of the conducting lines was denoted with R_{CL}. The transistor itself was characterized by the gate oxide capacitance C_{ox} and the transconductance g_m. The variable g_{DS} was set for the intrinsic channel conductance. For an adherend cell two pathways were assumed. One capacitive pathway over the membrane (C_{mem}) and one ohmic pathway through the cleft, which was given by the seal resistance R_{seal}. The amplification stage was omitted in the circuit.

With this circuit the general influence of some parameters was tested. First, the resistance of the electrode R_{el} was varied. For higher values, the cut-off-frequency of the transfer-function decreased. The same behaviour was observed for higher conducting line capacitances C_{CL}. If C_{CL} was set to a very high value, the transfer-function did not decrease at a certain cut-off frequency, but increased quickly. This behaviour was also seen, when g_m was chosen to be very small. The resistance of the conducting lines R_{CL} was found to have a minor influence on the transfer-function.

For a cell-covered transistor, the influences of the seal resistance of the cleft R_{seal} and the membrane capacitance C_{mem} were examined. For fixed C_{mem}, the cut-off frequency of the transfer-

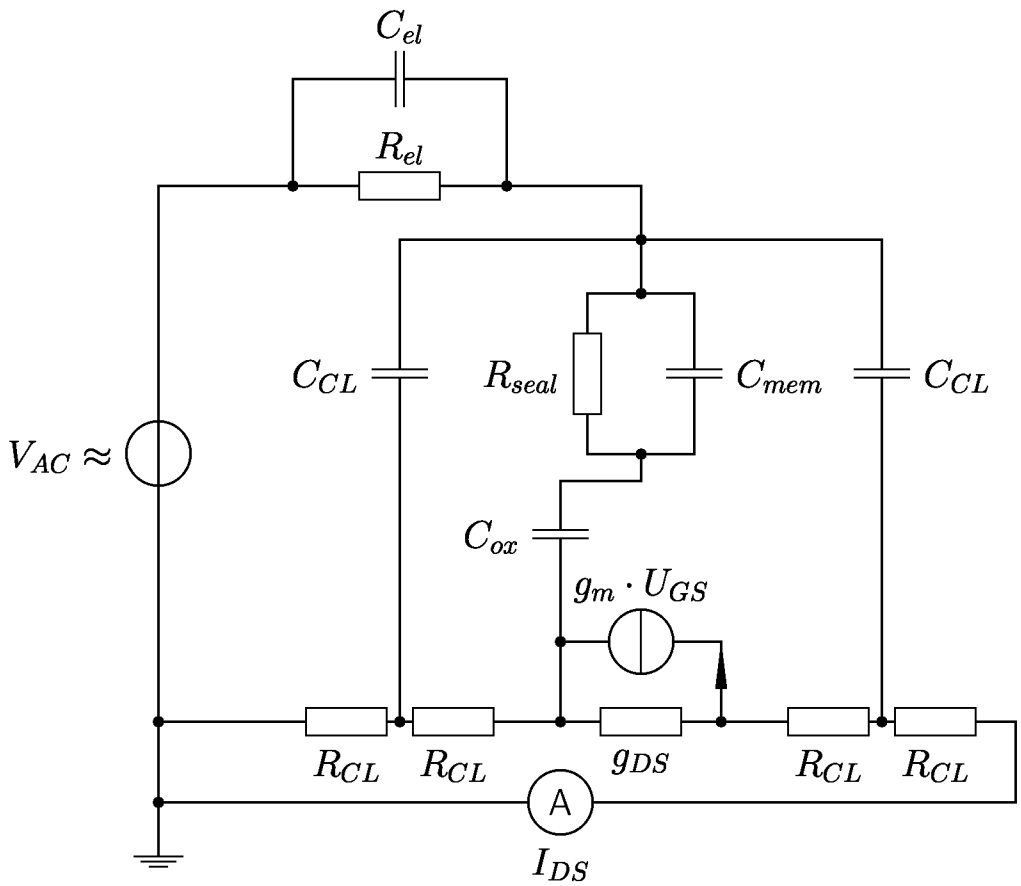

Figure 4.39: Electrical equivalent circuit for the TF-measurements.

function decreased for higher values of R_{seal}. This was also seen for fixed R_{seal} and increased C_{mem}. With more than one parameter varied, almost every shape of the transfer-function of the conducted measurements in this thesis could be obtained. However, the set of parameters was never unambiguous. Furthermore, even small changes of one parameter could change the overall shape of the function dramatically. Two general assumptions were made upon these observations. Firstly, the parameters interacted and could hence not be observed independently. Secondly, the time constants were in a similar range with small changes of the parameters resulting in a different proportionality and hence a different shape of the transfer-function.

To approach this system in a more analytical way, the equivalent circuit was simplified (Figure

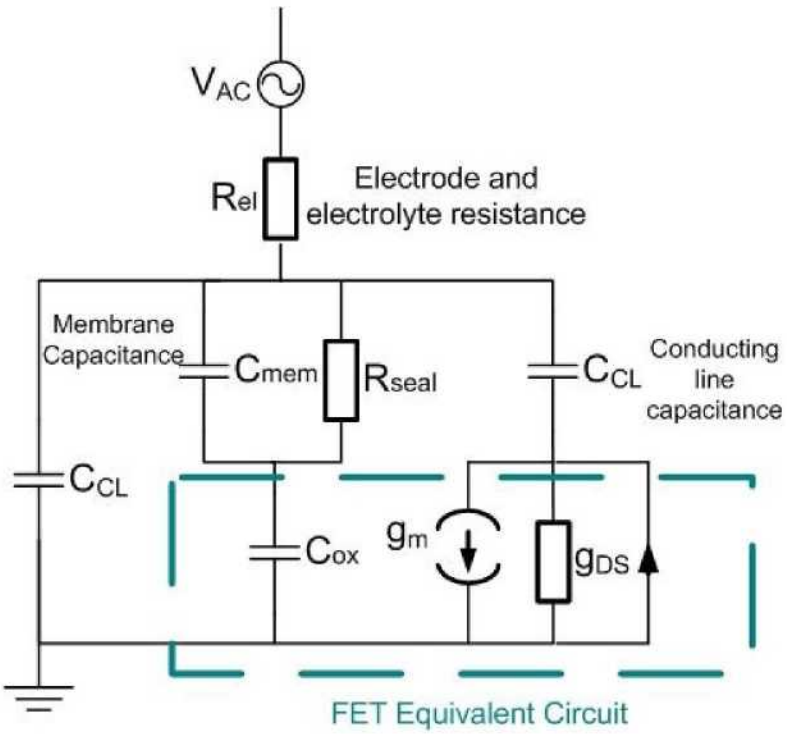

Figure 4.40: Simplified electrical equivalent circuit for a cell attached to a FET.

4.40). From this circuit an equation for the transfer-function was determined by Kirchoff's laws (Dufaux [2007]). As this was quite complex it was simplified with several approximations (Equation 4.6). First of all, the seal resistance was assumed to be much higher than the resistance of the electrode. This is always guaranteed for an adherend cell with the seal resistance usually being in the range of $M\Omega$ compared to the electrode resistance in the $k\Omega$ range. As a second approximation, the electrode resistance was taken to be much bigger than the transconductance, which is between 0.1 and 0.4 mS. The transconductance was taken to be of several orders of magnitude higher than the conducting line capacitance, which was determined to 140 to 180 pF

by the Juelich and planar FET design, respectively. Finally, the conducting line capacitance is much higher than the gate oxide capacitance and the membrane capacitance.

$$R_{seal}/\Omega \gg R_{el}/\Omega \gg g_m/S \gg C_{CL}/F \gg C_{ox}/F, C_{mem}/F \tag{4.6}$$

With those approximations a fairly simple expression was found for the transfer-function (Equation 4.7), which is then governed by four time constants (Equations 4.8 to 4.11). V_{out} is the amplified signal recorded from the transistor. τ_1 and τ_3 are present in the enumerator, while τ_2 and τ_4 are found in the denominator.

$$H(\omega) = V_{out} g_m \frac{(1 + i\omega\tau_1) \cdot (1 + i\omega\tau_2)}{(1 + i\omega\tau_3) \cdot (1 + i\omega\tau_4)} \tag{4.7}$$

$$\tau_1 = C_{mem} \cdot R_{seal} \tag{4.8}$$

$$\tau_2 = -\frac{C_{CL}(C_{mem} + C_{ox})}{C_{mem} \cdot g_m} \tag{4.9}$$

$$\tau_3 = R_{seal} \cdot (C_{mem} + C_{ox}) \tag{4.10}$$

$$\tau_4 = 2 R_{el} C_{CL} \tag{4.11}$$

A precise fit of the experimental data could not be accomplished with unambiguous parameters. Consequently, the time constants had to be analyzed in a qualitative way. A realistic set of parameters was defined:

$$\begin{aligned} R_{el} &= 2\,k\Omega \\ C_{CL} &= 140\,pF \\ g_m &= 0.3\,mS \\ C_{ox} &= 0.08\,pF \\ C_{mem} &= 28\,pF \\ R_{seal} &= 5\,M\Omega \end{aligned}$$

With those, the time constants were calculated to $\tau_1 = 140\mu s$, $\tau_2 = 0.48\mu s$, $\tau_3 = 145\mu s$ and $\tau_4 = 0.56\mu s$. Therefore, τ_2 and τ_4 were in the same range and τ_1 and τ_3 almost coincided. Also, τ_2 and τ_4 were more than two orders of magnitude smaller than τ_1 and τ_3. Hence it was assumed that the transfer-function was determined by the time constants τ_1 and τ_3 for lower frequencies, whereas τ_2 and τ_4 were responsible for the shape at high frequencies. With $\tau_4 > \tau_2$, τ_4 was identified to cause the decrease in amplitude for high frequencies, while τ_2 induced the increase

after the turning point. Now, some special cases were elucidated:

Varying the seal resistance

R_{seal} was set to $0.5\,M\Omega$, $1\,M\Omega$, $2.5\,M\Omega$, $5\,M\Omega$, and $10\,M\Omega$, respectively, with all other parameters persisting as given in Table 4.2.5. This changed the time constants τ_1 and τ_3 (Table 4.5). τ_1 and τ_3 coincided and increased linearly with increasing seal resistance. They dominated the system and caused the transfer-function to drop at lower frequencies (Figure 4.41). This case might be applicable for adherend cells of the same size, but with different distribution of focal adhesions and hence different adhesive strength. It is noteable, that the seal resistance is also changed with changing conductivity of the electrolyte. Therefore R_{el} has an indirect influence on τ_1 and τ_3.

R_{seal}	τ_1	τ_3
$0.5\,M\Omega$	$14\mu s$	$14\mu s$
$1\,M\Omega$	$28\mu s$	$28.1\mu s$
$2.5\,M\Omega$	$70\mu s$	$70.2\mu s$
$5\,M\Omega$	$140\mu s$	$140.4\mu s$
$10\,M\Omega$	$280\mu s$	$280.8\mu s$

Table 4.5: Time constants τ_1 and τ_3 for different seal resistance values.

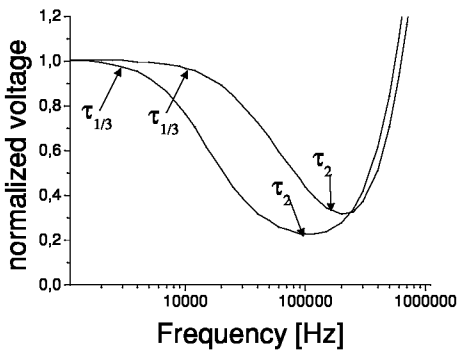

Figure 4.41: τ_1 and τ_3 increased for increasing seal resistance R_{seal}, causing the transfer function to drop at lower frequencies.

Varying the membrane capacitance

A change in the membrane capacitance (with all other parameters set to the typical values) affected the time constants τ_1, τ_2 and τ_3. For very small membrane capacitances, the ratio of C_{ox}/C_{mem} became large enough to see a significant difference between τ_1 and τ_3 regarding their absolut value. In this case, the time constants were separately visible in their effect on the transfer-function at low frequencies (Figure 4.42). This could be the case for either a damaged cell membrane or very small cellular systems like erythrocyte ghosts. However, τ_2 also increased for decreasing membrane capacitances, and for $C_{mem} = 0.1pF$ the relation $\tau_1 < \tau_2 < \tau_3$ was found. Taking into account the usually very high seal resistances for erythrocyte ghosts with $R_{seal} = 10\,M\Omega$ the relation $\tau_2 < \tau_1 < \tau_3$ was found. In that case, the transfer-function was first affected by τ_3, followed by τ_1 and then τ_2 and a plateau-like shape was seen for the transfer-function. This example made clear, how difficult the time constants were to tell apart in a real measurement, as their values were all in a very close range.

C_{mem}	τ_1	τ_2	τ_3
30 pF	$150\mu s$	$0.47\mu s$	$150\mu s$
10 pF	$50\mu s$	$0.47\mu s$	$50.4\mu s$
1 pF	$5\mu s$	$0.5\mu s$	$5.4\mu s$
0.1 pF	$0.5\mu s$	$0.84\mu s$	$0.9\mu s$
0.1 pF (R_{seal}=10 $M\Omega$)	$1.0\mu s$	$0.84\mu s$	$1.8\mu s$

Table 4.6: Time constants τ_1, τ_2 and τ_3 for different membrane capacitances.

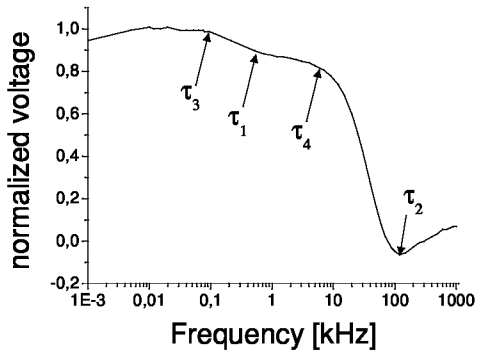

Figure 4.42: Example of a transfer function with all time constants visible. This case occurs for very small membrane capacitances and a high seal resistance.

Varying the electrode and electrolyte resistance

The variation of R_{el} exclusively affected τ_4 (Table 4.7). τ_4 increased linearly for increasing R_{el}. For high resistances, τ_4 was found in the range of τ_1 and τ_3 for small capacitances. Therefore, depending on the chosen parameters, τ_4 might dominate the whole system or partially conceal the other time constants. For the conducted HEK cell experiments this evaluation was not relevant, as R_{el} was about $2\,k\Omega$ for all measurements. On the other hand, for vesicles and erythrocyte ghosts, glucose solution and ISP7.4 buffer were used, respectively. Those solutions had a resistivity of the order of two higher than for extracellular patch solution, which changed R_{el} significantly.

R_{el}	τ_4
$0.5\,k\Omega$	$0.14\,\mu s$
$1.0\,k\Omega$	$0.28\,\mu s$
$2.0\,k\Omega$	$0.56\,\mu s$
$4.0\,k\Omega$	$1.1\,\mu s$
$6.0\,k\Omega$	$1.7\,\mu s$

Table 4.7: Time constant τ_4 for different electrode/electrolyte resistances.

Very small transconductances

As a last case, the influence of the transistors transconductance was examined. All other parameters were set to the typical values. As τ_2 is antiproportional to g_m, the time constant increased for decreasing transconductance. In the extreme case of a transconductance of only $0.05\,mS$, τ_2 would dominate over all other time constants and the transfer-function would increase at a lower frequency as the related frequency for τ_4 (Figure 4.43). In this case, cell-related transfer-function changes would hardly be detected. If we claim $\tau_2 < \tau_4$ and assume $C_{mem} \gg C_{ox}$, a minimum transconductance can be estimated to conduct successfull cell-adhesion measurements:

$$\begin{aligned} \frac{C_{CL}(C_{mem}+C_{ox})}{C_{mem}\,g_m} &\approx \frac{C_{CL}}{g_m} < 2\,R_{el}\,C_{CL} \\ g_m &> \frac{1}{2\,R_{el}} \approx 0.25\,mS \end{aligned} \tag{4.12}$$

g_m	τ_2
0.05 mS	2.8 μs
0.1 mS	1.4 μs
0.3 mS	0.47 μs
0.6 mS	0.23 μs

Table 4.8: Time constant τ_2 for different transconductances g_m.

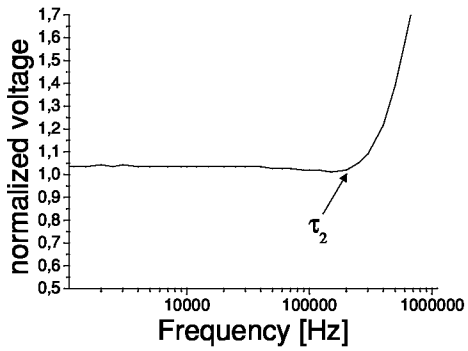

Figure 4.43: For very small transconductances the time constant τ_2 dominates the transfer function.

4.2.6 Fibroblast movement on a FET

Fibroblast migration was monitored with TF-measurements in Mode 2 at a constant frequency of 200 kHz and for a duration of 100 min. All measured transfer-functions were normalized and compared to a reference gate without cell coverage. Cell movement was controlled optically with one photograph per minute. Three different cases were observed for cells grown on a planar p-FET, including fibroblasts approaching a gate, moving on top and leaving the gate again. Those cases will be presented in the following subsections.

Fibroblast approaching a gate

The first measurement started with a normalized voltage value of 0.7, thus being 30% lower than the reference signal. Within 20 minutes two distinct peaks were monitored, before the voltage decreased down to the value 0.24. This steep decrease took place within 6 minutes. For the following 70 minutes no distinct peaks were observed. The voltage varied smoothly between the values 0.24 and 0.35. At the very end of the time measurement the voltage ascended quickly (Figure 4.44).

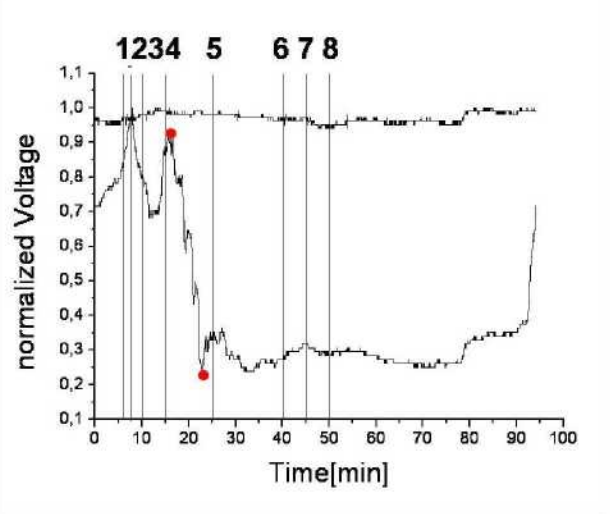

Figure 4.44: Time-dependent measurement of gate 1. The vertical lines indicate when the reference pictures in Figure 4.45 were taken. The red dots mark the time range of the decrease.

In the optical control (Figure 4.45) a fibroblast was seen to approach gate 1 with a part of its membrane. From picture 1 to 4, the cell encountered and retracted from the gate. From picture 5 on, the cell stabilized on the gate and spread its membrane across it, sealing the gate off.

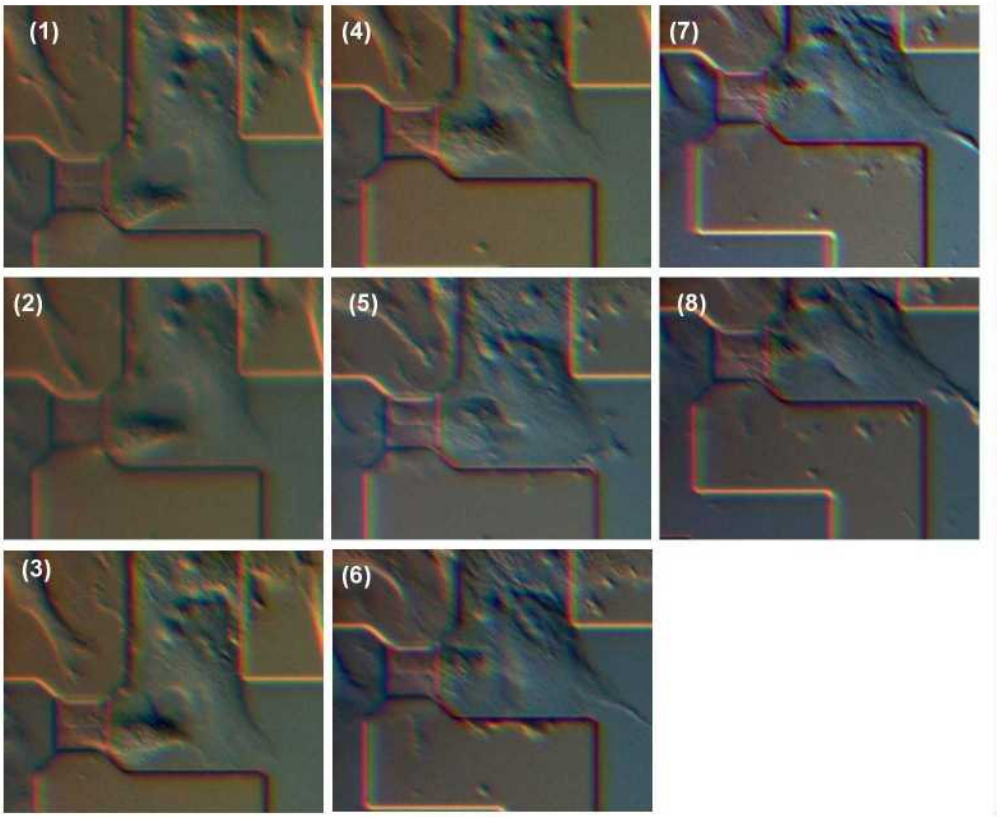

Figure 4.45: Photographs of a fibroblast encountering gate 1. The index of the pictures refers to the vertical lines in Figure 4.44.

A second example of cell approach can be found at gate 4. The transfer-function was found to be less stable and of a ragged appearance. It started at a value of 0.47. Within the first 25 minutes two small peaks were observed with a overall change in voltage from 0.41 to 0.62. During the following 30 minutes two mediate peaks were monitored with the voltage increasing up to the value 0.83. The highest peak was observed after 77 minutes (normalized voltage value: 0.98) followed by a drop to the value 0.47. The measurement was concluded at a voltage value of 0.69. The values measured simultanously to the presented pictures were 0.56, 0.55, 0.88 and 0.69, respectively. The optical control showed a single filopodium moving over the gate. At the first picture, the gate was partial covered by the cell body with a filopodial extension. In the second picture the gate was only covered by a single filopodium. This filopodium was even thinner at picture 3 and 4 and a smaller filopodium was seen to have stabilized next to it.

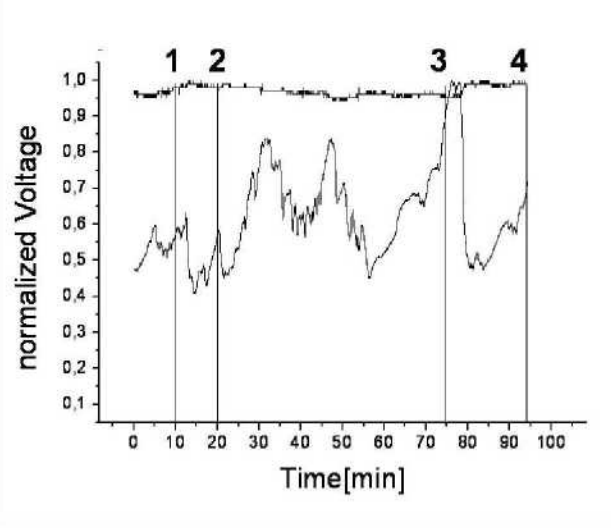

Figure 4.46: Time-dependent measurement of gate 4. The vertical lines indicate when the reference pictures from Figure 4.47 were taken.

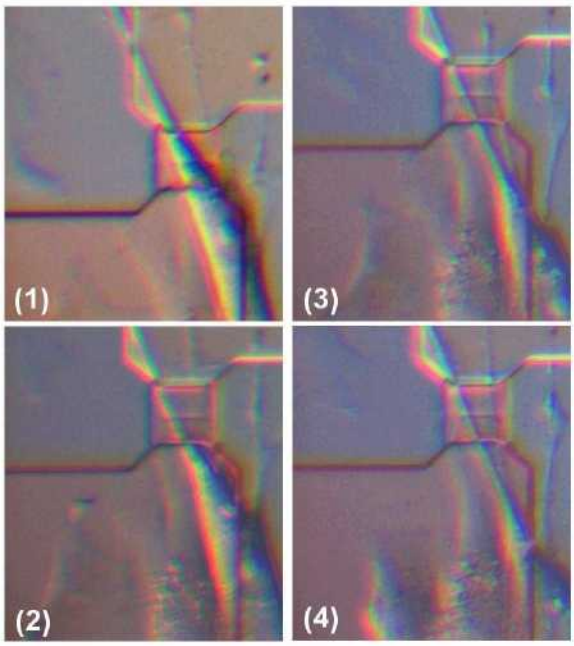

Figure 4.47: On gate 4 two filopodia were observed.

The third measurement of cell approach with gate 8 was characterized by ragged and stable sections of the transfer-function. The measurement started at a value of 0.76. During the first 28 minutes, the function appeared very unsteady, starting with three small peaks with an overall variation of 0.11. Those peaks were followed by three higher peaks exhibiting maxima up to 0.85 and minima down to 0.42. The time of voltage decrease was estimated from the distance of the red dots (Figure 4.48). The voltage values at the reference points were 0.85, 0.53, 0.85 and 0.63, respectively. This ragged section was followed by a wide groove with lower values reaching down to 0.12 for the next 15 minutes. Afterwards the voltage increased quickly (reference point 6: 0.50) within 8 minutes (blue dots) and the function became unsteady again, exhibiting peaks with a variation in voltage of 0.3 (reference point 7: 0.95, reference point 8: 0.91). The normalized voltage decreased to another groove, which showed only very small peaks (reference point 9: 0.31). This decrease took approximately 20 minutes. A last mediate peak was observed after 90 minutes. Towards the end of the measurement the voltage decreased slightly.

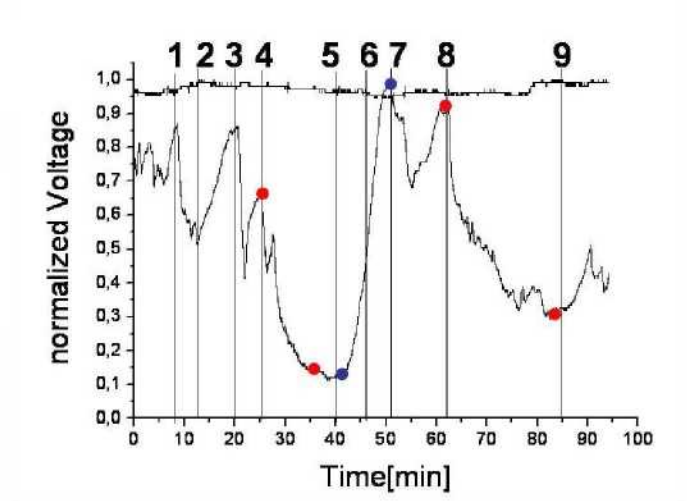

Figure 4.48: Time-dependent measurement of gate 8. The vertical lines indicate when the reference pictures from Figure 4.49 were taken. The decrease and increase times were estimated from the regions between the red and blue dots, respectively.

In picture 1 of the optical control the fibroblast was seen to approach the gate with several small lamellipodia, whereas it had stabilized one big filopodium on picture 2. Picture 3 showed roughly the same situation as picture 1. On picture 4 the fibroblast had further grown onto the gate, also increasing the amount of membrane covering the gate. This process had reached its maximum at picture 5, where the fibroblast membrane sealed the whole gate. Afterwards the cell retracted again, as observed on picture 6. Picture 7 and 8 confirm the further retraction of the fibroblast, leaving the gate almost free of membrane. Yet another approach of the cell was seen in the last reference picture 9. In these first three examples, cell migration was examined for the cell front. The movement of filopodia and lamellipodia was monitored as well as the whole cell body approaching a gate.

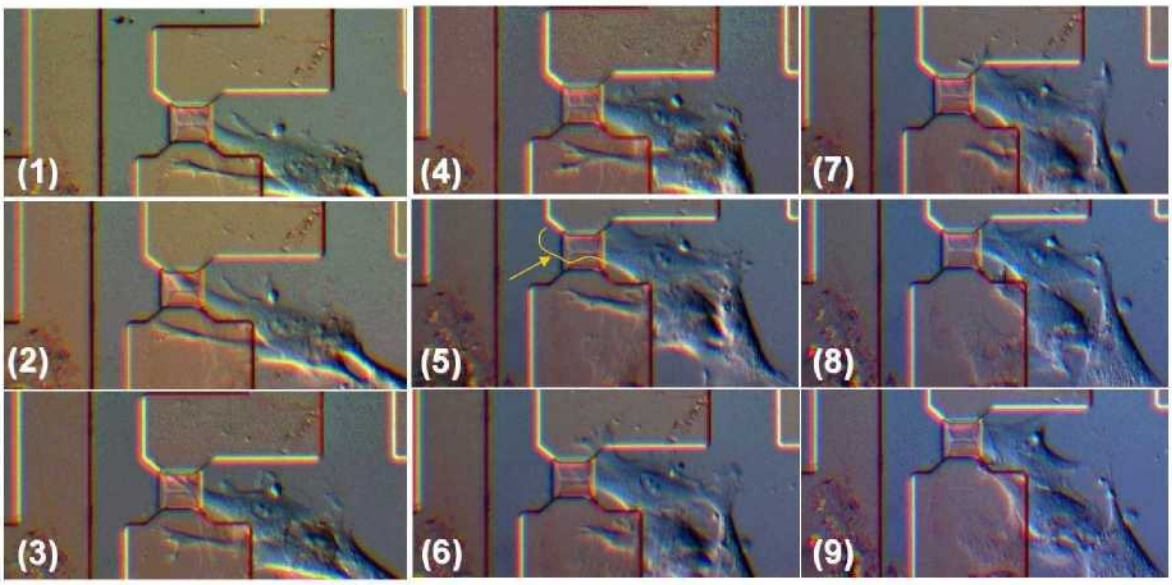

Figure 4.49: Gate 8 was repeatedly covered and left by an approaching fibroblast. Maximum sealing was reached, when the cell streched its membrane across the whole gate (5).

Fibroblast on top of a gate

Another kind of characteristics was found for the time-dependent measurement of gate 12. It had an initial voltage value of 1.0. This value steadily decreased until a final value of 0.28 was reached after 100 minutes. The decline was interrupted temporarily after 8, 46 and 77 minutes, when the voltage increased for several minutes before decreasing again. Those wide peaks were not as sharp as seen for the filopodial movement, but smoothly curved and stable over several minutes. The duration of the single decrease sections (red dots) was estimated to 7, 30, 17 and 10 minutes. In the optical control the fibroblast did not move considerably during the duration of the measurement.

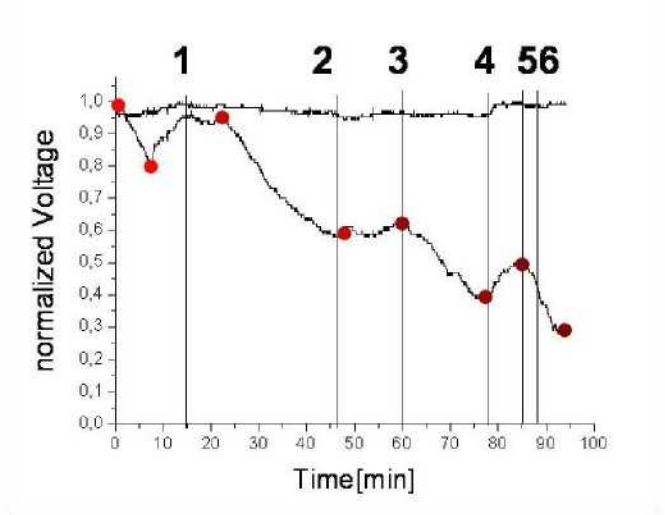

Figure 4.50: Time-dependent measurement of gate 12. The vertical lines indicate when the reference pictures from Figure 4.51 were taken.

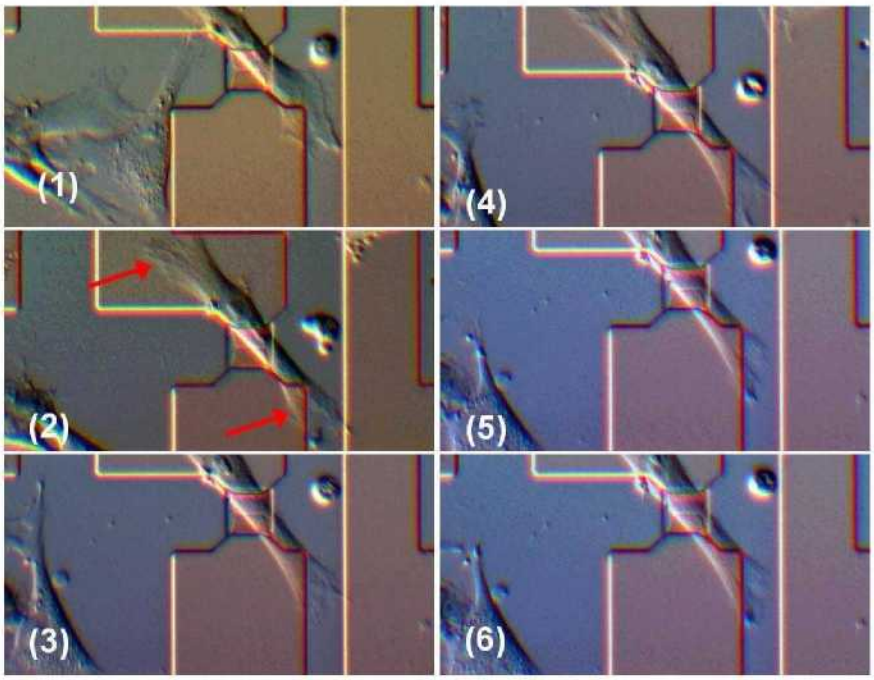

Figure 4.51: The fibroblast did not move significantly during the measurement. The red arrows indicate the regions of high adhesion.

Fibroblast leaving a gate

The last characteristics was found at gate 4 of the same planar FET, but during a different experiment. The measurement started with a value of 0.28 and stayed almost constant for several minutes. After 4.5 minutes the voltage increased abruptly and reached a value of 0.96 within 3 minutes. When the voltage had saturated at a value of 0.99 after 10 minutes, the measurement was aborted. The pictures taken for optical control were aquired in the time range indicated by the vertical lines in Figure 4.53. While the fibroblast was still adherent at picture 1 and 2, the pictures 3 to 6 showed the fibroblast leaving the gate. Finally, on the pictures 7 and 8 the gate was cell-free. This measurement showed the cell activity at the cell rear. The cell rear was detached abruptly within a time range of just 2 minutes (Figure 4.52, blue dots). This behaviour was totally contrary to the cell movement observed for the cell front.

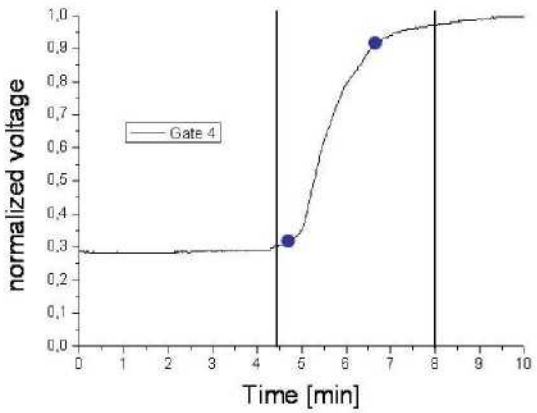

Figure 4.52: The transfer-function showed a sudden increase after 4.5 minutes and saturated within 10 minutes. The vertical lines denote the time range of optical control shown in Figure 4.53.

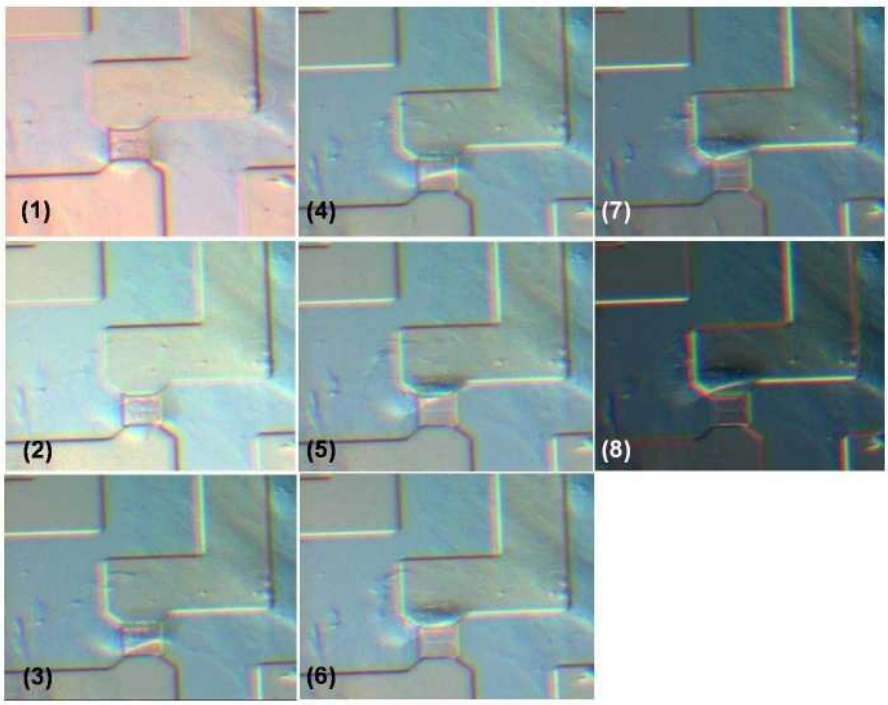

Figure 4.53: A fibroblast covered gate 4 completely before leaving the gate abruptly.

Chapter 5

Discussion

In this chapter the previous results will be summarized and discussed. First, the critical aspects of the planar p-FET process will be discussed, including first and second run, as well as the buried-channel FETs. The main focus of the discussion will be set on the cell adhesion measurements with both, the former Juelich FETs and the new planar p-FETs. The analytical approach to cell adhesion on a transistor will be applied to the conducted measurements. Finally, the cell migration measurements will be discussed.

5.1 Planar p-FET process

Both processes of the planar open-gate p-FET were conducted successfully. The transistors of the first process with a gate length of 3 μm showed typical characteristics, although they had a non-vanishing drain-source current for $V_{GS} = 0\,V$ and hence had no distinct threshold voltage. In this process, the transistors with gate length $1.5\,\mu m$ were not functionable. Both findings originate from the annealing step after the source- and drain-implantation, where boron ions diffused into the gate region and even closed the channel for small gate lengths of 1.5 μm. Due to this effect, larger gate lengths were chosen for the second process and the annealing time was reduced. As a result, all transistors of the second process showed typical characteristics and also distinct threshold voltages. Again, the threshold properties of the FETs were predominantly determined by the anneal after the second implantation. For a large gate width a high diffusion into the gate area and therefore lower threshold values were assumed. Naturally, a higher threshold voltage was expected for a larger gate length. These assumptions were verified for all chips with gate lengths of $4\mu m$ and $5\mu m$, whereas the chips with gate length $3\mu m$ had unexpectedly high threshold

voltages. This effect is not understood, as it is completely contrary to the results of the first process. As most important parameter, the maximum transconductances of all fabricated FETs were calculated. Thereby, the transconductances for the transistors of the first process were found to be at least two times higher than for the FETs of the second process (Table 4.2 and Figure 4.10). This seems to be obvious, as larger gate lengths were fabrictaed in the second process. However, for the completion of further planar FET wafers, gate dimensions and the diffusion step must be optimized to guarantee sufficient transconductances higher than $g_m = 0.25$ for successfull cell adhesion measurements. Additionally, chips with big arrays of functionable transistors with gate length $4\,\mu m$ were fabricated within the second process and can be used after the deposition of a stable passivation layer for future experiments that demand higher integrated chips.

Buried-channel FET processing

For the fabrication of buried-channel FETs, an additional implantation into the gate area was conducted with energies of 5 keV, 10 keV, 15 keV, and 20 keV, respectively. Functionable depletion-mode FETs were obtained for the 5 keV implantation. For the 10 keV implantation, the transistors still showed fairly typical characteristics, although the drain-source current could not be cut off completely, even for high positive voltages. All chips with implantation energies of more than 10 keV could not be controlled by the applied voltages and therefore did not show typical characteristics of field-effect devices. A lower spectral noise density was expected for the buried-channel devices, as the channel was shifted away from the silicon-oxide interface. However, the observed noise spectra showed an almost equal spectral noise density for open-gate an buried-channel FETs with 5 keV implantation. For the 10 keV FETs the spectral noise density was found to be even higher. This can be understood from the increase of defects, which is caused by the implantation with higher energy. Thus, the effect of the noise-decreasing shift of the channel was equalized by additionally caused defects in the Si/SiO_2 interface region. The FETs behaved as depletion-mode FETs, as it was expected due to the additional implantation, which increased the concentration of boron ions in the channel region. Consequently, the transistors showed positive threshold voltages. As a result, these FETs can be operated at $V_{GS} = 0\,V$ and still exhibit sufficiently high transconductances. This property offers a range of new applications like the binding of voltage-sensitive membranes to the FET surface. However, as the buried-channel process was only done as proof-of-principle, several improvements can be done for future processes. The implantation energies should be varied from 1 keV to 5 keV to improve the noise

properties by conserving the SiO_2 and to enhance the control over the channel conductivity. Furthermore, only few working chips were obtained from the buried-channel FET process, because only small samples were fabricated and many chips were lost within the processing. A better gain can be achieved by fabricating a whole wafer of buried-channel FETs in future.

Planarization

The major aim of minimizing the surface topography in comparison to the former Juelich p-FETs without introducing a chemical-mechanical polishing step was fulfilled for both processes of planar p-FETs as well as the buried-channel FETs. For this, the etching times of nitride and oxide layers were balanced in dependence on their thickness. The critical parameter was the etching time for the LOCOS oxide etch with HF. Too long etching times resulted in a positive step height from the gate plateau to the conducting lines, while too short etching caused a negative step height. Although surface profiles were measured before and after the etching, a certain imprecision remained due to the variance in the HF etch rate. For example, stirring caused a higher etch rate than leaving the wafers untouched. Furthermore, the birds beaks could not be avoided totally. They were especially high at the corners of the gate plateau, as oxidation could affect from more than one side. The birds beaks might therefore be reduced by using oval gate plateaus in the next design. Nevertheless, the planarization steps were uncomplicated and precise compared to an approach involving chemical-mechanical polishing. Furthermore, the step heights of 30 nm for the birds beaks can be disregarded compared to the step heights of more than 600 nm for the Juelich p-FETs. Cells were not or only marginally influenced by the remaining step heights and fragile systems like membrane vesicles could be applied without causing them to burst. Moreover, such devices are essential for migration measurements, as topographical cues like edges on the surface usually induce cell settlement and stabilization and hence may abort cell movement.

5.2 Cell adhesion examined with transistor transfer-function measurements

5.2.1 HEK293 cells observed with transistor transfer-function measurements

Cell adhesion on transistors was successfully monitored with the method of frequency-dependent transfer-function measurements. Thereby several different shapes of the transfer-function were observed, which are determined by four time constants governing the system (Equations 5.1-5.5).

$$H(\omega) = V_{out} g_m \frac{(1 + i\omega\tau_1) \cdot (1 + i\omega\tau_2)}{(1 + i\omega\tau_3) \cdot (1 + i\omega\tau_4)} \tag{5.1}$$

$$\tau_1 = C_{mem} \cdot R_{seal} \tag{5.2}$$

$$\tau_2 = -\frac{C_{CL}(C_{mem} + C_{ox})}{C_{mem} \cdot g_m} \tag{5.3}$$

$$\tau_3 = R_{seal} \cdot (C_{mem} + C_{ox}) \tag{5.4}$$

$$\tau_4 = 2R_{el}C_{CL} \tag{5.5}$$

For a cell-free gate the system is dominated by the time constants τ_2 and τ_4 and their proportion to each other. If τ_4 is bigger than τ_2, the transfer-function shows a distinct cut-off at high frequencies, while τ_2 is not necessarily be seen to affect the transfer-function within the measurement range (1 Hz to 1 MHz) (Figure 4.17 (a)). Conversely, when τ_2 is much bigger than τ_4, the normalized voltage increases dramatically for high frequencies and the effect of τ_4 becomes invisible (Figure 4.18). In a special case, when the time constants are equal and the transfer-function decreases after a short increase in a frequency range of 300 to 700 Hz (Figure 4.17 (c)). Hence, for effective cell adhesion measurements τ_4 should be bigger than τ_2. Therefore, a sufficiently high transconductance of the transistor is necessary. Also, τ_4 depends on the electrode and electrolyte resistance R_{el}, which is affected by the properties of the bath electrode (e.g. quality of chloridization). Due to this, the time constant τ_4 may vary slightly from one measurement to the next, possibly changing the proportion of τ_4 and τ_2 to each other.

For adherend cells on top of the transistor gate four time constants have to be considered. The interaction of those time constants leads to the different transfer-function shapes, which were observed troughout this thesis. Most generally, high cell coverage causes a high change in the voltage amplitude. Furthermore, the cell shape influences the received voltage signal strongly. Homogeneously adhered cells with a flat morphology result in higher signal changes than spindle

shaped cells and those again cause higher signal changes than small, round cells. This can be explained by two assumptions. Firstly, flat cells stay closer to the surface than round cells, thus having a bigger area of attached cell membrane and forming a thinner cleft with a higher seal resistance R_{seal} (Hoeller [2005]). Secondly, the cell shape determines the distribution of focal adhesion contacts, being equally distributed for symmetrical cells, but located in the cells extremities for spindle formed cells (Engelhardt [2007]). Therefore, a uniformly adhered cell causes a bigger seal resistance than a spindle cell, where the edge is only partially adhered tightly to the chip surface. Under the assumptions that C_{mem} is constant for cells of roughly the same size and $C_{mem} \gg C_{ox}$, τ_1 and τ_3 fuse to one time constant. τ_3 causes a cut-off frequency at lower frequencies in dependency on the seal resistance. For increasing seal resistance, the transfer-function drops at decreasing frequencies. τ_2 is responsible for the subsequent increase of the transfer-function (Figure 4.20). The observed intermediate and inclined transfer-functions (Figure 4.21 and 4.22) are supposed to result from an interaction of τ_1 and τ_3. If $\tau_3 > \tau_1$, the transfer-function shows a saddle point or decrease in inclination before finally decreasing due to τ_4 at high frequencies. For all measurements the transfer-function data was consistent with the optical control. Therefore, the method might become a reliable tool to monitor cell adhesion on transistor gates. However, to extract quantitative and unambiguous values for the relevant parameters of adhesion like R_{seal} or C_{mem} some problems must be overcome. Firstly, a change in R_{seal} alters two time constants at once (τ_1, τ_3) and for a change of C_{mem} even three time constants (τ_1, τ_2, τ_3) are affected. In reverse this means, that two or even three time constants need to be taken into account to determine the parameters. Only τ_4 is given by the more controllable conducting line capacitance C_{CL} and the electrode and electrolyte resistance R_{el}. Secondly, in a real system the parameters cannot be altered independently, as the addition of chemical agents usually affects the whole system, including the membrane and the cleft geometry between cell and substrate. A first approach was made by choosing trypsin and amphotericin as reagents with predominant affect on R_{seal} and C_{mem}, respectively.

Detachment induced by trypsin

Cell detachment mediated by trypsin was monitored with frequency-dependent and time-dependent transfer-function measurements. In the before- and after experiment (Figure 4.23), the shift of the voltage minima to higher frequencies and higher voltage values was observed upon detachment. Also, the transfer-functions did not reach the cell-free state, due to persistent loose attachment

of the cells to the gate. In the time-dependent monitoring the highest change in transconductance was observed for gates with strongly adhered flat cells (Figure 4.25, gate 8 and gate 10) upon detachment. The absolute change in transconductance might therefore be used as an indicator for the adhesive strength of a cell with a certain morphology. Nevertheless, this kind of measurement strongly depends on the chosen constant frequency. This was illustrated by the function of gate 10 in Figure 4.25. This gate had its minumum transconductance at 150 kHz in the initial measurement and therefore did not show a comparable magnitude of transconductance change, when it was monitored at 200 kHz. Also, when two or more cells covered the gate, the individual processes were masked, as the transistor gate can only sense the overall changes in the transconductance. This probably resulted in the smoother appearance of the transfer-function for gate 15. Finally, the changes in the slope of the transconductance at unsteady points could indicate different phases of detachment. The first phase with a high slope might be due to the cell detachment from the gate and therefore the decrease of the seal resistance. The second phase with lower slope could indicate the change in cell morphology to a round shape, which leads to less cell coverage.

The restriction to one constant frequency was overcome with the repetitive TF-measurement in Mode 1 of the detachment dynamics (Figure 4.26). Due to the trypsin activity the function minima were increased by 40% to 63% and shifted to higher frequencies. Generally, the shape of the transfer-functions did not change when the cells detached and changed their morphology. This firstly implies, that the seal resistance is significantly decreased by the trypsin activity, thereby decreasing the time constant τ_3. Secondly, the membrane capacitance does not decrease far enough to reveal the time constant τ_1. The increase in the voltage amplitude for high frequencies is again caused by τ_2. Thereby we deduce that the involved time constants maintain their sequence of influence. Detachment seemed to happen mostly homogeneous, although showing temporare phases of stagnation. Those stagnation periods might refer to different phases of detachment like observed for the time-dependent measurement. Furthermore, for strongly adhered, flat cells (Figure 4.26, gate 5 and gate 9) the trypsin showed a delayed effect, which is probably due to the limited diffusion of trypsin molecules into the cell-substrate cleft. Therefore, the time of delay is also an evidence of adhesive strength.

Influence of Amphotericin on the cell membrane

The effect of AmB on adherend cells on transistors was successfully monitored frequency- and time-dependently. For both measurement modes a completely opposite behaviour was found, compared to the measurements after trypsin treatment. For Mode 1, the shift of minima to lower frequencies and lower values (by about 30%) (Figure 4.29) implies the increase of the time constant τ_3, which forces the transfer-function to drop at lower frequencies for ongoing AmB treatment. τ_1 is not revealed, indicating that the membrane capacitance is not lowered to the magnitude of C_{ox}. The increase after the turning point is determined by time constant τ_2. These changes suggest enhanced sealing properties of the cells upon ongoing AmB treatment, although the optical control clearly shows the cells' membrane to be perforated, which leads to cell death, eventually. A possible explanation for this discrepancy is the modification in the cells morphology. As the cells die down, they most probably loose structural components maintaining the cell shape. The optical control suggests a collapse due to the lack of mechanical stability and all layers of cell membrane to form a lipid layer-stack very close to the gate. This process also increases the area of coverage. These effects cause a high seal resistance and therefore an increased time constant τ_3. Hence, a certain variation of time constants does not always allow the same conclusions regarding the cells' behaviour. In this case the shift could also have been caused by fortified adhesion instead of membrane permeabilization.
This was also confirmed by the time-dependent transfer-function measurement. Within 5 minutes after addition of AmB the normalized voltage decreased by about 2% to 6%, indicating an increased coverage and sealing of the gate (Figure 4.31). Again, this kind of measurement is highly dependent on the chosen frequency. Compared to the trypsin measurement it is even more delicate to estimate the frequency with the possibly highest change in voltage to occur.

Apoptosis induced by CPT-11

The apoptosis of adherend cells on transistors was visualized with a staining kit containing annexin-V and propidium iodide. Thereby, early and late apoptosis could be distinguished. As proof-of-principle, simulatenous transfer-function measurements in Mode 2 and 3 were conducted to monitor impedimetric and potentiometric changes in the normalized voltage. The decrease of the amplitude in the normalized voltage in the Mode 2 measurement presumably corresponded to changes of the cell adhesion upon apoptosis. However, the impedimetric measurement did not show significant changes and therefore alterations of the pH value in the cell cleft were

not detectable. This might be due to the high buffer concentration in the electrolyte solution. Nevertheless, this could be overcome by the use of an electrolyte containing less buffer. Then, acidification of the cells upon apoptosis could be determined simultaneously to alterations of cell adhesion.

5.2.2 Vesicles and erythrocyte-ghosts observed with transfer-function measurements

The adhesion of negatively charged lipid vesicles was detected with transfer-function measurements. Glucose was used as a buffer with a very low conductivity, resulting in a large time constant τ_4. As expected, the transfer-function showed a drop at low frequencies due to τ_4 (Figure 4.36). With vesicles attached to the gate, the minimum was shifted to even lower frequencies and to lower values, indicating the time constant τ_3 to affect the transfer-function. For the big vesicles, the membrane capacitance is assumed to be much larger than C_{ox} and τ_1 is not affected. For the small vesicles, on the other hand, the membrane capacitance should be comparable to C_{ox}. Still, there is no plateau seen. A possible explanation for this is the large value for τ_4, which might overlap the effects on τ_1.

A similar constellation of time constants was found for the small erythrocyte-ghosts. The transfer-functions exhibited an intermediate shape with a saddle point (Figure 4.38). This can be understood from the conductivity of the buffer solution ISP7.4, which is higher as for glucose buffer. Hence, τ_4 affects the transfer-function for higher frequencies and τ_1 is revealed. The time constants then follow the relation $\tau_2 < \tau_4 < \tau_1 < \tau_3$ and all time constants are visible in the measurement. However, the effects seen are very sensitive to small changes, as those can lead to suppression of single time constants. To reveal all time constants at one measurement, the properties of the system need to be exactly tuned.

For all presented adhesion measurements with HEK293 cells, vesicles and erythrocyte-ghosts, the transfer-function data was highly consistent with the optical control. Therefore, the transfer-function measurements have proven to be a valuable and reliable tool to gain information on the status-quo as well as the dynamics of a single cell or cellular system adhering on a gate. However, a definite reference system for calibration of the method is still missing and will be complicated to achieve. This is mainly due to the different adhesion characteristics for every cell and the unpredictable wear and tear of the transistors during cleaning. However, with a set of definite criteria, values of adhesive strength could be determined from the experimental data. For this

aim, the theoretical approach should be further improved. Once the system is fully understood, the time constants could be adjusted and optimized for cell adhesion measurements. For this, the transistor properties must be adapted, especially regarding the conducting line capacitances and the transconductance. Finally, with a mostly predictable set of time constants, the free parameters could be aquired from experimental data and used to calculate adhesion characteristics, like seal resistance and membrane capacitance.

5.3 Cell migration monitored with transistor transfer-function measurements

Additionally to the cell adhesion experiments, cell migration was monitored with time-dependent transfer-function measurements. The migration behaviour could be divided in processes at the cell front, underneath the cell body, and at the cell rear. Thereby, subcellular activity like filopodia or lamellipodia expansion and retraction was measured. Time constants for the different processes were roughly estimated.

Fibroblast approaching a gate

For three fibroblasts approaching a gate, the cell activity at the cell front was monitored (Figures 4.44 and 4.46 and 4.48). The highest changes in voltage of the transistor compared to the cell-free reference gate was observed for a high membrane coverage of the gate. Conversely, lamellipodia and filopodia caused smaller signal changes indicating their minor size and adhesive strength. Time resolution was sufficient to see single filopodia or groups of lamellipodia stabilize and retract again. These movements generally result in very unsteady regions of the transfer-function, which exhibit a variety of peaks. Cellular movement, that involves the membrane of the cell body, generally leads to a smoother curve. The time constants resulting from the cells' approach to or retraction from the gate are in the same range for all processes at the cell front (6 to 20 minutes). The transfer-function measurements were in great agreement with the optical references. Both methods in combination picture the fibroblast front as highly motile and flexible part of the cell, where continous outgrowth and retraction take place while the cell explores its environment.

Fibroblast stabilizing on a gate

One fibroblast was monitored while stabilizing on a gate (Figure 4.50). This process did not seem to be completed within the measurement range of 100 minutes, as the voltage amplitude still decreased at the end of the measurement. This implies a time constant larger than 100 minutes for cell stabilization. The optical reference shows that the highest concentration of focal adhesion complexes was not located at the cell body, but in the extremities of the spindle formed fibroblast (Figure 4.51, red arrows). Therefore the cell body, which is located on the gate, is only weakly adhered. This is confirmed by the high initial value of the transfer-function. Nevertheless, a steady decrease was electrically measured. As the fibroblast did not move significantly during the measurement, it was assumed to settle. The decrease in voltage is then explained by the formation

of additional adhesion complexes in the region of the central cell body. Those complexes cause a higher seal resistance and therefore a decrease of the measured signal.

Fibroblast leaving a gate

In the last experiment, a fibroblast was monitored leaving a gate (Figure 4.52). This process exhibited the fastest change in the voltage signal compared to all other fibroblast measurements. The time constant for retraction of the cell rear from the gate was approximately 2 minutes. This indicates that only few adhesion complexes have to be retracted to loosen the cell from its substrate.

The results of this section coincide nicely with the general knowledge about the gradual distribution of focal adhesion complexes of migrating cells. While the cell front is attached strongly, the cell rear is weakly bound (Huttenlocher et al. [1995]). Hence the cell generates the traction for a net forward movement. Also, the observed membrane ruffling and the lamellipodial protrusions at the cell front have been well described in literature (Chen [1979], Harms et al. [2005]) based on microscopical data. We conclude, that the monitoring with transistor transfer-function measurements is also suitable to study migration processes. Nevertheless, more experiments are necessary for statistical verification.

Chapter 6

Conclusion and Outlook

Conclusion

In this thesis the method of transistor transfer-function measurements was successfully applied to qualitatively characterize the cell-transistor contact as well as other cellular and membrane based systems attached to the transistor surface. Transistor transfer-functions were aquired frequency- and time-dependently, revealing different properties of the systems. Thereby, multiple transfer-function shapes were measured and interpreted with respect to the time constants of the system. Those constants critically rely on factors like the seal resistance of the cell or its membrane capacitance, as well as the transconductance of the used transistor, its conducting line capacitances, and the resistance of the electrolyte solution. From that, the adhesive strength of the cells could be determined qualitatively and was seen to depend on the cells' morphology. The dynamics of cell detachment and changes upon permeabilization of the membrane were monitored. All cell measurements were conducted on a single cell level and were highly consistent with the optical controls. Furthermore, a staining method for apoptotic cells was introduced. Simultaneous electrical measurements of impedimetric and potentiometric changes in the normalized voltage upon apoptosis were shown. Erythrocyte ghosts and membrane vesicles were successfully prepared and detected upon attachment on transistors with planar surface. The resulting transfer-functions were interpreted with respect to the corresponding time constants. Finally, fibroblast migration was monitored electrically on a sub-cellular level, revealing adhesive patterns of single filopodia and groups of lamellipodia. Different adhesive behaviour was found for the cell front, the cell body and the cell rear. So far, significant values for R_{seal} and C_{mem} were not obtained from the experimental data, as the system was dependent on many interacting parameters. Transistors of the former Juelich p-FETs were used for the first exemplary adhesion experiments, while the

measurements of the cellular model systems and all migration experiments were conducted with the planar p-FETs of the first process, which was completed within this work. Planarity of the transistor surface was successfully achieved, exhibiting step heights of less than 30 nm. The FETs of the second process were not used for cell adhesion measurements, as their transconductance was slightly too low. However, they were ideal as initial FETs for the post-processing to buried-channel FETs. Some wafers were left unfinished for future experiments. Those can be fabricated with higher transconductance by adjusting the second anneal. All transistors were characterized with respect to their threshold voltages, subthreshold slopes and transconductances.

Outlook

In all experiments within this thesis, the system of transistor transfer-function measurements has been proven adequate to monitor adhesion of cells on transistors. This is also valid for modified cell adhesion, e.g. under the influence of chemicals like trypsin or amphotericin. Nevertheless, it will be essential for future experiments to advance the analytical approach and gain a deeper understanding of the interaction of the involved time constants. As the time constants can be almost identical, fine tuning is necessary to develop ideal conditions and hence reveal all information of the respective biological system under examination. This also demands a precise adjustment of the transistor parameters. With partly known time constants, the experimental data can then be used to calculate adhesion related parameters from the measured time constants like the seal resistance (Vassanelli [1997]). The adhesive strength could be determined quantitatively (Merkel et al. [2007]). Furthermore, a reliable calibration system is needed for a better comparability of the results. However, to compete with the elaborate optical methods or to even replace them, unambiguous values for seal resistance and membrane capacitance must be extracted from the experimental data. On the one hand, this requires the precise knowledge of all involved transistor parameters. On the other hand, experiments must be developed to decouple the effects on the single adhesion related quantities and hence facilitate the analytical evaluation. With such a system, a wide range of studies will be possible, as static adhesion as well as dynamical processes on the gate can be monitored with the different modes of this method. As an example, the method could be used to determine the cell viability before patch-clamp experiments on transistors in the frame of cellular signal recording with transistors (Ingebrandt et al. [2005]). The adhesive strength might also be compared with respect to different cell types on various protein coated substrates (Hoeller [2005], Rauf [2007]). For electrogenic cells like heart cells (e.g. HL-1), the

changes in adhesion upon beating could be examined, as the cleft geometry and hence the seal resistance is assumed to change for beating cells (Ingebrandt et al. [2001]). Also, bioassays on a single-cell level can be developed to adress various tasks. These might be toxicology-bioassays (Keese et al. [1998]), e.g. exploring the effects of environmental toxins. Furthermore, anti-cancer agents could be tested by measuring apoptosis rates in the treated cell culture. As it could be possible to sense changes in the pH of the cleft with potentiometric measurements, apoptosis should be detected by monitoring changes in cell adhesion as well as the sensing the typical acidification of apoptotic cells (Barry et al. [1993], Gottlieb et al. [1996]). Experiments over a longer time range could address cell attachment, settlement and proliferation (Keese and Giaever [1991]). Also, cell division and wound healing might be monitored (Keese et al. [2004]). Here, the method reveals its advantages to its full extend, as it should be possible to develop setups that are absolutely non-invasive and do not require to remove the cells from the ideal physiological environment to conduct experiments. Moreover, the adhesive strength during cell migration could be examined for different biochemical cues, also creating directed migration. With the big advantage of subcellular resolution the electrical mapping of neuronal network growth comes into reach. A time-dependent electrical monitoring of neuronal outgrowth, possibly revealing the polarity of the cells, could supplement microscopic observation. Of course, higher integrated transistor chips are required for this task.

Keeping in mind the planarity of the FETs, combined devices for simultaneous stimulation and signal recording of neurons can be developed, using the planar FET process as basis for further processing of electrodes on top (Wallys [2007]). Moreover, biological membranes could be observed (Atanasov et al. [2005], Köper et al. [2005]) with the planar FETs, as they permit a smooth linkage of a membrane to the surface. The buried-channel devices could be used to operate at very low gate-source voltages as platform for alternative gate oxides based on organic material for novel biosensor chips (Sudhölter et al. [1990], de Smet et al. [2003], Faber et al. [2005], Faber et al. [2007]).

Appendix A

Device processing

A.1 Process flow

Table A.1 names the used wafer types and their properties, whereas Table A.2 lists all process parameters of the first and second run of the process, respectively. The two processes are distinguished where necessary. The buried-channel process parameteres are given in Tabel A.3. All equipment is given in Table A.6, the used chemicals are listed in Table A.5.

First process	
Company	Wacker Siltronic AG
Diameter	100mm
Thickness	500-550 μm
Orientation	<100>
Dopant	n / phosphorus
Resistivity	$2.5 - 8.5 \Omega cm$
Second process	
Company	Si-Mat
Diameter	100mm
Thickness	500-550 μm
Orientation	<100>
Dopant	n / phosphorus
Resistivity	$1 - 10 \Omega cm$

Table A.1: Wafers used for the fabrication processes.

Table A.2: Process steps and parameters for the planar open-gate p-FET.

No	Process step	Process parameters	Control
1	Oxidation	thermal, 30 nm	
	First process	wet oxide 900°C, 10 min	43 nm (Ellipsometry)
	Second process	dry oxide 900°C, 30 min	30 nm (Ellipsometry)
2	Nitride deposition	100 nm, LPCVD	
	First process		63 nm (Ellipsometry)
	Second process		100 nm (Ellipsometry)
3	1. Lithography: Definition of feed lines	pretreat: HMDS, 90°C/1min spin coat: AZ5214, 4000 rpm, 90°C/5min (soft bake) exposure: 365 nm, 4.3 s, 0.7 mW/cm^2 development: MIF326, 50 s	
	Hard bake	120°C/30 min	light microscope
4	Nitride/Oxide etch	RIE: CHF_3, 20 ml/min, 0.02 bar, 200 W	laser interferometer SOFIE
	First process	2 min 20 s	
	Second process	2 min 25 s	
5	Implantation	Boron: 120 keV, $8 \cdot 10^{15}/cm^2$ and 80 keV, $5 \cdot 10^{15}/cm^2$	
6	Resist removal	RIE: O_2, 30 ml/min, 0.03 bar, 200 W	

Table A.2: Process steps and parameters for the planar open-gate p-FET.

No	Process step	Process parameters	Control
	First process	16 min	
	Second process	13 min 30 s	SOFIE
7	2. Lithography: Definition of gateplateau	pretreat: HMDS, evaporated, 100°C spin coat: UV06, 4000 rpm, 130°C/60 s (soft bake) exposure: 248 nm, 6 s, 0.3 mW/cm^2 postexposure bake: 140°C/90 s development: MF24-A, 45 s	light microscope
8	Nitride/Oxide etching	RIE: CHF_3, 20 ml/min, 0.02 bar, 200 W	
	First process	4 min	
	Second process	6 min 40 s	SOFIE
	Resist removal	RIE: O_2, 30 ml/min, 0.03 bar, 200 W	
	First process	2 min 50 s	
	Second process	2 min 20 s	SOFIE
9	RCA clean, 2 HF-dips		
10	Diffusion and Oxidation		
	First process	1000°C 12 h 30 min O_2	

Table A.2: Process steps and parameters for the planar open-gate p-FET.

No	Process step	Process parameters	Control
		1 h 30 min N_2	Testwafer: Oxide thickness 300 nm (Ellipsometetry)
	Second process	1000°C 12 h 30 min O_2 1 h 30 min N_2	Testwafer: Oxide thickness 264 nm (Ellipsometetry)
11	Planarization, HF- etch to lower nitride edge, HF 1%		
	First process	W2: 10 min W1/3/5/6: 7 min	AFM: plateau height 60-70 nm; Thickness SiO_2 on feed line: 220 nm (Ellipsometry)
	Second process	W5: 18 min W1: 14 min W2/3/4/6: 13 min	Step from feed line to plateau: 105 nm (W5) 74 nm (W1) 77 nm (W2,3,4,6) (Dektak) Thickness SiO_2 on feed line: 196 nm (Ellipsometry)
12	Nitride etch	boiling H_3PO_4, 145°C	
	First process	45 min	AFM: step from feed line to plateau 30 nm; Thickness SiO_2 in gate area: 37 nm (Ellipsometry)
	Second process	W1/5: 1 h 20 min	

Table A.2: Process steps and parameters for the planar open-gate p-FET.

No	Process step	Process parameters	Control
		W2/3/4/6: 1 h 23 min	Step from feed line to plateau: 22 nm(W5) 6 nm(W1) 4 nm(W2) (Dektak)
13	Oxide etch	HF 1%	
	First process	3 min	Oxide thickness (sacrificial oxide) 13 nm in gate area (Ellipsometry)
	Second process	4 min	Oxide thickness (sacrificial oxide) 6 nm in gate area (Ellipsometry)
14	3. Lithography: Definition of gate geometry		
	First process	pretreat: HMDS, 90°C/1 min spin coat: AZ5214, 4000 rpm, 90°C/5 min (soft bake) exposure: 365 nm, 4.3 s, 0.7mW/cm^2 postexposure bake: 115°C/90 s flood exposure: 17.2 s development: MIF326, 45 s	light microscope

Table A.2: Process steps and parameters for the planar open-gate p-FET.

No	Process step	Process parameters	Control
	Second process	pretreat: HMDS, 90°C/1 min spin coat: AZ5214, 4000 rpm, 90°C/5 min (soft bake) exposure: 320 nm, 30 s development: MIF326, 45 s	light microscope
	Hard bake	150°C/30 min	
15	Implantation	Boron: 80 keV, $5\,10^{15}/cm^2$	
16	Resist removal	RIE: O_2, 20 ml/min, 0.02 bar, 200 W	
	First process	10 min	SOFIE
	Second process	14 min 15 s	SOFIE
17	RCA clean, 2 HF-dips		
18	Diffusion	O_2	
	First process	W6: 1000°C, 1 h W2: 1000°C, 30 min W5: 900°C, 30 min	probestation transistor channel closed by diffusing ions transistor channel closed by diffusing ions working transistors
	Second process	30 min 900°C	Testwafer: oxide thickness in gate area 13nm (Ellipsometetry)

Table A.2: Process steps and parameters for the planar open-gate p-FET.

No	Process step	Process parameters	Control
19	RCA clean, 2 HF-dips		
	First process	first HF-dip: 7 min	
	Second process	first HF-dip: 4 min 15 s	
20	Gateoxidation	O_2, 820°C, 1 h	
21	4. Lithography: Definition of contact holes	pretreat: HMDS, 90°C/1 min spin coat: AZ5214, 4000 rpm, 90°C/5 min (soft bake) exposure: 365 nm, 4.3 s, mW/cm^2 development: MIF326, 45 s	light microscope
22	Oxide etch	AF91 (buffered HF 10%) 5 min 30 s	
	Resist removal	Acetone (ultrasound 20s), Isopropanol	
23	5. Lithography: Definition of metal feed lines	pretreat: HMDS, 90°C/1 min spin coat: AZ5214, 4000 rpm, 90°C/5 min (soft bake) exposure: 365 nm, 4.3 s, mW/cm^2	light microscope

Table A.2: Process steps and parameters for the planar open-gate p-FET.

No	Process step	Process parameters	Control
		postexposure bake: 115°C/90 s flood exposure: 17.2 s development: MIF326, 45 s	
24	Metalization	Argon-sputtering 1 min/300 W Al/Ti/Au 150 nm/10 nm/150 nm	
25	Lift-Off	Acetone, Isopropanol	
26	Metal anneal	RTA: N_2, 325°C, 10 min	

Table A.3: Process parameters and aperatures for the planar buried-channel open-gate FET.

No	Process step	Process parameters	Control
1-18	see planar p-FET	see second process parameters	
19	Protection resist W5 cut into probes of 9 chips	AZ5214, 115°C/20 min	
	Resist removal	Acetone, Isopropanol	
20	4. Lithography: buried channel area	pretreat: HMDS, 90°C/1 min spin coat: AZ5214, 4000 rpm, 90°C/5 min (soft bake) exposure: 365 nm, 4.3 s postexposure bake: 115°C/90 s flood exposure: 17.2 s development: MIF326, 45 s	light microscope
21	Implantation	Boron: $5 \cdot 10^{15}/cm^2$ 5 keV (samples 4.1/5.1) 10 keV (samples 4.2/5.2) 15 keV (samples 4.3/5.3) 20 keV (samples 4.4/5.4)	
22	Resist removal	RIE: O_2, 20 ml/min, 0.02 bar, 200 W	
23	RCA clean, 2 HF-dips	1. HF-dip 2 min	
24	Anneal	RTA: 1000°C, N_2, 30 s	

Table A.3: Process parameters and aperatures for the planar buried-channel open-gate FET.

No	Process step	Process parameters	Control
25	Gateoxidation	O_2, 820°C, 1 h	
26	5. Lithography: Definition of contact holes	pretreat: HMDS, 90°C/1 min spin coat: AZ5214, 4000 rpm, 90°C/5 min (soft bake) exposure: 365 nm, 4.3 s development: MIF326, 45 s	light microscope
27	Oxide etch	AF91 (buffered HF 10%) 6 min	light microscope
	Resist removal	Acetone, Isopropanol	samples 4.4, 5.1, 5.2, 5.3 o.k. samples 4.1, 4.2, 4.3, 5.4 not etched in the middle
	27 repeated for samples 4.1, 4.2, 4.3, 5.4	AF91: 3 min	light microscope
28	6. Lithography: Definition of metal feed lines	pretreat: HMDS, 90°C/1 min spin coat: AZ5214, 4000 rpm, 90°C/5 min (soft bake) exposure: 365 nm, 4.3 s	light microscope

Table A.3: Process parameters and aperatures for the planar buried-channel open-gate FET.

No	Process step	Process parameters	Control
		postexposure bake: 115°C/90 s flood exposure: 17.2 s development: MIF326, 45 s	
29	Metalization	Argon-sputtering 1 min/300 W Al/Ti/Au 150 nm/10 nm/150 nm	
30	Lift-Off	Acetone, Isopropanol	light microscope
31	Metal anneal	RTA: N_2, 325°C, 10 min	

A.2 RCA cleaning procedure

To minimize contamination during the whole process, the wafers were cleaned with the RCA procedure, which is the industry standard for removing contaminants from wafers. It was developed by Werner Kern in 1965, while working for the Radio Corporation of America (RCA). The cleaning consists of several steps given in Table A.4, subsequently removing organic contaminants, a thin oxide layer, ionic and heavy metallic atomic contaminants.

Process step	Composition	Temperature and Time
Piranha Solution	$H_2O_2 : H_2SO_4 = 2 : 1$	60°C, 10min
HF-dip	1% (v/v) HF	room temperature, 10s
SC1, organic clean	$H_2O : H_2O_2 : NH_4OH = 20 : 4 : 1$	60°C, 10min
HF-dip	1% (v/v) HF	room temperature, 10s
SC2, ionic clean	$H_2O : H_2O_2 : HCl = 20 : 1 : 1$	60°C, 10min

Table A.4: Details of RCA cleaning procedure.

A.3 Equipment and chemicals

Reagent	Company
Acetone	Honeywell Riedel-de Haën, Seelze, Ger.
AF91	Honeywell Riedel-de Haën, Seelze, Ger.
AZ5214 resist	MicroChemicals, Ulm, Ger.
HMDS	Honeywell Riedel-de Haën, Seelze, Ger.
NH_4OH	Baker, Griesheim, Ger.
H_2O_2, HCl, $HF(37\%)$, H_3PO_4, H_2SO_4	Honeywell Riedel-de Haën, Seelze, Ger.
Isopropanol	Honeywell Riedel-de Haën, Seelze, Ger.
MF24-A	Micro resist technology, Berlin, Ger.
MIF326	MicroChemicals, Ulm, Ger.
UV06 resist	Micro resist technology, Berlin, Ger.

Table A.5: Chemicals used within the chip processing.

Equipment	**Company**	**Process Steps**
Atomic force microscope AFM	Zeiss/Axiotech SIS	6,12,16,21
High vaccum deposition plant	Pfeiffer Vacuum Inc.	25
Laser Ellipsometer S400	Sentech, Berlin, Ger.	1,2,10,12,13,18
Broadband Ellipsometer S800	Sentech, Berlin, Ger.	1,2,10,12,13,18
Ion implanter NV 8250	Axcelis Technologies, Beverly, MA	5,15
Light optical microscope Leitz	Leica Microsystems	3,7,14,21,23
LPCVD	Centrotherm, Blaubeuren, Ger.	2
Mask Aligner MA-6 365 nm	Suess MicroTech, Garching, Ger.	3,14,22,24
Mask Aligner MA-6 320 nm	Suess MicroTech, Garching, Ger.	14
Mask Aligner MA-6 248 nm	Suess MicroTech, Garching, Ger.	7
Oxidation oven	Tempress Sytems, Heerde, NL	1,10,18,21
RIE	Oxford,UK	4,6,8,16
RTA oven	Addax	26
Surface Profiler Dektak 3030	Veeco Instruments GmbH, Mannheim, Ger.	6,8,10,11,12

Table A.6: Equipment used within the chip processing.

Appendix B

Chip preparation

B.1 Flip-chip method, wire bonding and encapsulation

The chips for all cell measurements were assembled by the flip chip method, also called Controlled Collapsed Chip Connection (C4), which was first introduced by IBM in 1964. The chips were mounted onto the carriers in a face-down manner (hence the name flip chip) and the electrical connections were established by silver bumps on the chips' bond pads (Figure B.1). To apply

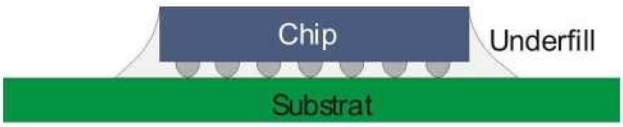

Figure B.1: Schematic of a face-down chip connected to a carrier by conductive silver bumps surrounded by underfilling Epoxy glue (Maier [2006]).

well defined silver glue bumps on the respecting contacts of the carrier, a laser perforated foil was used like in screen printing. The carrier was exactly placed below the holes in the foil and two-component silver glue was pressed through them with a quick but steady motion. Chips and carriers were then aligned and connected with a fineplacer as described by Ingebrandt et al. [2003] (Figure B.2). The silver glue was hardened at 150°C for 20 minutes. To guarantee the frequent reuse of the chips and to avoid short circuits, the conducting silver bumps were isolated by an epoxy underfill, which was applied around the die with a toothpick and drawn in the cleft between the bumps by capillary forces. A *polydimethylsiloxane* (PDMS) layer was applied around the die and hardened at 150°C for 1 h to protect the underfill during chip cleaning with ethanol. The encapsulation method forming a cell culture dish on top of the carrier was adapted from Offenhäusser et al. [1997] with some modifications. A glass ring with a diameter of 16 mm and a

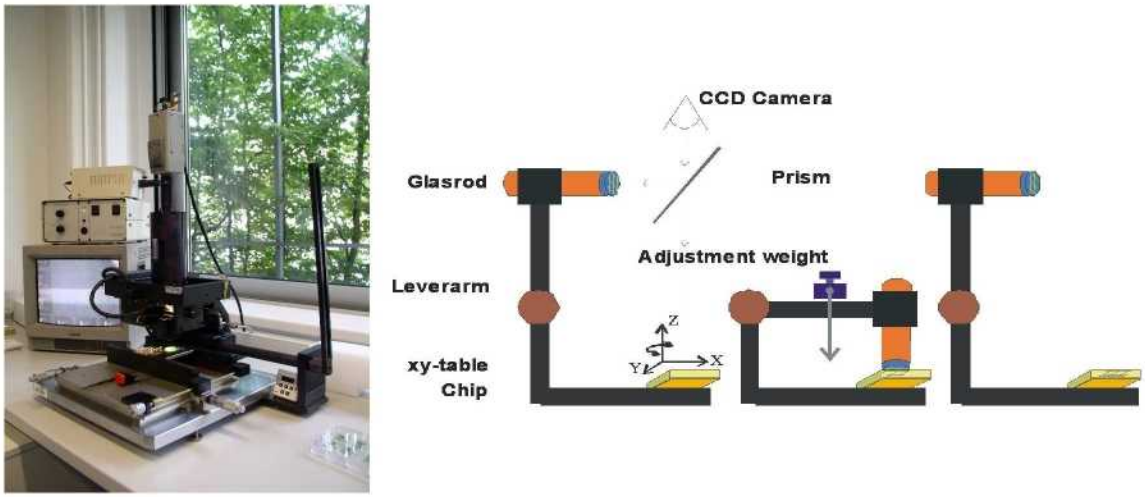

Figure B.2: A fineplacer was used to align and connect carrier and chip. Alignment was accomplished with a split field optic and the chip being mounted on a adjustable x-y-table.

smaller PDMS funnel (inner diameter 2,8 mm) were glued to the carrier with silicon glue, forming a cone-shaped hole. After degassing the silicon glue in vacuum, it was hardenend at 150°C for 1 h. The interspace between funnel and ring was subsequently filled with PDMS. Again, it was degassed before being hardened at 150°C for 1 h. This assembly formed a small petri dish for cell culturing for a couple of days (Figure B.3). The dish could hold 0.5 ml cell culture medium.

For noise measurements with our headstage (Meyburg [2005]), the chips needed to be encapsu-

Figure B.3: The single components (A) were assembled to a chip holding a small petri dish on top (B).

lated in a different way. They were glued onto 28-pin dual-inline carriers (DIL) with a tiny dot of silver glue. The contacts were established by wire bonds (Figure B.4 (A)) and the mounting of the petri dish on top was completed as described above (Figure B.4 (B)). All used reagents and equipment are listed in Table B.1.

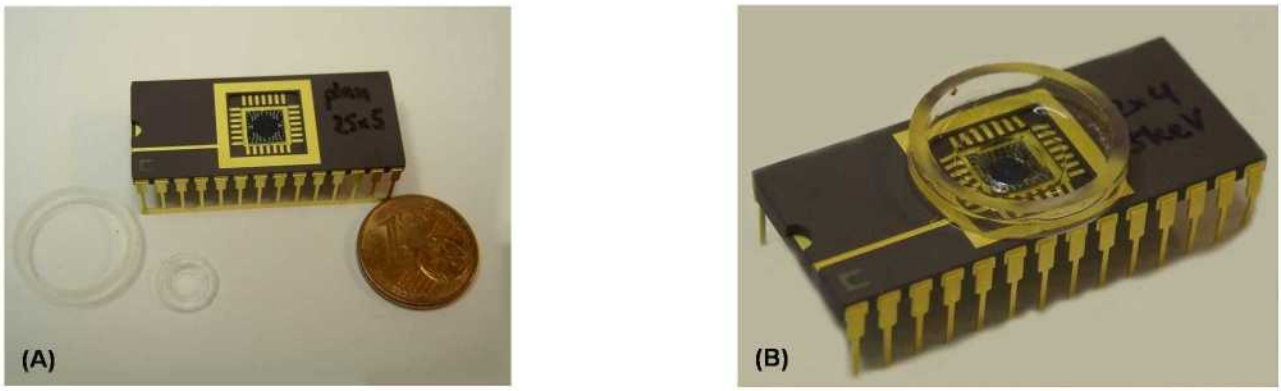

Figure B.4: The chip was contacted by wire bonds (A), funnel and glass ring were mounted to form a petri dish on top (B).

Reagent	Company
Epo-Tek H20E-PFC, Part A/B	Polytec GmbH, Waldbronn, Ger.
Silicone adhesive Sylgard 96-083, Base and Cure	Dow Corning, Midland, USA
Silicone elastomer Sylgard 184, Base and Cure	Dow Corning, Midland, USA
U300 Epoxy, Part A and B	Polytec GmbH, Waldbronn, Ger.
Equipment	**Company**
Bonder, semiautomatic, 4523AD	Kulicke &Soffa, Fort Washington,PA
Fineplacer	Finetech GmbH Co KG, Berlin, Ger.
Printed circuit board carrier (PBC)	Wika GmbH, Klingenberg, Ger.
Perforated Foil	CADiLAC Laser GmbH Co KG, Hilpoltstein, Ger.
Screenprinter SP-002	Essemtec AG, Aesch, Switzerland

Table B.1: Reagents and equipment used for the chip assembly.

B.2 Cleaning and coating

Before each measurement the chips were cleaned and the chip surface was activated in order to bind an adhesion promoting protein layer. The cleaning method was adapted from Offenhäusser et al. [1997]. The chips were cleaned in a Hellmanex bath in ultrasound for 5 minutes, followed by a rinse in VE-water (fully deionized water). Afterwards, they were transferred immediately to a bidest bath, undergoing another 5 minutes ultrasonification. For surface activation, H_2SO_4 was pipetted onto the chip surface and left for 20 minutes at 80°C. Once again the chips were cleaned in bidest with ultrasound for 5 minutes. The chips were dried with nitrogen to avoid corrosion of the bottom contacts. To keep the surfaces sterile until protein coating, they were covered with ethanol and transferred to the clean bench. Ethanol was removed and the chip surfaces were wasched twice with PBS. As cell adhesive protein we used *poly(L)lysin* (PLL) for HEK EAG cells, ghosts and vesicles, and fibronectin for fibroblasts. PLL acts cell adhesive due to its positive charges, while fibronectin contains certain functional amino acid sequences for

promoting cell adhesion. PLL was dissolved in bidest (100 μg/ml) and 25 μl were placed in the center of the cone-shaped opening. In case of fibronectin a concentration of 12.5 $\mu g/ml$ was used. After one hour of incubation, the surface was rinsed twice with PBS. Coated and dried chips could be stored at 4°C for several days before use. Directly after use, the chip surface was rubbed thouroughly with a Q-tip soaked with ethanol (70%) and rinsed with *bidestilled water* (bidest).

Appendix C

Cell culture

The following sections describe the used cell systems including their origin, their preparation and the cell culture procedures.

C.1 Human Embryonic Kidney 293 cells

The HEK cell line was generated from human embryonic kidney cells by transformation with a sheared adenovirus 5 DNA (Graham et al. [1977]). It is widely used in cell research, as HEK cells are easy to work with. One useful property is the low amount of ion channels creating low endogenous ionic current densities. Especially the density of potassium channels is relatively low (Zhu et al. [1998]).

The cell culture protocol was adapted from Wrobel et al. [2005]. Cells were grown in a 50 mm culture dish until they formed a 70 % confluent cell layer. For splitting the cells, they were trypsinized with 0.5 mg/ml trypsin for 5 min at 37°C. The detached cells were resuspended in M10 (Table C.1) and centrifuged for 5 min at 200 x g at room temperature. The pellet was resuspended again in 1 ml of M10 and the cell density was determined from a dilution with PBS (1:10) with a counting chamber. 30 000 cells in 3 ml M10 were seeded to a new culture dish. By addition of the antibiotic G418 (1 μl/ml M10) all non-transfected cells were sorted out, while the transfected cells were resistent against G418. Cells were cultured at 37°C and 5% CO_2.

The cells for measurement were plated onto the transistor chips in numbers of 1 500 to 2 500, suspended in 25 μl of M10. The number of plated cells was dependent on the number of days between plating and measurement, thus reaching a final number of 8 000 cells per chip. After an adhesion time of at least 3 hours, the chip was filled with 475 μl of M10. The plated cells

were cultured at 37°C, 5% CO_2 in a humidified chamber for 2 to 3 days. Immediately before conducting the measurement, the culture medium was exchanged to extracellular patch solution at 37°C.

M10 all culture medium

Reagent	Concentration
Glutamin	2mM
Non-essential amino acids	1%(v/v)
Fetal calf serum	10%(v/v)
Penicillin	100 units/ml
Streptomycin	0.1 ng/ml

Table C.1: Cell culture medium for HEK293 cells consisted of minimal medium with the listed additional ingredients.

Extracellular Solution

Reagent	Concentration
NaCl	140mM
KCl	5mM
Glucose	5mM
HEPES	10mM

Table C.2: Ingridients of the Ca^{+}-free extracellular patch solution at pH 7.4.

Reagent	Concentration
NaCl	137mM
KCl	2.7 mM
Na_2HPO_4	8.1mM
KH_2PO_4	1.47mM

Table C.3: Phosphate Buffered Saline PBS at pH 7.4.

All reagents were solved in H_2O (bidest) and adjusted to a pH of 7.3.

Solution for apoptosis

Reagent	Concentration
Annexin-V binding buffer	1 ml
Annexin-V FITC labelled	50 mul
Propidium iodide buffer (50 μg/ml in PBS)	
Irinotecan hydrochloride CPT-11 0.5 mg/ml	6 μl

Table C.4: Components of the apoptosis solution including apoptosis markers and apoptosis inducer.

C.2 Preparation of vesicles

The method of liposome swelling for vesicle preparation was first established by Dimitrov and Angelova (Angelova and Dimitrov [1985], Dimitrov et al. [1984]) and subsequently improved to liposome electroformation (Angelova and Dimitrov [1986], Angelova and Dimitrov [1987], Dimitrov and Angelova [1988]). Lipids of varying composition were deposited on metal electrodes (e.g. platinum electrodes) and dried under nitrogen atmosphere. Water was added and an DC voltage was applied. Driven by osmotic and electrostatic forces the lipids formed liposomes. Theoretical considerations, also regarding the preparation parameters, can be found at Dimitrov and Angelova [1986].

Here, the vesicles were prepared by the electroswelling technique. 2 μl of the lipid mixture (SOPC/ SOPS/ DMPE-LisRhod=500:2:1) were carefully deposited on indium tin oxide (ITO) coated glass slides. The lipid-chloroform film was dried under vacuum for 1 hour. After careful dehydration, the glass slides were arranged in a capacitor-like manner in a chamber containing 2 ml of 300 mM of sucrose solution. The slides were separated with a 1 mm teflon spacer and connected to copper electrodes. For electroswelling an AC field of 2 V was applied with 10 Hz for 3 hours. After preparation the vesicles were carefully transfered into PBS buffer (pH 7.4) containing 300 mM glucose. The vesicles were measured within a few hours after preparation. All lipids were purchased from Avanti Polar Lipids Inc.

Lipids
1-Stearoyl-2-Oleoyl-sn-Glycero-3-Phosphocholine (SOPC)
1-Stearoyl-2-Oleoyl-sn-Glycero-3-[Phospho-L-Serine] (SOPS)
1,2-Dimyristoyl-sn-Glycero-3-Phosphoethanolamine-N-LissamineRhodamine-B-Sylfonyl (DMPE-LisRhod)

Table C.5: Lipids used for vesicle preparation.

Solution	Component	Concentration
Phosphat buffered solution	$NaCl$	150 mM
	Na_3PO_4	5 mM
5p8 solution	Na_3PO_4	5 mM
5p8-Mg solution	$MgSO_4$	1 mM
	Na_3PO_4	5 mM
ISP7.4 solution	5p8	100g
	Sucrose	9g

Table C.6: Solutions for the preparation of erythrocyte ghosts.

C.3 Preparation of erythrocyte ghosts

Erythrocyte-ghosts can be preparated by electroporation, dialysis or direct hypotonic lysis of red blood cells, the latter being the easiest and mostly used method (Steck and Kant [1974]). The erythrocyte-membrane was prepared by ultracentrifugation in a lysis buffer. The subsequent transfer to an isotonic buffer led to the resealing of the membrane, producing the "resealed" ghosts. The ghosts' content can be varied and adjusted to the particular problem.

In our case the protocol was adopted from Lisin et al. [1996] and adjusted to lower centrifugation temperatures and higher accelerations. For the preparation 25 ml of fresh human blood were used. Heparin was added to prevent coagulation. The blood was removed from the withdrawal syringes and transfered to falcon tubes. The first centrifugation step (4°C, 2300 x g, 10 min) separated blood serum from all cellular components, which sedimented as a pellet. The supernatant was removed and the pellet dissolved in PBS by careful pipetting. The tubes were filled up to 12 ml with PBS for the next centrifugation. This was repeated three times, until the supernatant was clear. Hemolysis of the cells was initiated by dissolving the pellet in icecold hypotonic buffer (5P8). The membranous ghosts were transfered to sterile ultracentrifuge tubes and pelleted at 4°C with 22 000 x g for 15 min. Afterwards the supernatant was removed and the ghosts were washed twice in ice cold 5p8-Mg (4°C, 22 000 x g, 15 min), which caused them immediately to seal. The resealed ghosts were washed twice in ISP7.4 and resuspended in 4 ml of the same solution. Antibiotic was added (1.5 μl/ml solution) and the ghost density was controlled optically. The ghost solution was diluted 1:100 and 1:1000 with ISP7.4 and stored overnight at 4°C. All solutions are given in Table C.6. The pH value of PBS, the 5p8 buffer and the 5p8-Mg buffer were set to 8.0, ISP7.4 was adjusted to a PH of 7.4.

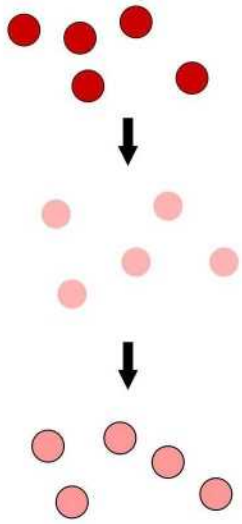

Figure C.1: Ghost preparation: Red blood cells undergo lysis and are resealed again

C.4 Fibroblasts

Component	Concentration
Basic fibroblast growth factor, human, recombinant	1.0 ng/ml medium
Endothelial cell growth supplement/ Heparin	4 μl/ml medium
Epidermial growth factor, human, recombinant	1.0 ng/ml medium
Hydrocortisone	1 μg/ml medium
Phenol red	0.62ng/ml medium
Fetal calf serum	20 μl/ml medium

Table C.7: Endothelial cell growth medium containing the delivered supplement mix.

Appendix D

General chemicals, software and equipment

D.1 Reagents

Reagent	Company
2-Propanol	Merck KGaA, Darmstadt, Ger.
Ag wire	Goodfellow, Bad Nauheim, Ger.
Amphotericin B	Sigma-Aldrich Chemie GmbH, Taufkirchen, Ger.
Aceton p.A	Merck KGaA, Darmstadt, Ger.
Antibiotikum G418	Invitrogen GmbH, Karlsruhe, Ger.
Epidermal growth factor	Sigma-Aldrich Chemie GmbH, Taufkirchen, Ger.
Endothelial growth medium	Promocell, Heidelber, Ger.
Ethanol	Riedel-de Haën, Seelze, Ger.
Fetal calf serum	Invitrogen GmbH, Karlsruhe, Ger.
HBSS	Sigma-Aldrich Chemie GmbH, Taufkirchen, Ger.
HELLMANEX II	Hellma GmbH, Mühlheim, Ger.
Minimal Essential Medium	Sigma-Aldrich Chemie GmbH, Taufkirchen, Ger.
Non-essential amino acids	Invitrogen GmbH, Karlsruhe, Ger.
Irinotecan hydrochloride (CPT-11)	Sigma-Aldrich Chemie GmbH, Taufkirchen, Ger.
Penicillin-Streptomycin	Sigma-Aldrich Chemie GmbH, Taufkirchen, Ger.
Poly-L-Lysin	Sigma-Aldrich Chemie GmbH, Taufkirchen, Ger.
Trypsin EDTA	Sigma-Aldrich Chemie GmbH, Taufkirchen, Ger.

Table D.1: Used reagents

D.2 Software

Software	Company
AutoCad	
BioMol	D.Lomparski, Research Centre Jülich
MathWorks MATLAB 7.0	The MathWorks, Inc.,Natick,Boston,USA
OriginLab Origin 7.5	OriginLab Corporation, Northampton MA, USA
PSpice	Orcad Cadence Design Systems, San Jose, CA
SA3Cell	S.Meyburg, Research Centre Juelich

Table D.2: Software

D.3 Equipment

Equipment	Company
Light mikroscope Axiotech Vario with camera	Carl Zeiss AG, Oberkochen, Ger.
DIC-Prisma und Schieber	Carl Zeiss AG, Oberkochen, Ger.
Lock-In-Amplifier	N.Wolters, Research Centre Jülich
Osmometer Osmomat 030	Gonotec GmbH, Berlin, Ger.
Semiconductor probe system PM5	Suess MicroTech, Garching, Ger.
TTF-Box	N.Wolters, Research Centre Jülich

Table D.3: Technical equipment

Bibliography

Adam, P.Läuger, and G. Stark. *Physikalische Chemie und Biophysik*. Springer Verlag, Berlin,2nd edition, 1988.

B. Alberts, A. Johnson, J. Lewis, M. Raff, K. Roberts, and P. Walter. *Molekularbiologie der Zelle, 4. Auflage ISBN 3-527-30492-4*. Wiley-VCH Verlag GmbH & Co. KgaA, Weinheim, 2004.

D. Ammann, E. Pretsch, W. Simon, E. Lindner, A. Bezegh, and E. Pungor. Lipophilic salts as membrane additives and their influence on the properties of macroelectrodes and microelectrodes based on neutral carriers. *Analytica Chimica Acta*, 171(MAY):119–129, 1985.

M. I. Angelova and D. S. Dimitrov. Kinetics of cell-size liposome formation. *Biophysical Journal*, 47(2):A163–A163, 1985.

M. I. Angelova and D. S. Dimitrov. Liposome electroformation. *Faraday Discussions*, pages 303–+, 1986.

M. I. Angelova and D. S. Dimitrov. Swelling of charged lipids and formation of liposomes on electrode surfaces. *Molecular Crystals And Liquid Crystals*, 152:89–104, 1987.

M. M. Antonisse, B. H. Snellink-Ruël, R. J. Lugtenberg, J. F. Engbersen, A. van den Berg, and D. N. Reinhoudt. Membrane characterization of anion-selective chemfets by impedance spectroscopy. *Anal Chem*, 72(2):343–348, Jan 2000.

R. D. Armstrong and M. Todd. Exchange of li+, na+ and k+ ions with a pvc membrane containing valinomycin and kbph4. *Electrochimica Acta*, 31(11):1413–1415, Nov. 1986.

M. Arnold, E. A. Cavalcanti-Adam, R. Glass, J. Blümmel, W. Eck, M. Kantlehner, H. Kessler, and J. P. Spatz. Activation of integrin function by nanopatterned adhesive inter-

faces. *Chemphyschem*, 5(3):383–388, Mar 2004. URL http://dx.doi.org/10.1002/cphc.200301014.

V. Atanasov, N. Knorr, R. S. Duran, S. Ingebrandt, A. Offenhäusser, W. Knoll, and I. Köper. Membrane on a chip: A functional tethered lipid bilayer membrane on silicon oxide surfaces. *Biophysical Journal*, 89(3):1780–1788, Sept. 2005.

J. P. Aubry, A. Blaecke, S. Lecoanet-Henchoz, P. Jeannin, N. Herbault, G. Caron, V. Moine, and J. Y. Bonnefoy. Annexin v used for measuring apoptosis in the early events of cellular cytotoxicity. *Cytometry*, 37(3):197–204, Nov 1999.

D. Axelrod. Cell-substrate contacts illuminated by total internal-reflection fluorescence. *Biophysical Journal*, 33(2):A200–A200, 1981.

M. A. Barry, J. E. Reynolds, and A. Eastman. Etoposide-induced apoptosis in human hl-60 cells is associated with intracellular acidification. *Cancer Research*, 53(10):2349–2357, May 1993.

e. a. Bekkers. *The Axon CNS guide to electrophysiology and biophysics laboratory techniques.* Axon CNS Molecular Devices, 2006.

P. Bergveld, J. Wiersma, and H. Meertens. Extracellular potential recordings by means of a field effect transitor without gate metal, called osfet. *IEEE Trans Biomed Eng*, 23(2):136–144, Mar 1976.

C. C. Berry, G. Campbell, A. Spadiccino, M. Robertson, and A. S. G. Curtis. The influence of microscale topography on fibroblast attachment and motility. *Biomaterials*, 25(26):5781–5788, Nov 2004. URL http://dx.doi.org/10.1016/j.biomaterials.2004.01.029.

D. Braun and P. Fromherz. Fluorescence interferometry of neuronal cell adhesion on microstructured silicon. *Physical Review Letters*, 81(23):5241–5244, Dec. 1998.

D. Braun and P. Fromherz. Imaging neuronal seal resistance on silicon chip using fluorescent voltage-sensitive dye. *Biophys J*, 87(2):1351–1359, Aug 2004. URL http://dx.doi.org/10.1529/biophysj.104.039990.

B. Brüne. Nitric oxide: No apoptosis or turning it on? *Cell Death Differ*, 10(8):864–869, Aug 2003. URL http://dx.doi.org/10.1038/sj.cdd.4401261.

C. S. Chen, M. Mrksich, S. Huang, G. M. Whitesides, and D. E. Ingber. Geometric control of cell life and death. *Science*, 276(5317):1425–1428, May 1997.

W. T. Chen. Induction of spreading during fibroblast movement. *J Cell Biol*, 81(3):684–691, Jun 1979.

K. S. Cole. Dynamic electrical characteristics of the squid axon membrane. *Archives Des Sciences Physiologiques*, 3(2):253–258, 1949.

J. A. Conti, N. E. Kemeny, L. B. Saltz, Y. Huang, W. P. Tong, T. C. Chou, M. Sun, S. Pulliam, and C. Gonzalez. Irinotecan is an active agent in untreated patients with metastatic colorectal cancer. *Journal Of Clinical Oncology*, 14(3):709–715, Mar. 1996.

A. Curtis and C. Wilkinson. Topographical control of cells. *Biomaterials*, 18(24):1573–1583, Dec 1997.

L. C. P. M. de Smet, G. A. Stork, G. H. F. Hurenkamp, Q.-Y. Sun, H. Topal, P. J. E. Vronen, A. B. Sieval, A. Wright, G. M. Visser, H. Zuilhof, and E. J. R. Sudhölter. Covalently attached saccharides on silicon surfaces. *J Am Chem Soc*, 125(46):13916–13917, Nov 2003. URL `http://dx.doi.org/10.1021/ja037445i`.

D. S. Dimitrov and M. I. Angelova. Swelling and electroswelling of lipids - theory and experiment. *Studia Biophysica*, 113(1-2):15–20, 1986.

D. S. Dimitrov and M. I. Angelova. Lipid swelling and liposome formation mediated by electric-fields. *Bioelectrochemistry And Bioenergetics*, 19(2):323–336, June 1988.

D. S. Dimitrov, J. LI, M. Angelova, and R. K. Jain. Surface effects in preparation of cell-size liposomes. *Febs Letters*, 176(2):398–400, 1984.

T. Dufaux. personal communications. 2007.

S. Eick. personal communications. 2007.

S. Engelhardt. Characterization of the cell-sensor contact with total internal reflection fluorescence microscopy. Diplomarbeit, Rheinisch-Westfälische Technische Hochschule Aachen, 2007.

J. F. Eschermann. personal communications. 2007.

E. J. Faber, L. C. P. M. de Smet, W. Olthuis, H. Zuilhof, E. J. R. Sudhölter, P. Bergveld, and A. van den Berg. Si-c linked organic monolayers on crystalline silicon surfaces as alternative gate insulators. *Chemphyschem*, 6(10):2153–2166, Oct 2005. URL `http://dx.doi.org/10.1002/cphc.200500120`.

E. J. Faber, W. Sparreboom, W. Groeneveld, L. C. P. M. de Smet, J. Bomer, W. Olthuis, H. Zuilhof, E. J. R. Sudhölter, P. Bergveld, and A. van den Berg. ph sensitivity of si–c linked organic monolayers on crystalline silicon surfaces. *Chemphyschem*, 8(1):101–112, Jan 2007. URL `http://dx.doi.org/10.1002/cphc.200600447`.

S. W. Fesik and Y. Shi. Structural biology. controlling the caspases. *Science*, 294(5546):1477–1478, Nov 2001. URL `http://dx.doi.org/236`.

S. Frings, N. Brüll, C. Dzeja, A. Angele, V. Hagen, U. B. Kaupp, and A. Baumann. Characterization of ether-à-go-go channels present in photoreceptors reveals similarity to ikx, a k+ current in rod inner segments. *J Gen Physiol*, 111(4):583–599, Apr 1998.

Fromherz, Müller, and Weis. Neuron transistor: Electrical transfer function measured by the patch-clamp technique. *Physical Review Letters*, 71(24):4079–4082, Dec 1993.

Fromherz and Stett. Silicon-neuron junction: Capacitive stimulation of an individual neuron on a silicon chip. *Physical Review Letters*, 75(8):1670–1673, Aug 1995.

P. Fromherz, V. Kiessling, K. Kottig, and G. Zeck. Membrane transistor with giant lipid vesicle touching a silicon chip. *Applied Physics A-Materials Science & Processing*, 69(5):571–576, Nov. 1999.

P. Gastrein. *NaKpompe-cycle.* Wikipedia, Sep 2005. URL `http://en.wikipedia.org/wiki/Sodium_potassium_pump`. Released under the GNU Free Documentation License.

P. Gehrig, W. E. Morf, M. Welti, E. Pretsch, and W. Simon. Catalysis of ion transfer by tetraphenylborates in neutral carrier-based ion-selective electrodes. *Helvetica Chimica Acta*, 73(1):203–212, 1990.

I. Giaever and C. R. Keese. Monitoring fibroblast behavior in tissue culture with an applied electric field. *Proc Natl Acad Sci U S A*, 81(12):3761–3764, Jun 1984.

I. Giaever and C. R. Keese. Micromotion of mammalian cells measured electrically. *Proc Natl Acad Sci U S A*, 88(17):7896–7900, Sep 1991.

R. Gleixner and P. Fromherz. The extracellular electrical resistivity in cell adhesion. *Biophys J*, 90(7):2600–2611, Apr 2006. URL `http://dx.doi.org/10.1529/biophysj.105.072587`.

R. A. Gottlieb, J. Nordberg, E. Skowronski, and B. M. Babior. Apoptosis induced in jurkat cells by several agents is preceded by intracellular acidification. *Proceedings Of The National Academy Of Sciences Of The United States Of America*, 93(2):654–658, Jan. 1996.

F. L. Graham, J. Smiley, W. C. Russell, and R. Nairn. Characteristics of a human cell line transformed by dna from human adenovirus type 5. *J Gen Virol*, 36(1):59–74, Jul 1977.

D. R. Green and J. C. Reed. Mitochondria and apoptosis. *Science*, 281(5381):1309–1312, Aug. 1998.

B. D. Harms, G. M. Bassi, A. R. Horwitz, and D. A. Lauffenburger. Directional persistence of egf-induced cell migration is associated with stabilization of lamellipodial protrusions. *Biophysical Journal*, 88(2):1479–1488, Feb. 2005.

M. Hoeller. Biophysikalische charakterisierung des zell-transistor kontaktes. Diplomarbeit, Rheinisch-Westfälische Technische Hochschule Aachen, 2005.

A. Huttenlocher, R. R. Sandborg, and A. F. Horwitz. Adhesion in cell migration. *Curr Opin Cell Biol*, 7(5):697–706, Oct 1995.

M. Hutzler and P. Fromherz. Silicon chip with capacitors and transistors for interfacing organotypic brain slice of rat hippocampus. *Eur J Neurosci*, 19(8):2231–2238, Apr 2004. URL `http://dx.doi.org/10.1111/j.0953-816X.2004.03311.x`.

S. Ingebrandt, C. K. Yeung, M. Krause, and A. Offenhäusser. Cardiomyocyte-transistor-hybrids for sensor application. *Biosens Bioelectron*, 16(7-8):565–570, Sep 2001.

S. Ingebrandt, C.-K. Yeung, M. Krause, and A. Offenhäusser. Neuron-transistor coupling: interpretation of individual extracellular recorded signals. *Eur Biophys J*, 34(2):144–154, Mar 2005. URL `http://dx.doi.org/10.1007/s00249-004-0437-9`.

S. Ingebrandt, C. K. Yeung, W. Staab, T. Zetterer, and A. Offenhäusser. Backside contacted field effect transistor array for extracellular signal recording. *Biosens Bioelectron*, 18(4):429–435, Apr 2003.

Y. Iwanaga, D. Braun, and P. Fromherz. No correlation of focal contacts and close adhesion by comparing gfp-vinculin and fluorescence interference of dil. *Eur Biophys J*, 30(1):17–26, 2001.

J. B. Johnson. Thermal agitation of electricity in conductors. *Physical Review*, 32(1):97–109, July 1928.

A. G. Jordan and N. A. Jordan. Theory of noise in metal oxide semiconductor devices. *Ieee Transactions On Electron Devices*, ED12(3):148–&, 1965.

D. R. Jung, R. Kapur, T. Adams, K. A. Giuliano, M. Mrksich, H. G. Craighead, and D. L. Taylor. Topographical and physicochemical modification of material surface to enable patterning of living cells. *Crit Rev Biotechnol*, 21(2):111–154, 2001.

D. Kahng and M. Atalla. Silicon- silicon dioxide field induced surface devices. Solid State Device Research. Conference, Pittsburgh,. Pa., 1960.

C. Keese and I. Giaever. A biosensor that monitors cell morphology with electrical fields. *Engineering in Medicine and Biology Magazine, IEEE*, 13(3):402–408, June-July 1994.

C. R. Keese and I. Giaever. Substrate mechanics and cell spreading. *Exp Cell Res*, 195(2): 528–532, Aug 1991.

C. R. Keese, N. Karra, B. Dillon, A. M. Goldberg, and I. Giaever. Cell-substratum interactions as a predictor of cytotoxicity. *In Vitro & Molecular Toxicology-A Journal Of Basic And Applied Research*, 11(2):183–192, 1998.

C. R. Keese, J. Wegener, S. R. Walker, and I. Giaever. Electrical wound-healing assay for cells in vitro. *Proc Natl Acad Sci U S A*, 101(6):1554–1559, Feb 2004. URL `http://dx.doi.org/10.1073/pnas.0307588100`.

W. Keese and G. Branner. In-depth modeling, analysis and design of balanced active microwave frequency doublers. In *Circuits and Systems, 1993., Proceedings of the 36th Midwest Symposium on*, pages 562–565vol.1, 16-18 Aug. 1993.

H. Kenis, H. van Genderen, A. Bennaghmouch, H. A. Rinia, P. Frederik, J. Narula, L. Hofstra, and C. P. M. Reutelingsperger. Cell surface-expressed phosphatidylserine and annexin a5 open a novel portal of cell entry. *J Biol Chem*, 279(50):52623–52629, Dec 2004. URL `http://dx.doi.org/10.1074/jbc.M409009200`.

A. B. Kharitonov, J. Wasserman, E. Katz, and I. Willner. The use of impedance spectroscopy for the characterization of protein-modified isfet devices: Application of the method for the analysis of biorecognition processes. *Journal Of Physical Chemistry B*, 105(19):4205–4213, May 2001a.

A. B. Kharitonov, M. Zayats, L. Alfonta, E. Katz, and I. Willner. A novel isfet-based nad(+)-dependent enzyme sensor for lactate. *Sensors And Actuators B-Chemical*, 76(1-3):203–210, June 2001b.

A. B. Kharitonov, M. Zayats, A. Lichtenstein, E. Katz, and I. Willner. Enzyme monolayer-functionalized field-effect transistors for biosensor applications. *Sensors And Actuators B-Chemical*, 70(1-3):222–231, Nov. 2000.

V. Kiessling, B. Müller, and P. Fromherz. Extracellular resistance in cell adhesion measured with a transistor probe. *Langmuir*, 16(7):3517–3521, Apr. 2000.

I. Köper, N. Knorr, V. Atanasov, J. R. Long, P. A. V. Anderson, R. Duran, and W. Knoll. Membrane on a chip; tethered bilayer membranes as a biosensor platform. *Abstracts Of Papers Of The American Chemical Society*, 229:U657–U657, Mar. 2005.

R. Lisin, B. Z. Ginzburg, M. Schlesinger, and Y. Feldman. Time domain dielectric spectroscopy study of human cells. i. erythrocytes and ghosts. *Biochim Biophys Acta*, 1280(1):34–40, Apr 1996.

C. M. Lo, C. R. Keese, and I. Giaever. Impedance analysis of mdck cells measured by electric cell-substrate impedance sensing. *Biophys J*, 69(6):2800–2807, Dec 1995.

M. Maier. *Schematic of C4*. Wikipedia, 2006.

S. Matsuyama, J. Llopis, Q. L. Deveraux, R. Y. Tsien, and J. C. Reed. Changes in intramitochondrial and cytosolic ph: early events that modulate caspase activation during apoptosis. *Nature Cell Biology*, 2(6):318–325, June 2000.

R. Merkel, N. Kirchgebner, C. M. Cesa, and B. Hoffmann. Cell force microscopy on elastic layers of finite thickness. *Biophysical Journal*, 93(9):3314–3323, Nov. 2007.

S. Meyburg. *Transistor Arrays for the Direct Interfacing with Electrogenic Cells*. PhD thesis, Rheinisch-Westf¨alische Technische Hochschule Aachen, 2005.

R. Müller. *Rauschen*. Springer Verlag, Berlin, München, New York, London, Paris, Tokyo, Hongkong, 1990.

R. Naumann, S. M. Schiller, F. Giess, B. Grohe, K. B. Hartman, I. Karcher, I. Koper, J. Lubben, K. Vasilev, and W. Knoll. Tethered lipid bilayers on ultraflat gold surfaces. *Langmuir*, 19(13): 5435–5443, June 2003.

E. Neher and B. Sakmann. Single-channel currents recorded from membrane of denervated frog muscle fibres. *Nature*, 260(5554):799–802, Apr 1976.

H. Nyquist. Thermal agitation of electric charge in conductors. *Physical Review*, 32(1):110–113, July 1928.

A. Offenhäusser, C. Sprössler, M. Matsuzawa, and W. Knoll. Field-effect transistor array for monitoring electrical activity from mammalian neurons in culture. *Biosens Bioelectron*, 12(8): 819–826, 1997.

S. Paukner, G. Kohl, K. Jalava, and W. Lubitz. Sealed bacterial ghosts–novel targeting vehicles for advanced drug delivery of water-soluble substances. *J Drug Target*, 11(3):151–161, Apr 2003. URL `http://dx.doi.org/10.1080/10611860310001593366`.

A. Rauf. Analysis of cell morphology in dependence of selected surface coating by means of confocal laser scanning microscopy. Master's thesis, FH Aachen, Campus Jülich, 2007.

J. Rädler and E. Sackmann. Imaging optical thicknesses and separation distances of phospholipid-vesicles at solid-surfaces. *Journal De Physique Ii*, 3(5):727–748, May 1993.

W. G. Regehr, J. Pine, C. S. Cohan, M. D. Mischke, and D. W. Tank. Sealing cultured invertebrate neurons to embedded dish electrodes facilitates long-term stimulation and recording. *J Neurosci Methods*, 30(2):91–106, Nov 1989.

M. Ruiz. *Cell membrane detailed diagram.svg*. Wikipedia, Jan 2007. URL `en.wikipedia.org/wiki/Cell_membrane`.

R. B. M. Schasfoort, G. J. Streekstra, P. Bergveld, R. P. H. Kooyman, and J. Greve. Influence of an immunological precipitate on dc and ac behavior of an isfet. *Sensors And Actuators*, 18 (2):119–129, June 1989.

S. J. Singer and G. L. Nicolson. The fluid mosaic model of the structure of cell membranes. *Science*, 175(23):720–731, Feb 1972.

T. L. Steck and J. A. Kant. Preparation of impermeable ghosts and inside-out vesicles from human erythrocyte membranes. *Methods Enzymol*, 31(Pt A):172–180, 1974.

E. J. R. Sudhölter, P. D. Vanderwal, M. Skowpronskaptasinska, A. Vanderberg, P. Bergveld, and D. N. Reinhoudt. Modification of isfets by covalent anchoring of poly(hydroxyethyl methacry-

late) hydrogel - introduction of a thermodynamically defined semiconductor-sensing membrane interface. *Analytica Chimica Acta*, 230(1):59–65, Mar. 1990.

D. Swartz. *Basic Histology, Cells and their structure, membrane elements.* 2007. URL `http://anatomy.iupui.edu/courses/histo_D502/D502f04/lecture.f04/cell.f0%4/cellf04`.

Szczepan. *Biological Cell.* Wikipedia, Oct 2006. URL `en.wikipedia.org/wiki/Biological_cell`. Multi-license with GFDL and Creative Commons CC-BY-SA-2.5 and older versions (2.0 and 1.0).

S. Sze. *Semiconductor devices-Physics and technology.* John Wiley & sons, 1985.

C. B. Thompson. Apoptosis in the pathogenesis and treatment of disease. *Science*, 267(5203): 1456–1462, Mar 1995.

F. Vassanelli. Neurons from rat brain coupled to transistors. *Applied Physics A-Materials Science & Processing*, 65:85–88, 1997.

M. Völker. *Detektion von Aktionspotentialen einzelner Säugetierneurone mit rauscharmen Feldeffekttransistoren nahe der thermodynamischen Meßgrenze.* PhD thesis, Technische Universität München, 2005.

S. G. Waley and J. Watson. The action of trypsin on polylysine. *Biochemical Journal*, 55(2): 328–&, 1953.

J. Wallys. Stimulation of individual electrogenic cells with micro-scale sirof electrodes. Diplomarbeit, Rheinisch-Westfälische Technische Hochschule Aachen, 2007.

J. Wegener, C. R. Keese, and I. Giaever. Electric cell-substrate impedance sensing (ecis) as a noninvasive means to monitor the kinetics of cell spreading to artificial surfaces. *Exp Cell Res*, 259(1):158–166, Aug 2000. URL `http://dx.doi.org/10.1006/excr.2000.4919`.

R. Weis, C. Müller, and P. Fromherz. Neuron adhesion on a silicon chip probed by an array of field-effect transistors. *Physical Review Letters*, 76(2):327–330, Jan 1996.

G. Wrobel, M. Höller, S. Ingebrandt, S. Dieluweit, F. Sommerhage, H. P. Bochem, and A. Offenhäusser. Transmission electron microscopy study of the cell-sensor interface. *J R Soc Interface*, 5(19):213–222, Apr 2008. URL `http://dx.doi.org/10.1098/rsif.2007.1094`.

G. Wrobel, R. Seifert, S. Ingebrandt, J. Enderlein, H. Ecken, A. Baumann, U. B. Kaupp, and A. Offenhäusser. Cell-transistor coupling: investigation of potassium currents recorded with p- and n-channel fets. *Biophys J*, 89(5):3628–3638, Nov 2005. URL `http://dx.doi.org/10.1529/biophysj.104.049809`.

G. Zeck and P. Fromherz. Repulsion and attraction by extracellular matrix protein in cell adhesion studied with nerve cells and lipid vesicles on silicon chips. *Langmuir*, 19(5):1580–1585, Mar. 2003.

G. Zhu, Y. Zhang, H. Xu, and C. Jiang. Identification of endogenous outward currents in the human embryonic kidney (hek 293) cell line. *J Neurosci Methods*, 81(1-2):73–83, Jun 1998.

Danke...

An dieser Stelle möchte ich mich bei allen bedanken, die zu dieser Arbeit beigetragen und mich in Höhen und Tiefen begleitet haben.

Danke Herr Prof. Dr. Andreas Offenhäusser, für die Aufnahme in Ihr Institut und die Möglichkeit das spannende Thema dieser Arbeit im Rahmen ihrer tollen, interdisziplinären Gruppe bearbeiten zu können. Insbesondere möchte ich mich für Ihren Einsatz bedanken, als sich eine notwendige Verlängerung meiner Arbeit abzeichnete.

Danke Herr Prof. Dr. Hao Tjeng, für die Bereitschaft Begutachter dieser Arbeit zu sein.

Danke Dr. Sven Ingebrandt, für die gute Betreuung und die vielen Anregungen und Ratschläge rund um diese Arbeit. Auch Dir besonderen Dank für den Rückhalt in den schwierigeren Phasen der Arbeit.

Danke Regina Stockmann, für die tolle Zusammenarbeit rund um den planar-FET Prozess. Du hast mir viel beigebracht und auch lange Reinraumstunden vergnüglich gemacht.

Danke Boris Hofmann, für die Unterstützung bei den Apoptose-Messungen, das Bonden der buried-channel FETs und die große Geduld während der Korrekturphase. Du hattest wirklich immer ein offenes Ohr, in allen Belangen.

Danke Stefan Eick, für die große Unterstützung bei den Rauschmessungen und die konstruktive Kritik während der Korrekturphase. Nicht zu vergessen die konstante Unterstützung bei allen kleineren und größeren alltäglichen Schwierigkeiten.

Danke Jan Eschermann, für die vielen fachlichen Diskussionen und privaten Gespräche. Du warst ein prima Büro-"Mitbewohner"! Insbesondere danke ich dir für die Unterstützung bei der Modellierung der Transfer Funktionen.

Danke Thomas Dufaux, für die Unterstützung bei der Modellierung der Transfer Funktionen.

Danke Dieter Lomparski, für die Bereitstellung der BioMol software und großer Geduld bei kurzfristigen "Sonderwünschen".

Danke Norbert Wolters, für die Unterstützung in elektronischen Belangen rund um die TTF-Messbox.

Danke Rita Helpenstein, Sabrina Buller und Esther Breuer für eure umfassende Unterstützung und Hilfe im Biolabor, sowie die Präparation der HEK293 Zellen.

Danke Günter Wrobel, für die Vorarbeit mit den Transfer-Funktions Messungen und die lehrreichen Diskussionen.

Danke Dr. Simone Meffert, für die Beantwortung zahlreicher biologischer Fragen und die Unterstützung bei der Präparation der Erythrocyten-Ghosts.

Danke Nils Hersch (IBN-4), für die gute Zusammenarbeit rund um die Fibroblasten-Migrationsexperimente.

Danke Dr. Agnes Csiszar (IBN-4), für die Präparation der Lipidvesikel.

Danke Alfred Steffen und seinem Reinraum-Team (ISG-PT), für die Unterstützung rund um alle Reinraumgeräte. Insbesondere danke ich J. Müller für die Hilfe mit den verschiedenen Belichtern und S. Bunte für das Sägen der Wafer.

Danke Katja Panitz und W. Michelsen (IBN-1) für die Implantationen und die Unterstützung bei der buried-channel FET Prozessierung.

Danke Petra Schulte, für die ausführliche Beantwortung biologischer Fragen.

Danke Sascha Engelhardt und Jens Wallys, meinen Mit-Diplomanden, für moralische Unterstützung und viele Gespräche.

Thank you Dr. Ranjita Gosh-Moulick, for various conversations and for being such a nice "roommate".

Danke allen anderen Kollegen des IBN-2, die hier nicht namentlich erwähnt wurden.

Danke meiner Familie, weil ihr immer ein Rückhalt für mich seid und nie aufhört Interesse an dem zu zeigen, was ich tue.

Danke meinen lieben Freunden, weil ihr alle großen und kleinen Katastrophen des letzten Jahres mit mir durchgestanden habt und mich bedingungslos (er)trugt, als ein Flügel gebrochen war.

Danke Flo, dafür dass du da bist.

Zusammenfassung

Ziel dieser Arbeit war die elektrische Charakterisierung der Adhäsion zellulärer Systeme auf nichtmetallisierten, p-dotierten Feldeffekt-Transistoren (open-gate p-FETs). Dazu wurden frequenz- und zeitabhängige Transfer-Funktions Messungen mit verschiedenen Zelltypen sowie mit verschiedenen biomimetischen Systemen durchgeführt. Alle Messungen waren auf der Ebene einzelner Zellen möglich. Feld-Effekt Transistoren des Jülicher Typs wurden für die Charakterisierung der Adhäsion von HEK293 Zellen eingesetzt. Für biomimetische Systeme wie künstliche Membranvesikel oder Erythrocyten-Ghosts wurden planare Feldeffekt-Transistoren entwickelt und prozessiert. Diese waren ebenfalls geeignet, um elektrische Messungen der Zellmigration von Fibroblasten durchzuführen.

Das Design der planaren FETs war an dem FET-Design des Jülicher Typs orientiert, jedoch im Hinblick auf die Leiterbahnkapazität optimiert. Zentrale Aufgabe war die Planarisierung der Chips ohne das aufwändige chemisch-mechanische Polieren. Dies wurde mit einer zusätzlichen Lithographie, einer LOCOS-Oxidation, sowie einem selektiven Ätzschritt erreicht. Das verbleibende LOCOS-Oxid diente als Passivierung der Leiterbahnen. Mit dieser Methode wurden Stufenhöhen von maximal 30 nm erreicht. Dadurch wurde die Topologie der Transistoroberfläche deutlich reduziert und Zelladhäsion und Migration nur noch wenig beeinflusst. Für zukünftige Experimente wurden selbstleitende FETs mit vergrabenem Kanal gebaut. Diese sind besonders als Substrat zur Ankopplung von spannungssensitiven Membranen geeignet. Alle Transistoren wurden im Hinblick auf ihre Threshold-Spannung, sowie ihren Wirkleitwert und ihr Rauschverhalten untersucht und verglichen.

Die statische Adhäsion sowie die zeitabhängige Dynamik unter Einfluss verschiedener Pharmaka wurde an HEK Zellen untersucht. Das Ablösen der Zellen durch die Serinpeptidase Trypsin, sowie der Einfluss des Ionophor Amphotericin B auf die Zellmembran wurden dokumentiert.

Vorexperimente für die gleichzeitige impedimetrische und potentiometrische Messung apoptotischer Zellen wurden durchgeführt. Weiterhin wurde die Adhäsion von Membranvesikeln und Erythrocyten-Ghosts erfolgreich gemessen. Bei allen Experimenten konnte der variable Verlauf der Transfer-Funktionen mit einem Modell nachvollzogen werden. Dieses beruht auf einem Ersatzschaltkreis, der sich an dem gängigen Punkt-Kontakt Modell für den Zell-Transistor-Kontakt orientiert. Sowohl die Eigenschaften des Transistors selbst als auch die Morphologie der Zelle bestimmen vier Zeitkonstanten des Systems. Diese wurden qualitativ untersucht.

Die Migration von Fibroblasten wurde zeitabhängig gemessen. Dabei zeigten sich unterschiedliche Charakteristika für Zellvorderseite, Zellmitte und Zellhinterseite. Die Adhäsion wurde auf der Ebene einzelner Filopodien sowie Lamellipodien dokumetiert. Unterschiedliche Zeitkonstanten wurden für das Annähern der Zelle an das Gate, das Stabilisieren des Zellkörpers, sowie das Ablösen der Zellhinterseite abgeschätzt.

Bei allen Experimenten stimmte die optische Kontrolle gut mit der elektrischen Messung überein. Insgesamt erwies sich die Methode der Transfer-Funktions Messungen als außerordentlich geeignet um Zelladhäsion und ihre Dynamik zu charakterisieren.

Jül-4261
Februar 2008
ISSN 0944-2952